# Structural Investigation on P-glycoprotein 1, Bile Salt Export Pump, and Sodium/Calcium Exchanger

Inauguraldissertation

*Zur*
*Erlangung der Würde eines Doktors der Philosophie*
*vorgelegt der*
*Philosophisch – Naturwissenschaftlichen Fakultät*
*der Universität Basel*

*von*

Raphael Küng

aus Basel, Schweiz

2020

Genehmigt von der Philosophisch-Naturwissenschaftlichen Fakultät

auf Antrag von

Prof. Dr. Henning Stahlberg, Fakultätsleiter

Prof. Dr. Jan Pieter Abrahams, Korreferent

Basel, den 26. Juni 2018

Prof. Dr. Martin Spiess, Dekan

## Summary

Transmembrane proteins span biological membranes and provide essential functions to the cell. Here we provide structural insight into three transmembrane proteins involved in substrate transport and signal transduction. Our goal is to understand the mechanism underlying the function of those proteins and to contribute thereby to improvements for future medical treatments.

P-glycoprotein 1 (Pgp) is an ABC transporter involved in multidrug transport. It provides protection from potentially toxic substances by exporting them from the cell. However in cancer cells upregulation of Pgp expression can interfere with therapy. Here we provide a near-atomic resolution structure of cross-linked nucleotide free Pgp interacting with UIC2, an inhibitory antibody, and the third generation Pgp inhibitor zosuquidar. Our structure shows binding of two zosuquidar molecules in the transmembrane domain of an occluded conformation. In addition we describe the binding interface of UIC2 binding, providing insight to the mechanism of conformational trapping. Characterized binding interfaces may be exploited for therapeutic purposes.

BSEP is the only bile salt transporter at the canalicular membrane of hepatocytes. Despite a very high sequence identity compared to Pgp, BSEP is way more selective. While diseases effected by mutations in BSEP are considerably rare, inhibition of BSEP can be the result of not intended interactions between BSEP and a variety of pharmaceutical compounds. I determined four structures of BSEP including a drug inhibited state using the antidiabetic drug glibenclamide and two structures in presence of the substrate taurocholate. These structures give rise to multiple potential models for the transport mechanism. In addition I could show that glibenclamide binds to the cytosolic facing cavity of BSEP, either repressing the connecting loop between the N- and C-terminal BSEP or locking BSEP in a inside open conformation. In addition mutations of BSEP associated with disease could be explained on structural basis.

NCX are a sodium/calcium exchangers widely spread among species, involved in calcium signalling. We have solved two crystal structures of the bacterial NCX from *Thermotoga maritima* in the outward facing conformation. Both conformations are substrate free, but show differences in the ion binding site. Comparison of our structures the NCX homolog from *Methanococcus jannaschii* suggest a simple reorientation of N-termianl helix 7 to switch NCX to the occluded state, indicating transition to the inward facing site.

# Contents

# 1 Introduction for ABC Transporters and P-glycoproteine 1

This introduction aims to give an overview for ABC transporters in general, but focussing more on exporters. In addition a introduction is given specific for Pgp, discussed in detain in the next chapter.

## Contents



## 1.1 Structure Of ABC Transporters

ABC transporters build a family of membrane proteins having a cytosolic ATP binding cassette. The ABC transporter superfamily is divided to 7 subfamilies comprising ABC1, MDR/TAP, MRP, ALD, OABP, GCN20, and White. Despite classification in one family, there is evidence for a polyphyletic origin of the transmembrane domains. Statistical sequence analyses indicate that the membrane spanning domains of ABC exporters have evolved independently al least three times ([1]). These origin from a triplication of a 2 transmembrane segment (TMS), a duplication of a 3 TMS and a duplication of a 4TMS precursor. Emerging domains comprise 8-10 TMS for the duplication of 4TMS precursors and 6 TMS for the other cases. For ABC importers a polyphyletic origin of transmembrane domains can be assumed based on structural evidence ([2]). ABC transporters promote active transport of substrate across the membrane driven by ATP binding and hydrolysis. This transport can take place against strong gradients. ABC transporters are widely spread among species. In bacteria uptake of nutrients, secretion of toxins to provide antibiotic resistance or as virulence factors are widely covered by ABC transporters ([3]). In eukaryotes no ABC importers are present, but exporters are involved in multiple processes from which clearance of potentially toxic compounds by

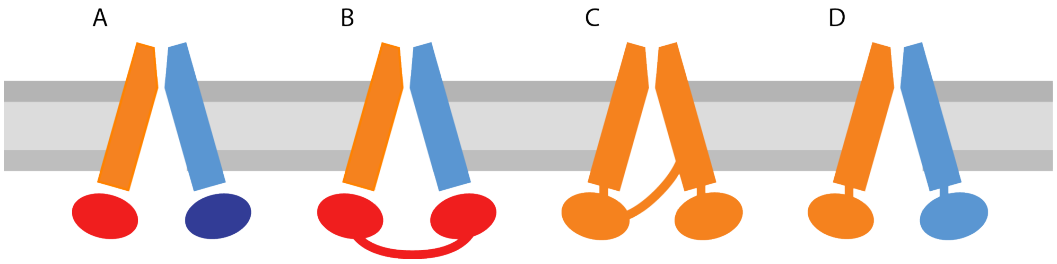


Figure 1: Schematic structure of some ABC transporters. **A** Transporter consist of four separate domains. **B** Transporter consist of two separate transmembrane domains (TMD) and two fused ATPase domains. **C** In full transporters all domains are part of the same polypeptide chain. **D** Half transporters consist of two copies of a TMD fused to a ATPase domain. Figure redrawn and adapted from [4]

ABC transporters of the MDR family is most prominent feature. Depending on the task, substrate specificity can be very broad or limited to a single target. With the exception of importers, ABC transporters consist of two transmembrane units and two ATPase units. In bacteria, ABC transporters are usually composed of four independent subunits (Figure 1A) or of two independent transmembrane domains and two fused ATPase domains (Figure 1B). Animal and fungal ABC transporters on the other hand generally consist of a single polypeptide chain with all four domains fused together (Figure 1C) as full transporters or a ATPase and a transmembrane domain fused as half transporter (Figure 1D) ([4]). The ATPase domains of ABC transporters, also called nucleotide binding domains (NBDs), consist of an assembly of different motifs to bind and hydrolyze ATP. Best known are the Walker A and B motif ([5]). The Walker A motif consists of a $\alpha$-helix, followed by a glycine rich loop, whereas the Walker B motif is build of a $\beta$-strand. Between the Walker A and B motif lies the C motif, also known as LSGGQ or signature motif. This motif is the hallmark of ABC transporters and participates in ATP binding. The serine side chain in the LSGGQ motif interacts with the $\gamma$-phosphate for coordination. The Walter A motif of one domain interacts with the LSGGQ motif of the other domain to bind ATP. This leads to a dimerization ([6]). The Walker B motif on the other hand is taking part in hydrolyzing ATP, providing a glutamate for the nucleophilic attack ([7]). The EAA loop of the TMD couples ATPase domain activity with the transmembrane domain through interactions with the Q-loop of the ATPase domain ([8]). The largest conformational change takes place upon binding of ATP and not hydrolysis as initially assumed ([9]).

## 1.2 How Do ABC Transporters Work

ABC transporters translocate their substrate over a membrane using ATP as driving force. ATP binding and hydrolysis takes place at the cytosolic nucleotide binding domains. The Walker A motif of one NBD and the signature sequence of the other NBD jointly bind an ATP molecule. Thereby a lysine of the Walker A motif interacts with oxygens of beta/gamma-phosphate of the ATP and aromatic residues of this motif take part in binding the adenine moiety of ATP ([10]). The gamma-phosphate interacts also with serine and glycine of the signature motif ([10], [11]). ATP has to be properly oriented to allow hydrolysis by the attacking water molecule ([8]). ATP hydrolysis takes place at the Walker B motif. Therefore a glutamate of the Walker B motif performs a nucleophilic attack on the ATP $\gamma$-phosphate ([7]). The exact mechanism is still elusive ([12]). A coordination network is needed for hydrolysis, including the beta- and gamma-phosphate of ATP, $Mg^{2+}$, the C-terminal aspartate and glutamate of the walker B motif, a glutamine of the Q-loop and multiple water molecules. ([12], [13], [14], [8], [15]). For some ABC transporters, including Pgp, a model of alternate ATP hydrolysis by NBD1 and NBD2 is proposed ([16]). For other transporters mutating one NBD does abolish transport activity, but mutating the other domain does not. This disagrees with a sequential process ([17], [18]).

Different models were proposed for the transport mechanism. Due to the broad range of transported substrates and the assumed polyphyletic origin of transmembrane domains multiple transport mechanisms might coexist. The flipflop mechanism is proposed for the transport of lipids or lipophilic molecules. Hereby the substrate is transported from one membrane leaflet to the other, including a change of the substrates orientation ([19]). An alternative model for the transport uses the alternative access model. For this model an outward open and an inward open conformation with different substrate affinities are assumed. For importers the inward open structure has a lower affinity for substrate binding. For exporters correspondingly the outward open conformation binds substrate weaker for release. In this model ATP binding and hydrolysis brings in the energy to switch between the two conformations, but transport is not mediated through the rearrangement of the transmembrane domains induced by ATP hydrolysis ([8]). The ATP-switch model assumes that the conformational change induced by ATP binding and hydrolysis effect substrate transport. Initial binding of the substrate leads to subtle rearrangements of the TMDs. These rearrangements increase the affinity of the NBDs for ATP binding. Dimerization of the NBDs is induced by ATP binding. Thereby the transporter changes from an inward open to an outward open conformation

to release the substrate. Subsequently ATP is hydrolysed and released to recover the initial inward open conformation ([20]). This model can be extended by an involvement of ATP hydrolysis to the release of a substrate. Another model is called vacuum cleaner model. It is a combination of the flipflop and ATP-switch model ([21]). Thereby the substrate enters the transporter from a membrane leaflet and is removed from the membrane.

## 1.3 P-glycoprotein 1

Pgp refers to permeability-glycoproteine. It belongs to the family of ABC-transporters, in particular to the MDR/TAP subfamily. Pgp spans 1280 amino acids and has the size of 141kDa and is decorated by an additionally glycosylation of 10-15kDa. Pgp exports harmful substances, in particular xenobiotics. This requires a vast flexibility to adapt to a broad range of compounds, without exporting physiologically relevant compounds. As xenobiotics are not restricted to certain features, there is no particular evolutionary adaption to the substrate possible. The encoding gene is known as MDR1 for the involvement of Pgp in multidrug resistance in cancer cells. Thereby overexpression of Pgp1 promotes resistance against certain antineoplastic drugs. This resistance is based on the ability to extrude a large range of anticancer drugs ([22]). Pgp transports preferably large uncharged amphipathic substrates like paclitaxel or doxorubicine. A typical feature is not known, thought aromatic rings, overall high hydrophobicity and tertiary amino groups are found in many substrates ([22], [23], [24], [25]). Amphipathic drugs are supposed to integrate into the outer membrane leaflet with the hydrophobic part. From there these drugs move to the inner leaflet by a flip-flop action. This process is rather slow giving Pgp enough time to handle drug influx. ([26], [27]). The speed of drug influx is important due to the low turnover of Pgp ([28], [29]). While for amphipathic substrates a cytosolic access could be optional, hydrophobic substrates probably enter Pgp from the inner leaflet only ([30], [31]).

To date no loss of function mutations are known for human Pgp, implying a clear necessity of its function. However studies in mice showed that a mutation of murine Pgp homologs has no effect on viability, unless these mice are exposed to drugs ([32], [33], [34]). There is a wide overlap of transported substrate with other transporters like ABCC1, ABCC2and ABCG2 ([35]), as well as with CYP2A4, a drug-metabolizing enzyme.

## 1.4 Tissue Distribution of P-glycoprotein 1

Pgp1 is expressed at multiple sites either to eliminate xenobiotics from the body or to protect exclusive vital organs.

Pgp is found on the apical side of mucosal cells of the intestine from duodenum to rectum ([36], [37], [38]). In the mucosa of the gut Pgp prevents entry of xenobiotics into the body. It does not only interfere with the uptake of amphipathic drugs ([39], [40], [41]), but also excretes intravenously administered drugs ([42], [43]). Interference with orally applied drugs can be strong enough to enforce intravenous administration or simultaneous treatment with Pgp inhibitors ([44]). In addition dietary components can modulate activity or availability of Pgp, modulating drug uptake ([45], [46]).

In the liver Pgp1 is expressed at the canalicular membrane of hepatocytes. There it takes part in the clearance of xenobiotics from the body by secretion into bile. The hepatic expression level of Pgp1 is individual and can differ by a factor of 50 ([47]). Nevertheless Pgp expression is in average sevenfold lower than in the small intestine ([48]).

Further Pgp is expressed at the luminal side of renal tubular cells to excrete xenobiotics and lipophilic drugs ([49]). Similar to hepatic and intestinal expression, renal Pgp is intended to purge toxic substances from the body.

The CNS is vital for survival. Therefore the blood-brain barrier adds safety layer to protect the brain from potentially toxic substances. In brain capillaries, endothelial cells are connected by tight junctions. These tight junctions prevent paracellular transport and enforce transcellular transport. An involvement of Pgp in the blood-brain barrier could be shown with mutant mice, being more sensitive to neurotoxic pesticide than wildtype mice ([50], [51]). Pgp reduces the accumulation of diverse drugs like paclitaxel, vincristine, digoxin or loperamide ([52], [53], [54]). It appears that current inhibitors are not able to inhibit Pgp at high expression levels as they are found in the blood-brain barrier.

In the placenta the fetus is protected by Pgp expression in fetus-derived epithelial cells of the placenta. Pgp1 is expressed in trophoblasts to protect the embryo from xenobiotics and other toxics. The trophoblasts proliferate to cytotrophoblasts and syncytiotrophoblasts, which build up the chorionic villi ([55]). The chorionic villi are in contact with maternal blood, filling the intervillous space. Pgp in the apical membrane of these cells protect the fetus against amphipathic toxins ([56]). In a mouse model Pgp mutants were more

sensitive to the teratogenic effect of avermectin ([57]).

Pgp1 is expressed in lymphocytes and in hematopoietic stem cells. The efflux might protect these cells from toxins ([58], [59]). On the other hand Pgp1 contributes to drug resistance in leukemia ([60]) and HIV treatment ([61]).

In cancer cells, upregulation of Pgp expression might promote drug resistance. Expression of Pgp is detected by immunohistochemistry. This assessment is error prone due to possible false positive signals from infiltrating macrophages and T cells. The impact of Pgp inhibition for cancer treatment is still uncertain. On one hand inhibitors used in early studies have a poor inhibitory performance leading to an underestimation of the effect of Pgp inhibition on cancer treatment. On the other hand Pgp inhibitors also affect drug elimination in intestine, kidney and liver. Therefore effects can be based on the higher abundance of the tested drug in the body, instead of impaired clearance from the tumor. ([18])

## 1.5 Genetic Polymorphism

The gene coding for Pgp1 holds 28 exons giving rise to 3843nt of coding RNA. To date about 100 single nucleotide polymorphisms (SNPs) have been identified in the coding region. At least 16 polymorphisms could be found in Germany ([62], [63]) and 9 in Japan ([64], [65]). In humans no null allele was detected so far. This is surprising based on the fact, that Pgp inhibition does not provoke a phenotype in absence of amphiphilic toxins. In mice and collies null alleles have been found, rendering them hypersensitive to ivermectin, a drug against nematode infections ([51], [66]). In addition, the progeny of heterozygous Pgp null mutant mice treated with the teratogenic ivermectin show phenotypes depending on the embryos genotype. Progeny of homozygous null mutant genotype (Mdr1a -/-) had a cleft palate, whereas homozygous wildtype progeny (Mdr1a +/+) showed no defects. In case of the heterozygous progeny (Mdr1a +/-) 30% had a cleft palate ([57]). This shows the dose dependency of Pgp substrates and potential implication of different alleles on drug response based on Pgp abundance and activity.

Following SNPs represents a subset, which was investigated more in depth. The SNP 2677G>T/A codes for an alanine, a threonine or a serine at position 893. Despite similar expression levels this SNP shows significant differences in the transport properties. $V_{max}$ for the transport of vincristine with S893 is 50% faster than in A893. For T893 $V_{max}$ exceeds 893A by 200% ([67]). This is consistent with a better response of the 2677G allele for treatment of chronic

myeloid leukemia with the drug imatinib ([68]). The SNP 1236C>T does not change the primary sequence of Pgp1. But still homozygosity of 1236T increases the response to imatinib in chronic myeloid leukemia ([68]). The silent C3435T mutation coding for isoleucine leads to a reduced abundance of Pgp in the intestine. This reduction correlates with digoxin uptake ([62]). Prevalence of 3435T differs between ethnic groups from 20-25% in African blacks to 55-75% in Caucasians ([69], [70]). This might influence interethnic variation in drug response ([71]). The missense SNP 1199G>T mutates the serine at position 400 to an isoleucine. Ile400 is associated with a four times lower in vitro substrate transport capacity. On the other hand SNP 1199A coding for a asparagine at position 400 increased resistance to tested Pgp1 substrates ([72]). The mutation G191R induced by SNP G571A reduces Pgp1 mediated resistance against vinblastine, vincristine, paclitaxel, and etoposide by a factor of 5. However, transport of doxorubicin and daunorubicin is not affected ([73]).

The influence of SNPs on the response to drugs remain partially contradictory. Due to the vast amount of SNPs in Pgp1 and the broad range of transported substrates, studies cover only a subset of possible combinations. Currently no prediction can be made for the pharmacokinetic based on a patients morph.

## 1.6 Activation of P-glycoprotein 1 by Xenobiotics

A plethora of pathways has been shown to take part in regulating of Pgp expression, among them NF-$_K$B and MAPK signaling pathways ([74], [75]). Substrates can induce ABCB1 expression via PXR/RXR (pregnane X receptor / retinoic acid receptor). PXR is a nuclear receptor capable to sense xenobiotics and to activate transcription of detoxification components as heterodimer with RXR. This is in line with the coexpression of Pgp with proteins of the cytochrome P450 3A family, which have been shown to be regulated by PXR ([76], [77], [48]). Transcriptional activation has been shown for PXR/-CAR (constitutive androstane receptor) ligands as well ([78]). This can induce enhanced drug efflux of co-administered drugs ([43]). On the other hand drugs having an inhibitory effect on Pgp1 can increase bioavailability of co-administered drugs ([79]). This effect can be used to increase therapy efficiency, but leads as well to a risk of an overdose when drugs are combined ([80]).

| **Class** | **Drug** |
|---|---|
| **Substrate:** | |
| Anticancer drugs | Docetacel, doxorubicin, etoposide, imatinib, paclitaxel, teniposide, vinblastine, vincristine |
| Steroids | Dexamethasone, methylprednisolone |
| Immunosuppressants | Cyclosporine, sirolimus, tacrolimus |
| HIV protease inhibitors | Amprenavir, indinavir, nelfinavir, saquinavir, ritonavir |
| Antibiotics | Erythromycin, levofloxacin, ofloxacin |
| β-blockers | Bunitrolol, carvedilol, celiprolol, tanilolol |
| $Ca^{2+}$-channel blockers | Diltiazem, verapamil |
| Cardiac drugs | Digoxin, digitoxin, quinidine |
| **Inducers:** | |
| Anticonvulsants | Carbamazepine, phenytoin, phenobarbital, primidon |
| Tuberculostatics | Rifampicin |
| Herbals | Hyperforin (constituent of St. John's wort) |
| **Inhibitors:** | |
| Calcium channel antagonisten | Verapamil |
| Makrolide antibiotics | Erythromycin, clarythromycin, not azithromycin |
| HIV protease inhibitors | Ritonavir |
| Immunosuppressents | Cyclosporin |
| Antiarrhythmics | Chinidin, propafenon |

Table 1: Substrates, inducers, and inhibitors of P-glycoprotein 1. Table redrawn in reduced form from ([82])

# 2 Structure of a zosuquidar and UIC2-bound human-mouse chimeric ABCB1

*The following section has been published in:*

Proceedings of the National Academy of Science of the United States of America (PNAS)
https://dx.doi.org/10.1073%2Fpnas.1717044115

**Structure of a zosuquidar and UIC2-bound human-mouse chimeric ABCB1**

Amer Alam[a], Raphael Küng[b], Julia Kowal[a], Robert A. McLeod[b], Nina Tremp[a], Eugenia V. Broude[c], Igor B. Roninson[c] Henning Stahlberg[b], and Kaspar P. Locher[a,*]

a - Institute of Molecular Biology and Biophysics, ETH Zürich, 8093 Zürich, Switzerland
b - Center for Cellular Imaging and NanoAnalytics, Biozentrum, University Basel, 4058 Basel, Switzerland
c - Department of Drug Discovery and Biomedical Sciences, College of Pharmacy, University of South Carolina, Columbia, SC, 29208

* Corresponding Author: locher@mol.biol.ethz.ch

## Contents



My contribution to this work comprised initial screening by negative stain and structure determination of the flexible ABCB1$_{HM}$-UIC2.

### Significance

The ATP binding cassette transporter ABCB1 (also termed P-glycoprotein) is a physiologically essential multidrug efflux transporter of key relevance to biomedicine. Here, we report the conformational trapping and structural analysis of ABCB1 in complex with the antigen-binding fragment of UIC2, a human ABCB1-specific inhibitory antibody, and zosuquidar, a third-generation ABCB1 inhibitor. The structures outline key features underlining specific ABCB1 inhibition by antibodies and small molecules, including a dual mode of inhibitor binding in a fully occluded ABCB1 cavity. Finally, our analysis sheds light on the conformational transitions undergone by the transporter to reach the inhibitor-bound state.

Keywords: ABC transporter, structure, small-molecule inhibitors, cryo-EM, mechanism

## 2.1 Abstract

The multidrug transporter ABCB1 (P-glycoprotein) is an ATP-binding cassette transporter that has a key role in protecting tissues from toxic insult and contributes to multidrug extrusion from cancer cells. Here, we report the near-atomic resolution cryo-EM structure of nucleotide-free ABCB1 trapped by an engineered disulfide cross-link between the nucleotide-binding domains (NBDs) and bound to the antigen-binding fragment of the human-specific inhibitory antibody UIC2 and to the third-generation ABCB1 inhibitor zosuquidar. Our structure reveals the transporter in an occluded conformation with a central, enclosed, inhibitor-binding pocket lined by residues from all transmembrane (TM) helices of ABCB1. The pocket spans almost the entire width of the lipid membrane and is occupied exclusively by two closely interacting zosuquidar molecules. The external, conformational epitope facilitating UIC2 binding is also visualized, providing a basis for its inhibition of substrate efflux. Additional cryo-EM structures suggest concerted movement of TM helices from both halves of the transporters associated with closing the NBD gap, as well as zosuquidar binding. Our results define distinct recognition interfaces of ABCB1 inhibitory agents, which may be exploited for therapeutic purposes. P-glycoprotein (ABCB1) is an ATP-binding cassette transporter ubiquitously expressed in a wide range of cells and tissues, where it has an important role in cellular detoxification ([81], [18]). Its wide substrate specificity underlies its physiological relevance in drug transport across multiple blood-organ barriers, resulting in modulation of drug delivery, drug-drug interactions, and

drug pharmacokinetics for a host of clinically active agents ([81], [18], [82], [83]). ABCB1-mediated drug efflux has been linked to multidrug resistance, adversely affecting cancer chemotherapeutic treatment and treatment of various brain disorders ([84], [85], [86]). The ABCB1-specific inhibitory antibody UIC2 was developed with the goal of increasing antitumor drug treatment efficacy ([87], [88]). UIC2 targets the extracellular moiety of human ABCB1 ($ABCB1_H$) and has been successfully used to investigate the transport cycle of ABCB1 owing to its ability to bind the transporter during various states of the catalytic cycle ([88], [89], [90]). Although the crystal structure of the antigen-binding fragment (Fab) of UIC2 has been determined ([91]), the conformational epitope on the surface of $ABCB1_H$ has remained elusive because direct visualization of the ABCB1-UIC2 interface was limited to low-resolution cryo-EM reconstructions ([92]). To date, several structures of mouse ABCB1 are available, including those with bound inhibitors ([93], [94], [95], [96]) and nucleotides ([97]). However, despite added ligands, all these reveal the transporter in an inward-open conformation with varying degrees of nucleotide-binding domain (NBD) separation and a largely unchanged transmembrane domain (TMD) and substrate translocation pathway.

Small-molecule, third-generation inhibitors, including zosuquidar, tariquidar, and elacridar ([98], [99], [100]), have shown potential in model systems for coadministration with various anticancer agents. However, antibody- and small-molecule inhibitor-based strategies have not been successfully utilized clinically ([101], [102]), emphasizing the need for designing more effective therapeutic and diagnostic strategies targeting ABCB1 expression and inhibition. A detailed understanding of the structure of ABCB1 with bound antibody fragments and drugs/inhibitors in different conformations is central to improving the specificity of inhibitors and to further our understanding of the chemistry governing ABCB1 interaction with high-potency inhibitors. To achieve this, we generated a hybrid construct of human and mouse ABCB1 ($ABCB1_{HM}$) that contains the extracellular region of the human protein, including the recognition epitope of UIC2, on a background of mouse ABCB1. $ABCB1_{HM}$ shares ~90% sequence identity with the human protein (SI Appendix, Section 2.5) and takes advantage of the higher biochemical stability of mouse ABCB1, which shares high sequence similarity and, except for subtle differences, exhibits highly similar substrate/inhibitor-binding properties with its human homolog, especially with regard to third-generation inhibitors ([103]). As highlighted in Figure 2 and SI Appendix, Figure 6, our results reveal key $ABCB1_H$-specific residues involved in the interaction interfaces of both zosuquidar and UIC2 and ABCB1. ABCB1 has been observed to exist in a range of conformations with varying degrees of NBD separation, including

a nucleotide-bound "closed" conformation, where no gap between NBDs exists ([92]). To understand its interaction with small molecules, we sought to visualize an intermediate conformation of the transporter, where the NBD gap has been partially, but not fully, closed. To visualize and analyze the effect of progressive NBD gap closure on the TMD domains (in the absence of bound nucleotides in this case), we therefore generated a variant that allowed disulfide cross-linking of the NBDs of the transporter (ABCB1$_{HM-X}$). The latter harbors two S $\rightarrow$ C mutations at positions 559 and 1,204 in the dimerization (D)-loops, expected to come within close proximity to each other upon NBD dimerization as seen in the canonical ABC exporter Sav1866, among others, and successfully used for conformational trapping and high-resolution analysis of other ABC transporters ([104], [105]).

## 2.2 Results

### 2.2.1 Conformational Trapping and Functional Characterization of ABCB1$_{HM}$

ABCB1$_{HM-X}$ was shown in vivo to confer up to 50-fold higher paclitaxel resistance to mammalian cells when expressed in an inducible HEK293 cell line compared with uninduced cells (SI Appendix, Figure 7A), showing that the construct retains paclitaxel transport activity. The construct is strongly inhibited by zosuquidar and UIC2, which resensitize ABCB1$_{HM-X}$-expressing cells to paclitaxel (Figure 2Fig. 1 B and C) at nanomolar concentrations. The constructs were expressed in HEK293 cells and purified in a lauryl maltose neopentyl glycol (LMNG) and cholesteryl hemisuccinate (CHS) mixture in contrast to the more commonly used dodecyl maltoside (DDM)-based preparations to avoid interference from nonspecifically bound DDM molecules in the transmembrane (TM) ligand-binding cavity. Disulfide cross-linking of ABCB1$_{HM-X}$ was nearly complete in the absence of added nucleotides, as revealed by gel electrophoresis (SI Appendix, Figure 7B), and ABCB1$_{H}$, ABCB1$_{HM}$, and cross-linked or reduced ABCB1$_{HM-X}$ all showed near-identical UIC2-binding affinities (SI Appendix, Figure 7C).

While previous studies have reported negligible basal ATPase rates for detergent-purified ABCB1 ([106]), our LMNG/CHS-purified ABCB1$_{H}$ and ABCB1$_{HM}$ constructs maintain a measurable, albeit low, basal ATPase rate (~20-30 nmol$\cdot$ min$^{-1}\cdot$mg$^{-1}$), which is stimulated up to 10-fold by addition of zosuquidar or the anticancer drug paclitaxel (SI Appendix, Figure 7D), allowing for characterization of drug-mediated ATPase activity in an identical environment as used for our structural analysis. Although disulfide cross-linking did not alter

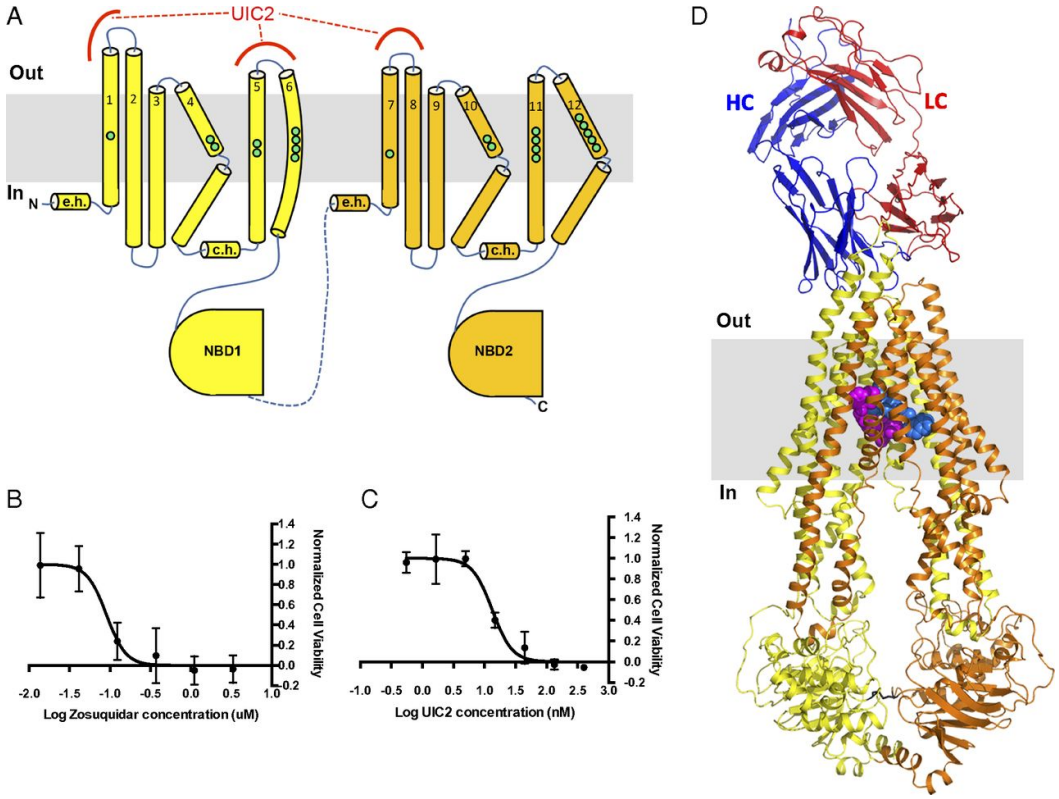


Figure 2: Structural and functional characterization of UIC2-Fab and zosuquidar-bound ABCB1. (A) Topology diagram of ABCB1. TM helices are numbered, and their relative lengths, as well as the locations of kinks or bends, are schematically illustrated. The locations of residues interacting with bound zosuquidar are schematically shown as filled green circles. External loops EL1, EL3, and EL4 interact with bound UIC2-Fab, as indicated by red lines. C, carboxy terminus; c.h., coupling helices; e.h., elbow helices; N, amino terminus. (B) Inhibition of $ABCB1_{HM-X}$-mediated protection from paclitaxel by zosuquidar (n = 3, error bars represent SD). (C) Inhibition of $ABCB1_{HM-X}$-mediated protection from paclitaxel by UIC2 (n = 3, error bars represent SD). (D) Ribbon representation of the UIC2-bound $ABCB1_{HM-X}$ structure, with the two halves of ABCB1 colored yellow and orange, respectively, and the heavy (HC) and light (LC) chains of UIC2-Fab colored blue and red, respectively. The approximate location of the membrane is depicted in gray. Two bound zosuquidar molecules are shown in light blue and pink sphere representation. The engineered disulfide between the two NBDs is shown as black sticks.

$K_m$ values for ATP hydrolysis in ABCB1$_{HM-X}$ and its ATPase stimulation by zosuquidar, we observed a reduction in ATPase stimulation by paclitaxel that could be reversed by addition of DTT (SI Appendix, Figure 7D and E). Interestingly, zosuquidar has been shown to stimulate the ATPase rate of detergent (DDM)-solubilized ABCB1 but inhibits the lipid-reconstituted ABCB1 ATPase rate, with the effect in the latter being much stronger ($EC_50$ ~200 nM, roughly 50-fold lower than that obtained in DDM micelles) (24). This opposing effect in detergent versus lipid has been speculated to stem from the occlusion of a primary high-affinity zosuquidar-binding site by DDM molecules, leading to zosuquidar binding to a secondary low-affinity site. As seen in SI Appendix, Figure 7F, while the ATPase activity of both ABCB1$_H$ and ABCB1$_{HM}$ purified in LMNG/CHS is stimulated by zosuquidar, the EC50 values for this modulation are ~200 nM, comparable to those reported for native membranes. Combined with the absence of bound detergent molecules in our inhibitor-bound structure, our results suggest that zosuquidar is bound to its primary site in our studies, as explained below.

### 2.2.2 Overall Structure of ABCB1-UIC2 in Complex with Zosuquidar

The structure of cross-linked, zosuquidar-bound ABCB1$_{HM-X}$ was solved to an overall resolution of 3.58Å [Fourier shell correlation (FSC) cutoff of 0.143] (Figure 2D and Figure 8). The high disulfide trapping efficiency correlated well with the observation that the overwhelming majority of usable particles corresponded to a single conformation of ABCB1. The local resolution was highest in the TM region, allowing unambiguous de novo building of the TMDs, including the zosuquidar-binding pocket, as well as the ABCB1-UIC2 interface (Figure 9). Despite their close association due to the disulfide cross-link, the NBDs did not adopt a fully closed sandwich conformation, which is a hallmark of ATP-bound structures, because no nucleotide was added. They maintained a degree of conformational flexibility reflected in the lower resolution of the electron density, nevertheless allowing atomic interpretation guided by the structures of mouse ABCB1 previously reported with minor manual adjustment where appropriate. Despite the overall lower resolution for the NBDs, density for the introduced disulfide cross-link was visible. The NBD arrangement was somewhat asymmetrical, closely matching that observed in the heterodimeric, bacterial homolog of ABCB1, TM287/288 ([107]). Asymmetry in ABCB1 hydrolysis has previously been proposed ([97], [108]) and also observed in a bacterial homolog of asymmetrical B family transporters, TmrAB ([109]). Our structure revealed a single copy of UIC2-Fab bound to the external side of the transporter and tilted by about 70° relative to the membrane plane (Fig-

ure 2D). Whereas the architecture and fold of ABCB1$_{HM}$ are similar to those of mouse ABCB1 ([94], [97]), the trapped conformation is distinct from previous structures because the NBDs are closer together and the TMDs assume a conformation that provides structural insight into an occluded and inhibitor-bound state of a B-family ABC exporter. As with previously reported ABCB1 structures, no density was observed for the linker region connecting the two halves of the transporter.

### 2.2.3 Molecular Details of the ABCB1-UIC2-Binding Interface

UIC2 recognizes a conformational epitope of ABCB1 that involves residues from TM1 and TM2 and the extracellular loops EL1, EL3, and EL4 (Figure 3A and B), in agreement with biochemical studies that have identified the external part of TM1 ([87]) and the external loop connecting TM5 and TM6 (EL3) ([90]) as contributing to the ABCB1$_H$-UIC2 interface. The buried surface area amounts to ~1,075Å$^2$, with the heavy chain of UIC2-Fab forming the bulk of the interface (~80%). The observed interactions include polar, electrostatic, and hydrophobic contacts, including methionine-pi stacking. Differences in the amino acid sequences of the external loops of ABCB1$_{HM}$ can readily explain the specificity of UIC2 for the human protein over that of rodents (Figure 3C). Additionally, the observed interaction provides a structural explanation of how UIC2 inhibits transport activity of ABCB1: By clamping the external loops together, UIC2 prevents ABCB1 from converting to an outward-open conformation, which is required to release substrate to the outside ([110], [111]). This is in line with studies indicating incomplete UIC2 binding in unmodified ABCB1-expressing cells ([87]), where the transporter is expected to exist in a mixture of conformations, including a UIC2-incompatible, outward-open state. It also agrees with the observed modulation of UIC2 affinity for ABCB1 in the presence or absence of various nucleotides and substrates ([90]). Any alteration of the equilibrium between the outward-open and outward-closed conformations of ABCB1 caused by the binding or release of drugs/nucleotides as part of the transporter's catalytic cycle could alter its affinity for UIC2. As ABCB1 has previously been shown to hydrolyze ATP in the presence of UIC2 ([112]), we conclude that the architecture of ABCB1 allows the NBDs to bind and hydrolyze ATP, while having the TMDs assume an outward-closed conformation. This is in agreement with the expected conformational landscape sampled by ABCB1 based on recent spectroscopic measurements and molecular dynamics studies on mouse ABCB1 ([110]), where an outward-occluded state with a closed NBD interface and outward closed TMD has been observed. Such a conformation is also compatible with those observed in structures of related

prokaryotic ABC exporters ([107], [113]), as well as the recently determined ATP-bound zebrafish CFTR structure ([114]), and is expected to be generally shared among various ABC exporter family members ([115]).

### 2.2.4 Details of the Zosuquidar-Binding Pocket

The zosuquidar-bound structure of ABCB1 reveals a large cavity that spans almost the entire width of the lipid membrane (Figure 2D and Figure 3D and E). The cavity is sealed from the external and cytoplasmic sides, and is lined by residues from all 12 TMs of ABCB1 (Figure 2A and SI Appendix, Figure 6), comprising many of the residues identified in biochemical studies as contributing to drug interactions of ABCB1 ([116], [117], [118], [119], [120], [121]). Although some of these side chains have been observed to be in contact with ligands in previously reported structures of ABCB1, these structures all described inward-facing conformations, with no enclosed cavities observed and fewer interactions with bound substrates ([93], [94], [96], [113]). As shown in Figure 3D and E, our EM density unambiguously revealed two zosuquidar molecules bound in the enclosed cavity, filling most, but not all of the available space. As a consequence, residues from eight TMs directly interact with bound zosuquidar. The two zosuquidar molecules assume defined orientations, are wrapped around each other, and roughly follow a twofold rotational symmetry. This is in stark contrast to structures of mouse ABCB1 in complex with cyclic inhibitors in the inward-open conformation ([122]). The distribution of interacting residues, which are fully conserved between our construct and $ABCB1_H$ (green dots in Figure 2B and SI Appendix, Figure 6), demonstrates that the two halves of ABCB1 contribute in a pseudosymmetrical fashion to zosuquidar binding, as the contacting residues belong to TM1, TM4, TM5, and TM6 (first half of ABCB1) and to TM7, TM10, TM11, and TM12 (second half of ABCB1). In addition to the many aromatic and hydrophobic residues, there are polar or charged side chains in the observed cavity (SI Appendix, Figure 10). The majority of these have been predicted to be part of the primary drug-binding site of ABCB1 ([94], [119], [120], [123]). Specifically, Y953 is seen in our structure to hydrogen-bond with one of the zosuquidar molecules (SI Appendix, Figure 11B) as predicted based on molecular dynamics and mutagenesis studies, although this study predicted only one zosuquidar bound in the cavity in a different configuration compared with that observed in our structure. The absence of interfering detergent, along with the close association of the bound inhibitors with residues predicted to be primary contributors to specific binding of zosuquidar ([116]), further validates the relevance of the observed binding site. The observation of two bound zosuquidar molecules

agrees with previous biochemical and structural findings suggesting that the ABCB1 drug-binding pocket is capable of accommodating multiple ligands simultaneously ([122], [124]). The presence of many aromatic residues can offer an adaptive plasticity to the pocket, in line with studies suggesting an induced fit mechanism of ligand recognition ([125]). We conclude that ABCB1 may bind inhibitors through a combination of specific interactions, leading to defined binding modes and a rigid core of bound inhibitor molecules surrounded by TM helices.

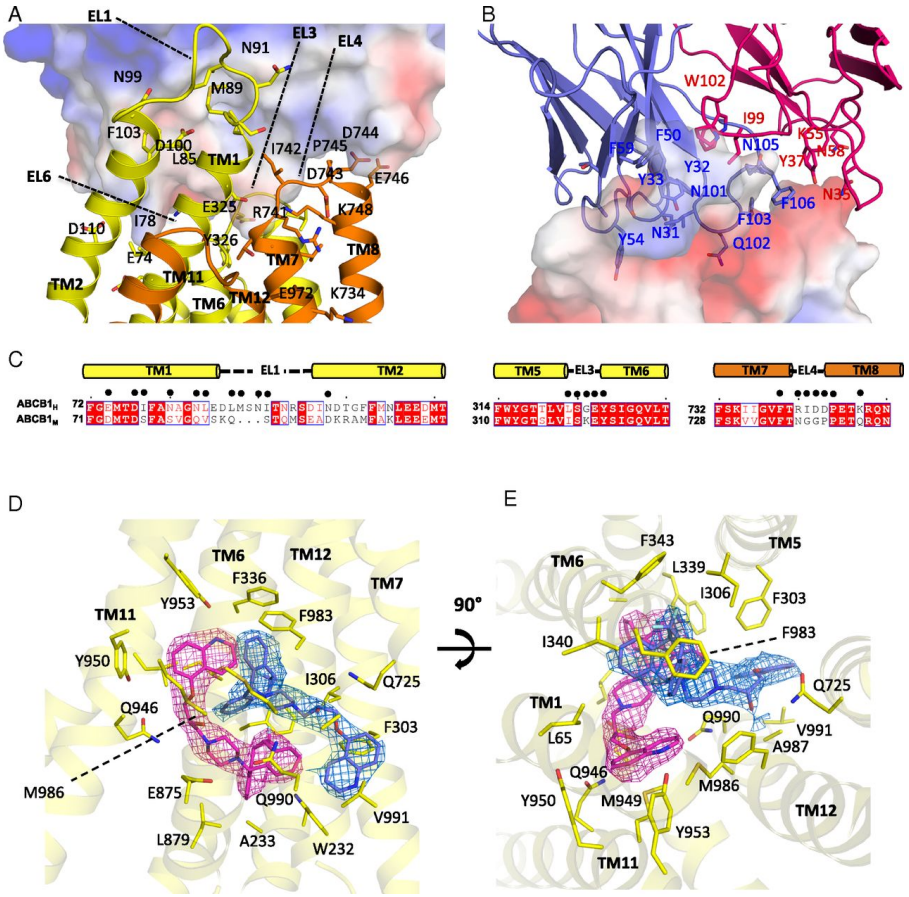


Figure 3: Details of UIC2-binding interface and zosuquidar-binding pocket. (A) Close-up view of the ABCB1-UIC2 interface with the UIC2-Fab-binding region shown as an electrostatic surface potential map and ABCB1 shown in ribbon representation. TM helices and ELs of ABCB1 are labeled. ABCB1 residues interacting with UIC2-Fab or with a structural role in stabilizing the outward-closed conformation of ABCB1 are shown as sticks and labeled. (B) Similar view as in A, but with ABCB1 shown as semi-transparent electrostatic surface potential map. UIC2-Fab is shown in ribbon representation and colored blue (heavy chain) or red (light chain). Select UIC2 residues within 5Å of ABCB1 are shown as sticks. (C) Sequence alignments of EL1, EL3, and EL4 regions of $ABCB1_H$ and mouse ABCB1, with secondary structure motifs shown above the sequences. Black dots represent residues of $ABCB1_H$ within 4Å of UIC2 as seen in our $ABCB1_{HM-X}$-UIC2 structure. (D) Ribbon diagram of ABCB1 viewed parallel to the membrane plane, with several TM helices removed for clarity. Two bound zosuquidar molecules are shown as pink and blue sticks, and the corresponding EM density is shown as pink and blue mesh. Selected ABCB1 residues within 4Å distance of bound zosuquidar are shown as yellow sticks and labeled. (E) Similar to D but viewed from the external side of the membrane.

### 2.2.5 Conformational Changes Associated with NBD Closure

To understand the contributions of disulfide-mediated NBD trapping and zosuquidar binding to the TMD conformation and the formation of an inhibitor-binding pocket, we determined two additional cryo-EM structures (Figure 4A). The structure of an amphipol (A8-34) reconstituted, non-cross-linked variant, ABCB1$_{HM-EQ}$, was determined in the absence of any drugs or nucleotides, but in complex with UIC2-Fab (SI Appendix, Figure 11). ABCB1$_{HM-EQ}$ harbors an E $\rightarrow$ Q mutation in the Walker-B motif, which increases the stability and limits the conformational heterogeneity of the sample. The ABCB1$_{HM-EQ}$ structure revealed an inward-open conformation with wide NBD separation, closely matching (rmsd = 1.88 for all aligned C$\alpha$atoms) previously reported mouse ABCB1 structures ([94], [95], [97], [122]) (SI Appendix, Figure 11E). A detailed structural analysis (Figure 4Fig. 3B) revealed that the transition from the inward-open state to the disulfide-trapped, zosuquidar-occluded state includes distinct changes in the TMDs, most significantly in the conformations of TM4 and TM10 (Figure 4C). Despite exhibiting different sequences otherwise, the three residues P223, S238, and G251 in TM4 correspond to identically spaced and located residues P866, S880, and G894 in TM10, allowing for similar helix bending and kinking. Along with the already bent and kinked TM6 and TM12, this amounts to four TM helices of ABCB1 that form significant kinks, forming a cytoplasmic gate to the zosuquidar-binding cavity and closing the lateral membrane opening that exists in the inward-open conformation (Figure 5A and B). We then determined the structure of disulfide-trapped ABCB1$_{HM-X}$, also in complex with UIC2-Fab, but in the absence of drugs or nucleotides. We found that the separation of the NBDs in the apo ABCB1HM-X structure was identical to that of the zosuquidar-bound state. The conformation of the external loops of ABCB1 and the conformation of the interface with UIC2 binding are indistinguishable in the three structures, which is in line with the observation that UIC2 binding allows the transporter to cycle through its complete ATP hydrolysis cycle despite the absence of a discrete outward-open conformation ([92], [112]). Although the structure of disulfide-trapped apo ABCB1$_{HM-X}$ is at slightly lower resolution than the zosuquidar-bound structure, side-chain density is still visible for most TMs, allowing unambiguous determination of the side-chain register. When all particles are used for 3D reconstruction, we observed blurred density in the regions of TM4 (residues 237-244) and TM10 (residues 880-888) owing to local conformational flexibility (SI Appendix, Figure 12, Figure 13, Figure 14). Upon subclassifying, we could identify distinct and roughly equally populated conformations where TM4 and TM10 either adopt kinked conformations (class 1/map 2) as observed in the zosuquidar-bound state (Figure 5C) or straight

conformations (class 2/map 3) as observed in the apo-inward ABCB1$_{HM}$ structure. We conclude that the closing of the NBD gap by disulfide trapping, which is transmitted to the TMDs via the coupling helices, allows TM4 and TM10 to sample both the straight and kinked conformations. Upon binding of zosuquidar, only the kinked conformation is observed. A stabilization of the two TMDs of ABCB1 has been also been reported upon binding of the third-generation ABCB1 inhibitor tarquidar ([117]), whose proposed binding site overlaps with the zosuquidar-binding site in our structure, pointing to similar modes of interaction with the transporter. In the related multidrug transporter ABCC1/MRP1 ([126]), binding of substrate was accompanied by a slight reduction in NBD separation and narrowing of the binding pocket, which, nevertheless, remained open to the cytoplasm.

## 2.3 Conclusions

Our results provide a number of insights into the modulation of ABCB1, as well as the chemistry of the underlying specific ligand interactions. First, we offer visualization of a fully occluded ligand-binding cavity of a type 1 ABC transporter occupied by a small-molecule inhibitor, identifying the details of zosuquidar binding to ABCB1. Such a conformation has been extremely difficult to trap owing to the highly dynamic nature of ABCB1, prompting us to employ covalent linkage of the NBDs. Given that disulfide-trapped ABCB1$_{HM-X}$ hydrolyzes ATP at a similar rate as the native protein and maintains stimulation by zosuquidar, the observed conformation provides physiologically relevant insight. This is further supported by the fact that we observed spontaneous and near-complete cross-linking for the designed cysteine pairs, and our structural analysis revealed the majority of particles to belong to a homogeneous class, consistent with an occluded state of ABCB1. Visualization of an occluded ABCB1 cavity offers a unique tool for in silico studies of drug binding to the transporter, which have so far relied on inward-open structures of ABCB1 and models based on different transporters. The ability of two inhibitor molecules to bind in tandem raises the possibility of cooperativity in binding, which, in the absence of a more sensitive readout for drug binding, we are currently unable to fully analyze. The zosuquidar-inhibited state captured in our structure also raises the question of whether transport substrates can bind similarly in well-defined orientations to the exact same site in ABCB1. Interestingly, based largely on its opposing ATPase modulatory behavior in lipid- or detergent-embedded ABCB1, zosuquidar, along with elacridar and tariquidar, has recently been proposed to bind to a low-affinity site in the presence of detergent, which is thought to bind to, and hence render, the proposed high-affinity site

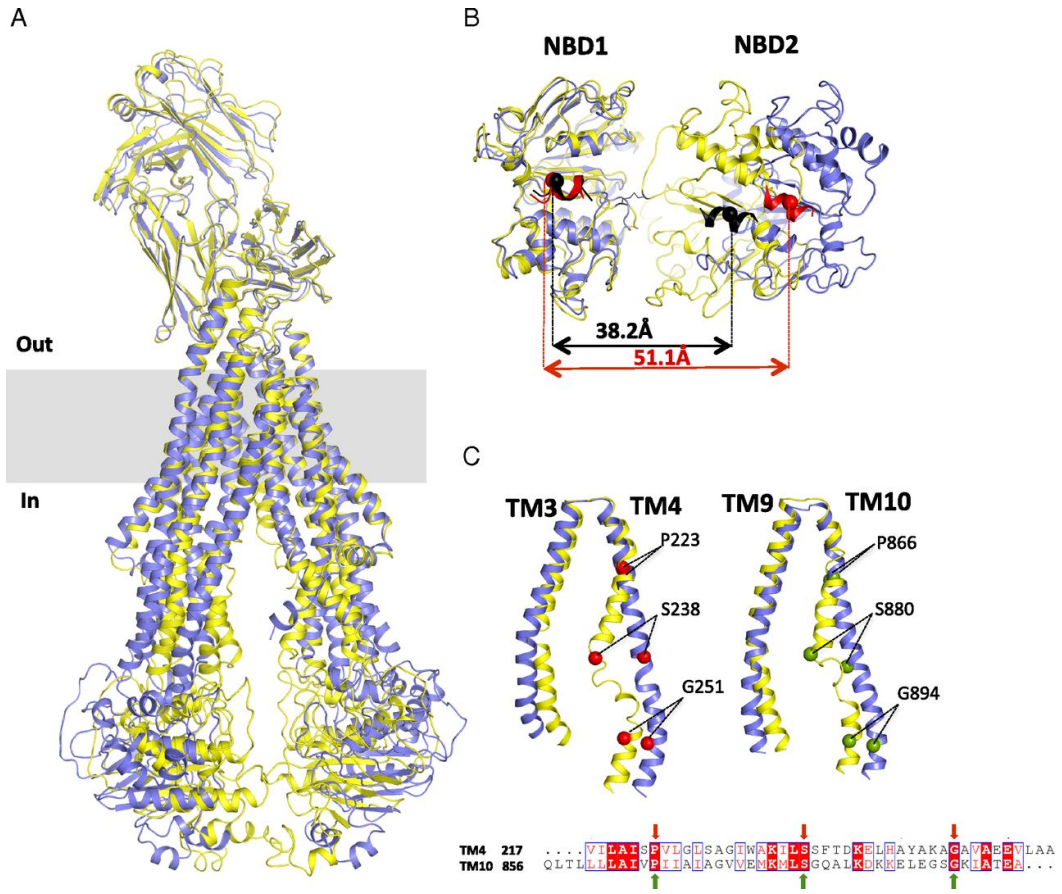


Figure 4: Conformational changes in ABCB1. (A) Comparison of apo-inward ABCB1$_{HM}$UIC2 (blue) and disulfide-trapped, apo ABCB1$_{HM-X}$-UIC2 (yellow) using UIC2-Fab as an anchor point for the superposition. The gray box represents the approximate location of the plasma membrane. (B) Close-up view of the NBDs of the two structures shown in A, but using NBD1 as the superposition anchor. The coupling helices of ABCB1$_{HM}$ and ABCB1$_{HM-X}$ are colored red and black, respectively. The Cα atoms of V264 and V908 of the coupling helices are represented as spheres, with the distance between them shown as black and red arrows. (C) Superposition of the TM helix pairs TM3-TM4 and TM9-TM10 of the two ABCB1 structures colored as in A. Red and green spheres depict Cα atoms of selected residues, with numbers indicated. A sequence alignment of TM4 and TM10 of human ABCB1 is shown below the structures, and the designated residues are indicated with arrows.

inaccessible for the inhibitor ([103]). While we cannot categorically rule out

such a different binding mode for zosuquidar, a number of observations help further validate the physiological relevance and significance of our zosuquidar-bound structure. First, we observe no interfering detergent molecules in the binding cavity, arguing against detergent-mediated occlusion of the primary zosuquidar-binding site. Second, our $EC_{50}$ values for zosuquidar modulation of LMNG-solubilized ABCB1 match those measured in native membranes, with our observed modulation effect being much stronger than that reported for DDM-based preparations ([103]). Third, the conformational changes in TM4 and TM10, although never before seen to occur in tandem, closely match those observed for TM4 in mouse ABCB1 in complex with select cyclic peptide inhibitors ([122]). In light of these findings, the explanation for the opposing effects of zosuquidar on ATPase activity of lipid-reconstituted or detergent-solubilized ABCB1 may need to be readdressed.

Second, the ability to narrow the NBD gap by cross-linking rather than addition of nucleotides allowed for the intriguing finding of abrogated ATPase stimulation by paclitaxel. While subtle conformational changes within the observed occluded cavity upon full NBD closure with bound nucleotides are possible, this result might indicate that some transport substrates (including paclitaxel) cannot access the occluded conformation seen in our zosuquidar-bound structure. Although individual instances of helix bending/kinking have previously been observed in ABCB1 structures ([95], [122], [127]), our structures visualize simultaneous conformational changes in the two halves of the transporter, involving conserved, helix-breaking residues. The structural rearrangements in the TMDs may not only occur during inhibition but possibly also during a productive transport cycle.

Finally, we elucidate the conformational epitope of the UIC2 antibody and the mechanism of its inhibitory activity. Most importantly, our structure clearly rules out the existence of an outward-open ABCB1 conformation in the presence of UIC2 as speculated upon based on low-resolution EM analysis of human ABCB1-UIC2 complexes ([92]).

Overall, the work presented herein opens new avenues for the development of more potent antibody and small-molecule inhibitors of ABCB1 that could be used alone or in combination with small-molecule inhibitors, while shedding light on the conformational changes undergone by the transporter upon ligand binding.

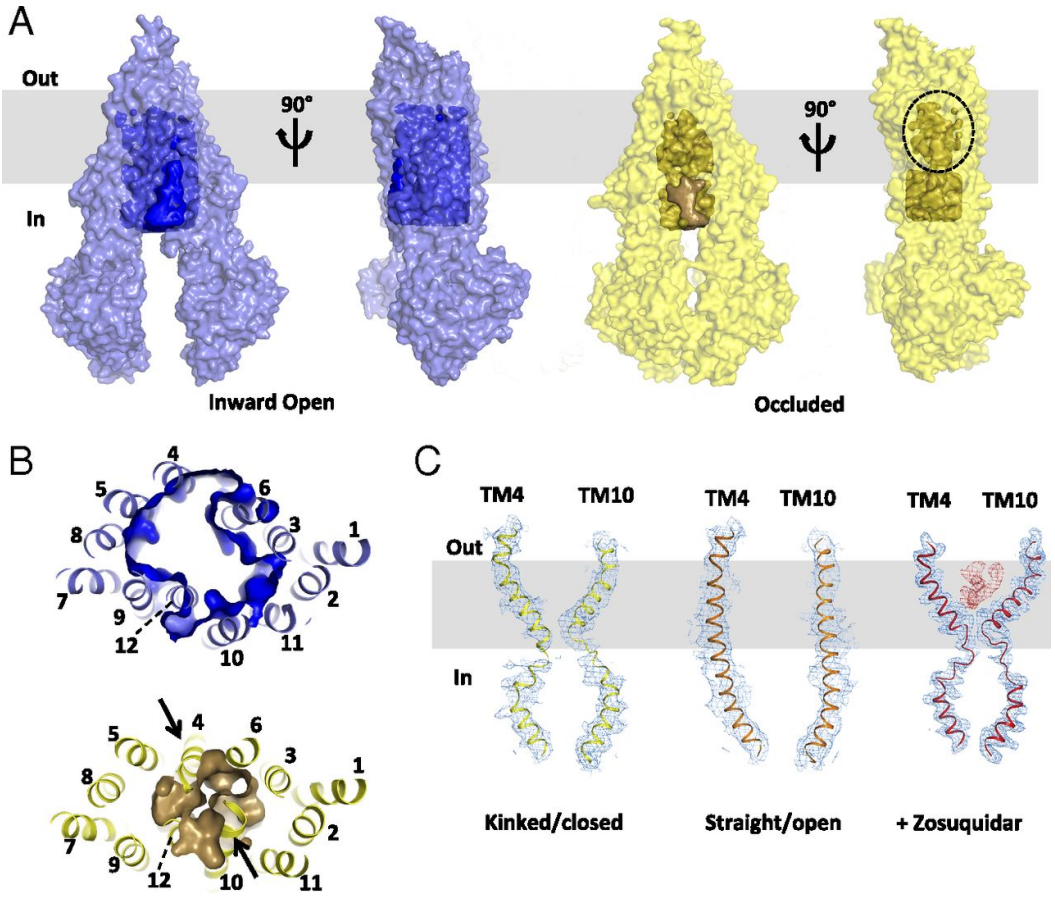


Figure 5: Structural changes in the translocation pathway. (A) Surface representations of inward-open ABCB1$_{HM}$ and disulfide-trapped ABCB1$_{HM-X}$ structures (without bound UIC2-Fab) colored blue and yellow, respectively. Internal cavity volumes are depicted as dark blue and gold-colored surfaces. The dashed oval indicates the location of the occluded TM cavity that binds zosuquidar in the zosuquidar-bound structure. The gray box represents the membrane. (B) Translocation pathways of ABCB1$_{HM}$ and ABCB1$_{HM-X}$ colored as in A, but viewed from the cytoplasmic side of the membrane. TM helices are shown as ribbons and numbered. Arrows indicate the constriction point or cavity gate formed by kinks in TM4 and TM10, closing off the cavity to the cytoplasm in the occluded ABCB1$_{HM-X}$ structure. (C) Side views of ribbon representation of TM4 and TM10 and the corresponding EM density of ABCB1$_{HM-X}$ structures. (Left and Center) Two populations of disulfide-trapped apo ABCB1$_{HM-X}$, suggesting equilibrium between kinked (closed) and straight (open) conformations. (Right) Zosuquidar-bound structure, where only the kinked conformation exists. Density for the bound zosuquidar molecules is shown as red mesh.

## 2.4 Materials and Methods

### 2.4.1 Protein Expression and Purification

A PCR-free cloning strategy was employed for all $ABCB1_{HM}$ constructs, which were synthetically generated (Thermo Fisher Scientific). For the variant of the $ABCB1_{HM}$ D-loop cross-link mutant ($ABCB1_{HM-X}$), a 3C protease site (LEVLFQGP) replaced residues 668-675 in the linker connecting the two halves of the transporter. All genes were cloned into an expression vector harboring the pXLG gene expression cassette in a pUC57 vector (GenScript) ([128], [129]) between BamH1 and Not1 restriction digestion sites. All genes were cloned with a C-terminal EYFP/rho-ID4 tag with an intervening precision (3C) protease cleavage site between the protein and purification tag. A stable cell line for $ABCB1_{HM-X}$ was generated using the Flp-In T-REx Kit (Thermo Fisher Scientific) for inducible expression as per the manufacturer's guidelines.

Transient expression for $ABCB1_{HM}$ and $ABCB1_{H}$ (sequence ID AAA59576.1) constructs was carried out in HEK293T adherent cultures. Cells were grown and maintained in DMEM (Thermo Fisher Scientific) supplemented with 10% FBS (Thermo Fisher Scientific) at 37°C with 5% $CO_2$ under humidified conditions. Purified DNA was mixed with branched polyethylenimine (PEI; Sigma) at a 1:2 (DNA/PEI) ratio and applied to cells after exchanging medium to expression medium (DMEM + 2% FBS). Expression and growth media were supplemented with a penicillin/streptomycin mixture (Thermo Fisher Scientific). For $ABCB1_{H}$, expression was allowed to proceed for 72 h at 37°C. All synthetic gene constructs were expressed in the presence of 4mM valproic acid (Sigma) at 30°C for 96h. A stable cell line for $ABCB1_{HM-X}$ was grown and maintained similarly; induced with 1μg·mL$^{-1}$ tetracycline and protein expression, it was allowed to proceed for 72h at 37°C. Cells were washed with PBS before being harvested and flash-frozen in liquid nitrogen for storage at -80°C.

For protein purification, frozen cell pellets were thawed and homogenized using a Dounce homogenizer in an eightfold (vol/wt) excess of resuspension buffer containing 150mM NaCl and 25mM Hepes (pH 7.5), in addition to 10-20% glycerol and a protease inhibitor mix (prepstatin A, leupeptin, soy trypsin inhibitor, and phenylmethylsulfonyl fluoride), followed by addition of detergent, except for the $ABCB1_{HM-EQ}$ sample for EM analysis, which was purified in 250mM NaCl and 50mM Tris (pH 7.5). For all $ABCB1_{H}$ genes, protein extraction was allowed to proceed in the presence of a mixture of 0.4% dodecyl maltopyranoside (DDM), 0.1% octaethylene glycol monododecyl ether (C12E8), and 0.1% CHS for 90min before being centrifuged for 30min at 37,060 × g in

a SA600 fixed-angle rotor. For $ABCB1_{HM}$ constructs, 0.5/0.05% LMNG/CHS was used for solubilizing protein for 60min before centrifugation. Clarified supernatant was applied to Sepharose-coupled Rho-ID4 antibody (University of British Columbia) and incubated for 3-18h. Beads were washed four times with 10 column volumes (CV) of purification buffer containing 150mM NaCl, 25mM, and Hepes (pH 7.5), along with 10-20% glycerol and 0.01/0.01/0.004% DDM/C12E8/CHS ($ABCB1_H$) or 0.02/0.004% LMNG/CHS (all $ABCB1_{HM}$ constructs). For the $ABCB1_{HM-EQ}$ sample for EM analysis, buffer and salt components were adjusted to contain 250mM NaCl and 20mM Tris (pH 8.0). For direct comparison of $ABCB1_H$ and $ABCB1_{HM}$ constructs in ATPase assays, DDM/C12E8/CHS-solubilized $ABCB1_H$ was bound to ID4 columns and exchanged to LMNG/CHS buffer during the wash and subsequent purification steps. Protein was eluted by adding 3 CV of wash buffer containing a 1:10 wt/wt excess of 3C protease or by addition of 0.5mg/mL ID4 peptide (GenScript) for 2-18h. The 3C protease was His-tagged and removed by incubating the cleaved protein with nickel nitrilotriacetic acid beads (Qiagen). All purification steps were carried out at 4°C.

### 2.4.2 Antibody Purification and Fragmentation

UIC2 hybridoma cells were cultured in Wheaton CeLLine Bioreactors as per the manufacturer's recommendations. Protein G and Protein A (GenScript) columns were used for antibody purification and antibody fragmentation, which were carried out using the Fab Preparation Kit protocol (Thermo Fisher Scientific). Fab purity was judged by SDS/PAGE, followed by size exclusion chromatography (SEC), after desalting into storage buffer containing 150 mM NaCl and 25 mM Hepes (pH 7.5) or 250mM NaCl and 20mM Tris (pH 8.0) for use with $ABCB1_{HM-EQ}$ for EM analysis.

### 2.4.3 Cytotoxicity Assays

The $ABCB1_{HM-X}$ stable cell line was grown and maintained as described above. Induced or noninduced cells were plated at a density of 5,000-10,000 cells per well of a 96-well plate and allowed to attach for 1-2h. Cells were then exchanged to medium containing paclitaxel at various concentrations and incubated for a further 48-72 h. Medium was exchanged, and cell viability was measured using the WST-1 cell proliferation/viability kit (Sigma). The assay was repeated in the presence of 10μM zosuquidar, added 1-3h before paclitaxel. To test the effect of UIC2, induced cells were plated as described above and

preincubated with varying UIC2 concentrations for 1h at 37°C. Paclitaxel was then added directly to the medium (final concentration 0.5μM), cells were incubated for 48-72h, and viability was measured described as above. The results shown are for three independent experiments (Figure 2B and C and SI Appendix, Figure 7A). Data were fit to a sigmoidal dose-response curve, plotted in GraphPad Prism 6, and normalized to calculated $B_{max}$ values from the fitted curve after subtraction of the calculated $B_{min}$ values (to adjust for background levels in separate assays) from the respective datasets.

### 2.4.4 Cysteine Cross-Linking of ABCB1$_{HM-X}$

Detergent-purified protein was incubated with 1 mM dichloro(1,10-phenanthroline) copper(II) (Sigma) for1 h at 4°C and desalted back into buffer lacking the oxidant using Sephadex G-25 desalting columns (GE Healthcare) to stop the reaction. For ABCB1$_{HM-X-3C}$, cross-linking efficiency was analyzed by SDS/PAGE (SI Appendix, Figure 7B). The 3C protease-cleaved samples were loaded in reducing and nonreducing loading buffer, and the ratio of cross-linked to non-cross-linked transporter was judged by comparing the full transporter band (cross-linked, ~140kDa) and the cleaved half-transporter bands (non-cross-linked, ~50kDa). Cross-linked protein was subsequently used for biochemical assays and EM sample preparation as described below.

### 2.4.5 ATPase Assays

Measurements of ATP hydrolysis were performed using a molybdate base colorimetric assay as previously described ([130]). Protein concentrations used in the assays in the range of 0.1-0.2mg/mL zosuquidar (Medkoo Biosciences) and taxol/paclitaxel (Sigma) were dissolved in DMSO and added to reaction mixes at the desired concentrations. The reactions were started upon addition of 2mM ATP in the presence of 10mM $MgCl_2$ at 37°C. For $K_m$ determination, a range of ATP concentrations was used. Linear regression and statistical analyses were performed using GraphPad Prism 6.

### 2.4.6 Antibody-Binding Assay

Purified Avi-tagged proteins were first desalted into biotinylation buffer [75mM NaCl, 25mM Hepes (pH 7.5), 10mM magnesium acetate, 10mM ATP, and 50μM biotin] containing the detergent/CHS mix used for protein purification

before addition of 5-10µg biotin ligase BirA (produced in-house), and the reaction was allowed to proceed overnight at 4°C, followed by desalting into buffer containing 150mM NaCl,25 mM Hepes (pH 7.5), 10-20% glycerol (buffer A), and the respective detergent/CHS mix. A total of 1-5 pmol of biotinylated proteins was added to each well of a preblocked 96-well Neutravidin plate (Thermo Fisher Scientific) for up to 1h at room temperature. All incubations were carried out on a plate shaker (Unimax 1010 Orbital Platform shaker; Heidolph) at 350rpm. Unbound transporters were discarded, and the wells were washed three times with 200 µL of buffer A supplemented with the respective detergent/CHS mix (buffer AD). A total of 100µL of serially diluted UIC2 antibody was added to the wells and incubated for30 min at room temperature. Unbound UIC2 was discarded, and the wells were washed three times with buffer AD as before. Horseradish peroxidase (100µL)-conjugated goat mouse anti-IgG (catalog no. A16072; Thermo Fisher Scientific) diluted to 1 mg/mL (1:1,500) in buffer A was added to the wells for 30 min. After discarding unbound antibodies, the wells were washed as before, followed by development using the TMB Substrate Kit (Thermo Fisher Scientific). Absorbance (450nm) was read using a BioTek Synergy HT plate reader. Readings were plotted against UIC2 concentrations and fit to a single-site specific binding equation in GraphPad Prism 6. Data were normalized to calculated $B_{max}$ values for comparative purposes.

### 2.4.7 EM Sample Preparation

LMNG/CHS-purified $ABCB1_{HM}$ constructs were mixed with a two- to threefold molar excess of UIC2-Fab. The $ABCB1_{HM-EQ}$-UIC2 complex was mixed with a 1:10 wt/wt excess of amphipol A8-35 (Anatrace) for 4h at 4°C, followed by overnight biobead (BB-SM2)-mediated removal of detergent. UIC2-Fab complexes of detergent-purified and amphipol-reconstituted samples were concentrated to 5-8mg/mL before being purified on a $G4000_{SWXL}$ SEC column in buffer containing 250 mM NaCl and 20mM Tris (pH 8.0) (amphipol) or 150mM NaCl and 25mM Hepes (pH 7.5) (detergent samples). Peak fractions corresponding to the purified complexes were pooled and used for cryo-EM grid preparation. For the zosuquidar complex, the inhibitor was added to a final concentration of 10µM before grid preparation. Freshly purified samples were applied to glow-discharged Lacey carbon grids (LC200; Electron Microscopy Sciences) and plunge-frozen in liquid nitrogen-cooled liquid ethane using a Vitrobot Mark IV (FEI) operated at 4°C with a blotting time of 3-4s and >90% humidity.

### 2.4.8 Data Collection and Processing

An overall data processing scheme for structure determination is provided in SI Appendix, Figure 14. Two different microscopes were used for data collection for the detergent-purified, cross-linked samples and the amphipol-reconstituted samples (FEI Titan Krios 1 and 2, respectively; SI Appendix, Figure 15). Grids were clipped for loading into a Titan Krios microscope (FEI) running at 300 kV equipped with a Gatan Quantum-LS Energy Filter (GIF) and a Gatan K2 Summit direct electron detector. For the zosuquidar complex of ABCB1$_{HM-X}$-UIC2, image stacks comprising 48 frames were collected at a nominal magnification of 165,000× in superresolution mode with an estimated dose per frame of 1.54 electrons per square angstrom, corresponding to a total dose of 74 electrons per square angstrom. Stacks were motion-corrected, dose-weighted, and twofold Fourier-cropped to a calibrated pixel size of 0.84Å in MotionCor2 ([131]). Contrast transfer function (CTF) estimates were performed using gCTF ([132]), followed by particle picking and extraction of a total of 469,224 particles from 2,479 micrographs in Relion 2.0 ([133], [134], [135]). After several rounds of 2D classification, 352,880 particles in all usable classes were used for 3D classification using a low-pass-filtered map of the cross-linked apo structure (discussed below) as a reference. Of those, two near-identically looking classes comprising 231,969 (66%) particles were combined and used for 3D refinement and postprocessing to yield a 3D map at 3.78Å resolution, whereas the remaining particles fell into unusable classes with missing NBDs. We suspect this arises from poorly averaged or heterogeneous particle sets, as well as missing orientation views and the fact that despite high cross-linking efficiency, a subset of transporters may not be linked, and may thus add to overall variability in conformational mobility of the NBDs. A model map for the detergent belt was generated from this map in UCSF Chimera ([136]), masked in Relion, and used for signal subtraction from the input set of particles used for the initial refinement to yield a final postprocessed map resolution of 3.58Å. The reported resolution for all maps was based on the FSC cutoff criterion of 0.143 ([137]). Local resolution estimation was performed using ResMap ([138]).

For the apo ABCB1$_{HM-X}$-UIC2 sample, image stacks comprising 80 frames each with an estimated dose per frame of ~0.9 electrons per square angstrom, corresponding to a total accumulated dose of 72 electrons per square angstrom, were collected at a magnification of 105,000× in superresolution mode, followed by motion correction and dose weighting in MotionCor2. Stacks were twofold binned via Fourier-cropping to a calibrated pixel size of 1.387Å for processing using Relion 2.0. CTF estimates were performed using gCTF, followed by

picking and extraction of a total of 820,566 particles from 2,614 micrographs in Relion. After 2D classification, an input set of 785,152 particles was used for 3D classification using a low-pass-filtered map of the ABCB1$_{HM-EQ}$-UIC2 structure (discussed below) as a reference. Of those, 517,053 particles (66%) from two similar-looking 3D classes were combined for a round of 3D refinement that yielded a 4.78Å map. After masking and postprocessing in Relion using automatically determined B-factors, we obtained a resolution of 4.33Å. This map was used to obtain a model map for the detergent belt, which was generated as described for the zosuquidar complex dataset and used for signal subtraction using the input particle set used for the initial refinement. The new signal-subtracted dataset was then used to refine a single 3D class comprising 517,053 particles. Masking and postprocessing using automatically determined B-factors as before yielded a final map with a resolution of 4.14Å (map 1) that was used for model building. A second, smaller detergent belt model was similarly generated to create a second signal-subtracted dataset that served as input for one more round of 3D classification, where a search for three 3D classes yielded two distinct classes that shared a similar architecture but showed differences in conformations of TM4 and TM10. Class 1 (153,652 particles) and class 2 (158,827 particles), containing kinked and straight conformations of TM4 and TM10, respectively, were both refined to a resolution of ~4.5Å (map 2 and map 3, respectively). The remaining particles fell into the third class containing blurred density in the regions of TM4 and TM10 and were not analyzed further.

For the ABCB1$_{HM-EQ}$-UIC2 complex, image stacks comprising 80 frames each were collected at a nominal magnification of 105,000× in superresolution mode with an estimated dose per frame of 1.0 electron per square angstrom, corresponding to a total dose of 80 electrons per square angstrom. The software suite Focus ([139]) was used for online data processing and pruning, applying motion correction with MotionCor2, including twofold binning of the recorded micrographs after motion correction to a calibrated pixel size of 1.336Å and CTF estimation with gCTF. Particles were picked with gAUTOMATCH ([140]) using a template-based approach, with templates created from the published ABCB1-UIC2 complex structure ([108]) using e2proc2d.py (EMAN2) ([141]). The same model was used later as a starting model in 3D classification. Micrographs were imported for processing in Relion, and a total of 347,049 particles were extracted from 2,038 micrographs, followed by two rounds of 2D classification, to yield a particle set of 112,196 particles. Following two rounds of 3D classification, the remaining 78,282 particles were used for 3D auto-refinement in Relion. Partial signal subtraction was performed to remove the amphipol belt for final 3D refinement and postprocessing to yield a final resolution of 6.25Å.

### 2.4.9 Model Building and Refinement

Postprocessed maps, as well as non-B-factor sharpened maps were used for model building in Coot ([142]) for all datasets. The quality of electron density in the TMD regions of the apo and zosuquidar maps allowed for de novo model building. The map quality in the NBD region was, on average, of lower quality compared with the TMDs, which were resolved to near-atomic resolution (SI Appendix, Figure 9 and Figure 12). Modeling of the NBD region was therefore guided by published structures of ABCB1 [Protein Data Bank (PDB) ID codes 4M1M and 5KO2], followed by manual adjustment where required and permitted by map quality. The UIC2 crystal structure (PDB ID code 5JUE) was manually docked into the Fab density using UCSF Chimera, followed by adjustment in Coot. Two molecules of zosuquidar were unambiguously fit into the corresponding electron density in the ABCB1-binding pocket. We observed electron density characteristic for a bound phospholipid that was tentatively modeled as phosphatidylethanolamine (PE) in both the apo- and zosuquidar-bound occluded ABCB1$_{HM-X}$ structures. PE and glycan monomers were obtained from the Coot monomer library (monomer codes 3PE and NAG, respectively). Geometric restraints for all ligands were generated in Phenix. The model for ABCB1$_{HM-EQ}$-UIC2 was based on the structure of the apo-occluded state. Map quality allowed for rebuilding the TMDs to fit the

density and was guided, in part, by the structure of mouse ABCB1 (4M1M).

Real-space refinement of the models was carried out in Phenix ([143], [144]), with default restraint parameterization along and automatically generated secondary structure restraints. Refinement statistics for all models are presented in SI Appendix, Table S1. For validation of the zosuquidar complex model, random coordinate errors up to 0.3Å were introduced into the refined model, which was subsequently refined against one of the half-maps from the 3D auto-refine run from Relion. Minimal differences in FSCs computed between the refined model and the half-map used for refinement compared with those between the refined model and the half-map excluded from refinement point to a model free from overrefinement (SI Appendix, Figure 8). All figures were prepared using UCSF Chimera and PyMOL (The PyMOL Molecular Graphics System, Version 1.8; Schrödinger, LLC). Cavity volumes were calculated using HOLLOW ([145]) as described. Structure alignment and rmsd calculations were done in PyMOL. Ligand interaction diagrams were prepared in LigPlot+ ([146]). Residue numbers in figures are based on equivalent residues in the fully human protein.

## 2.5 Supplementary Material

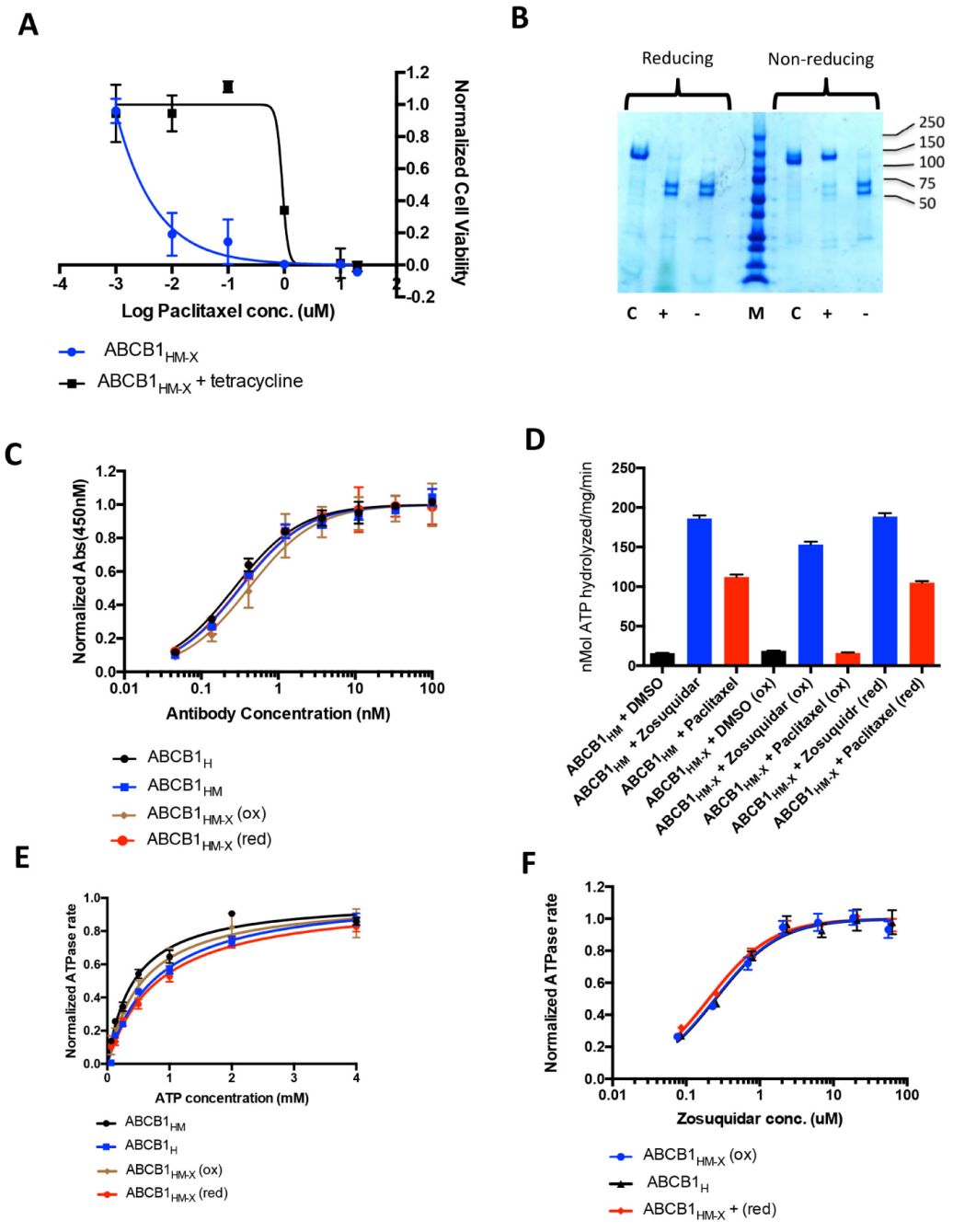

Figure 7: Functional characterization and disulfide trapping of ABCB1. A Cell viability analysis of $ABCB1_{HM-X}$ stable cell line in the presence or absence of tetracycline induction (n=3, error bars indicate s.d).). B SDS-PAGE of $ABCB1_{HM-X-3C}$ harboring a protease cleavage site for determining disulfide cross-linking efficiency. Cross linked species (+) and non-cross linked species (−) are shown along with bands corresponding to $ABCB1_{HM}$ are shown for comparative purposes (C). M represents the molecular marker sample. C ELISA-based UIC2 binding analysis of $ABCB1_{H}$, $ABCB1_{HM}$. disulfide- trapped (ox) or DTT-reduced (red) $ABCB1_{HM-X}$. (n=3, error bars represent s.d). D Basal and zosuquidar (10μM) or Paclitaxel (10μM) stimulated ATPase rates for $ABCB1_{HM}$, disulfide cross-linked $ABCB1_{HM-X}$. Also shown are ATPase rates for DTT-reduced $ABCB1_{HM-X}$ in the presence of zosuquidar or Paclitaxel (n=3, error bars represent s.d). E Zosuquidar-stimulated ATPase rates of $ABCB1_{H}M$, $ABCB1_{H}$, and disulfide-trapped (ox) or DTT-reduced (red) $ABCB1_{HM-X}$ (n=3, error bars indicate s.d). F Comparison of EC50 values for zosuquidar modulation of ATPase activity for detergent purified and oxidized or reduced $ABCB1_{HM-X}$ and $ABCB1_{HM}$ (n=3, error bars represent s.d). $EC_{50}$ values were in the range of 0.2-0.25μM for all three samples.

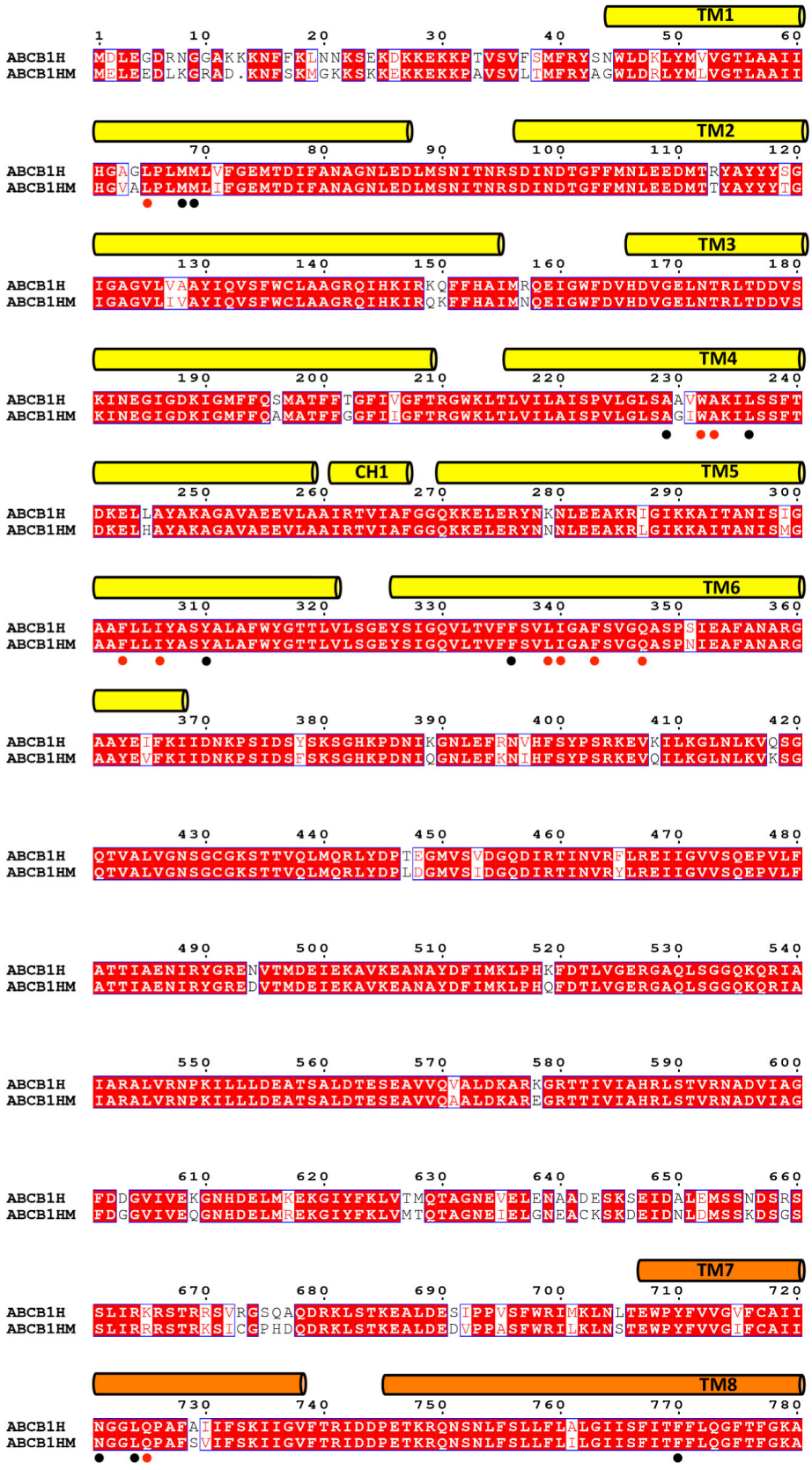
TM1
TM2
TM3
TM4
CH1
TM5
TM6
TM7
TM8
ABCB1H
ABCB1HM

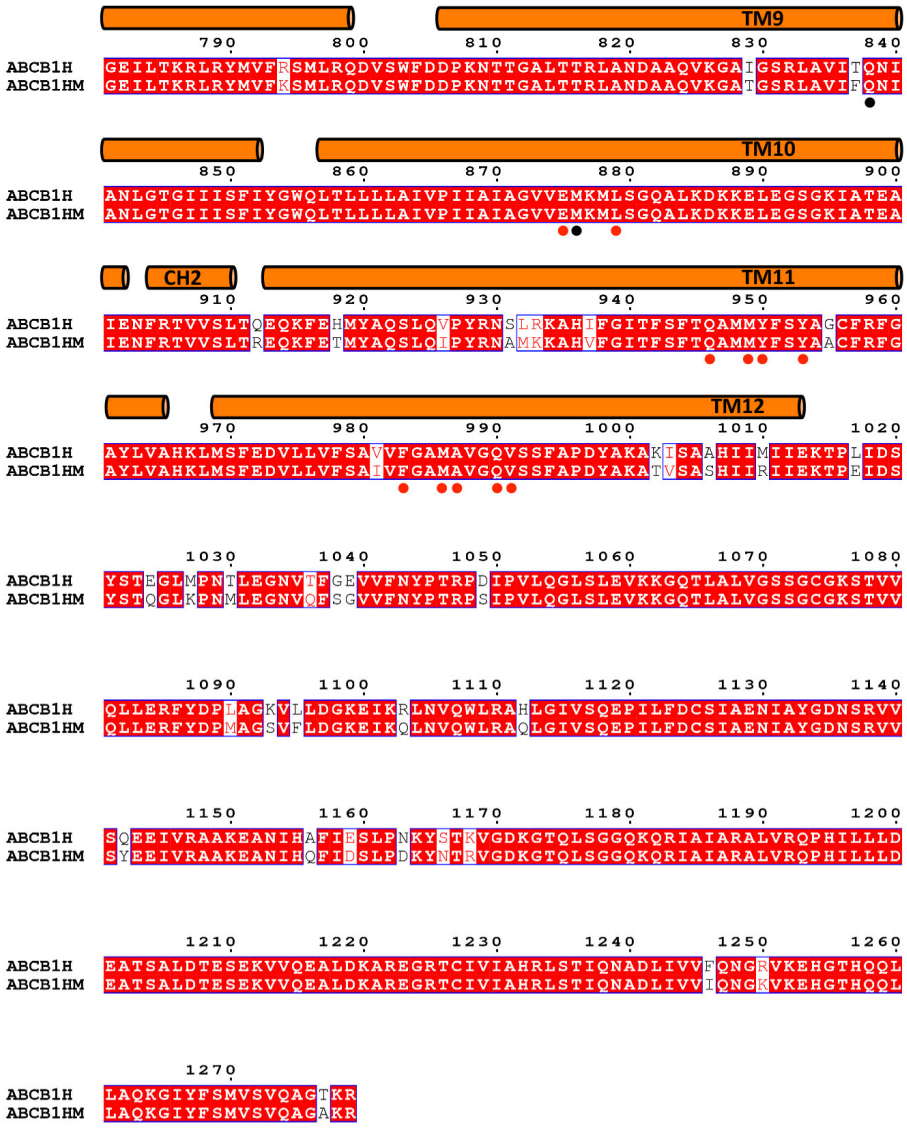


Figure 6: Sequence alignment of human ABCB1 ($ABCB1_H$) and the chimeric human-mouse ABCB1 construst ($ABCB1_{HM}$), with secondary structure assignment of transmembrane helices (TM) and coupling helices (CH) shown and numbered. Black dots indicate residues of the drug binding pocket (5Å distance to bound zosuquidar) whereas red dots indicate the subset of these within 4Å of either of the two zosuquidar molecules seen in the zosuquidar-bound $ABCB1_{HM-X}$-UIC2 structure.

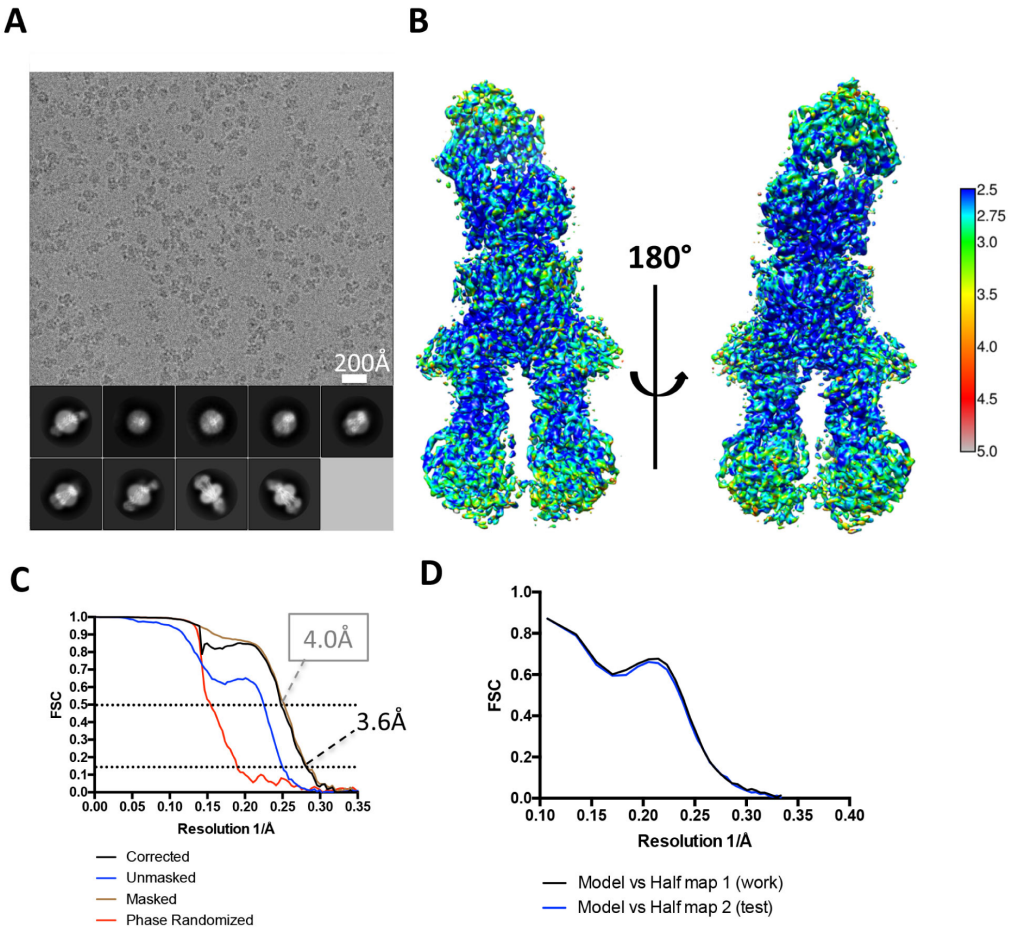


Figure 8: Cryo-EM analysis of zosuquidar-bound, disulfide-trapped ABCB1$_{HM-X}$-UIC2 complex. A Representative micrograph at -2.6µm defocus along with representative 2D classes. Scale bar is indicated in white. B Front and back views of cryo-EM volume colored according to local resolution estimate. The color key s shown on the right, numbers indicate Å resolution. C FSC curves showing resolution estimates determined by 0.143 and 0.5 cutoff criterion (black and grey dashed lines, respectively). D Model vs map FSC curves for a model refined against half map 1. The FSC curve calculated against half map 1 (work) are shown in black while that against half map 2 (test) is shown in blue.

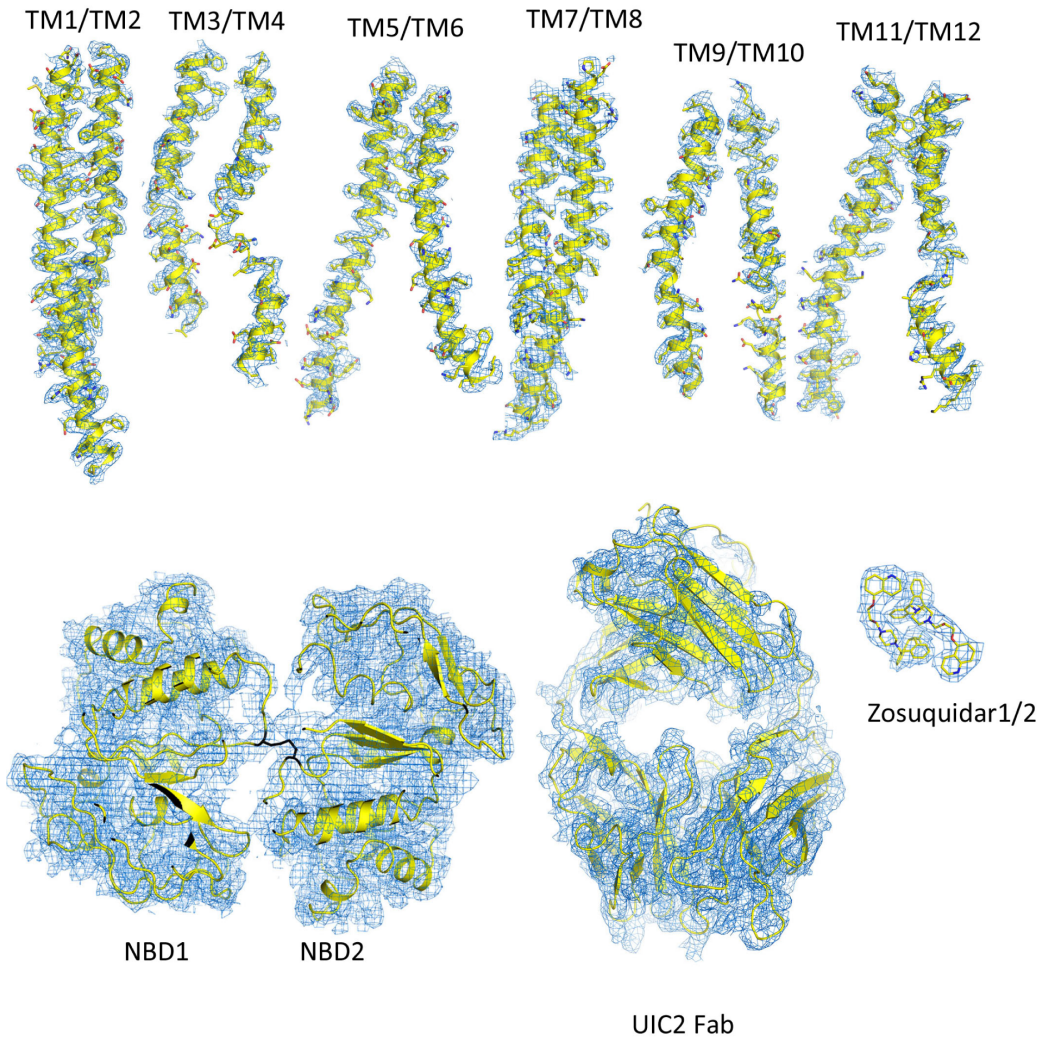


Figure 9: Quality of EM density (blue mesh) of the structure of disulfide-trapped, zosuquidar-bound ABCB1$_{HM-X}$-UIC2. Top, pairs of transmembrane domains are shown as ribbons (yellow), with selected side chains shown as sticks. Bottom, NBDs and UIC2-Fab are shown as ribbons, zosuquidar molecules are shown as sticks. The disulfide cross-linked cysteine residues in the D-loops of the NBDs are shown as black sticks.

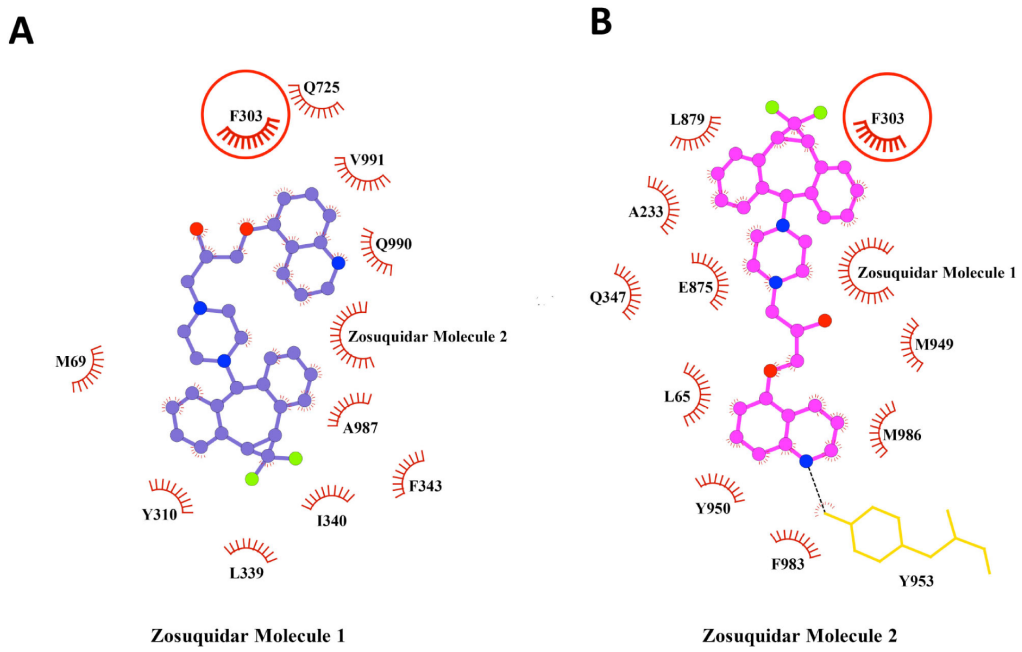


Figure 10: Residue interactions of individual zosuquidar molecules (ball and stick representation, colored similarly to Figure 7D-E) observed in the ABCB1$_{HM-X}$ binding pocket. Residues interacting with both molecules are indicated (red circle). Non bonded interactions are represented by spoked arcs and hydrogen bonds are indicated by dashed black lines. A Ligand interactions of zosuquidar molecule 1. B Ligand interactions of zosuquidar molecule 2. ABCB1 residue Y953 is shown iine format.

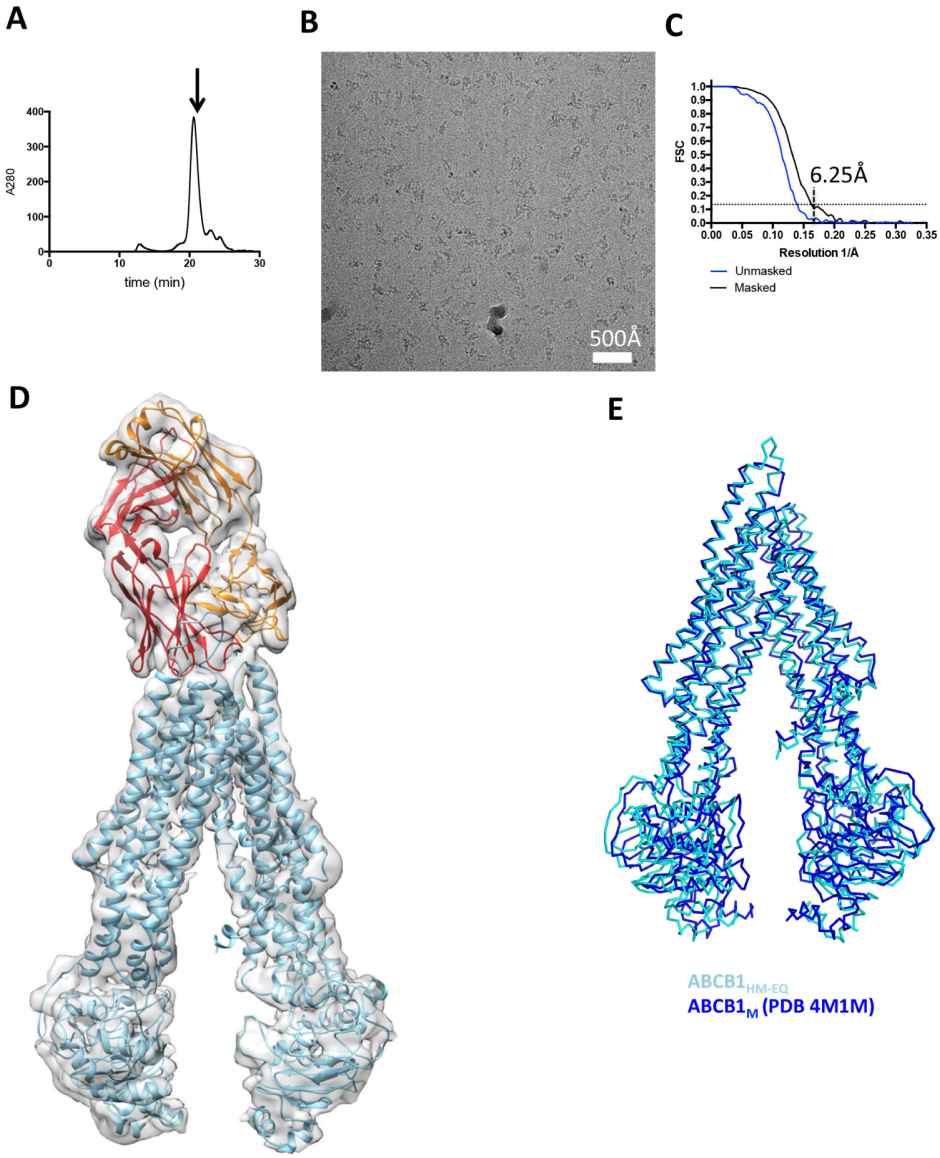


Figure 11: Cryo-EM analysis of ABCB1$_{HM}$-UIC2. A Size exclusion purification of amphipol-reconstituted ABCB1$_{HM}$-UIC2 complex, with arrow showing peak fraction used for grid preparation. B Representative micrograph with scale bar shown in white. C FSC curves of ABCB1$_{HM}$-UIC2 showing resolution estimate determined by 0.143 cutoff criterion (dashed lines). D Overall structure of ABCB1$_{HM}$-UIC2 complex showing inward-open ABCB1$_{H}$M (cyan ribbon) in complex with UIC2-Fab, whose heavy and light chains are colored red and orange, respectively. The EM density is shown as a transparent surface. E Superposition of inward open ABCB1$_{HM}$ (from our UIC2 complex structure) and mouse ABCB1 (ABCB1$_{M}$) (r.m.s.d for all aligned atoms = 1.88Å)

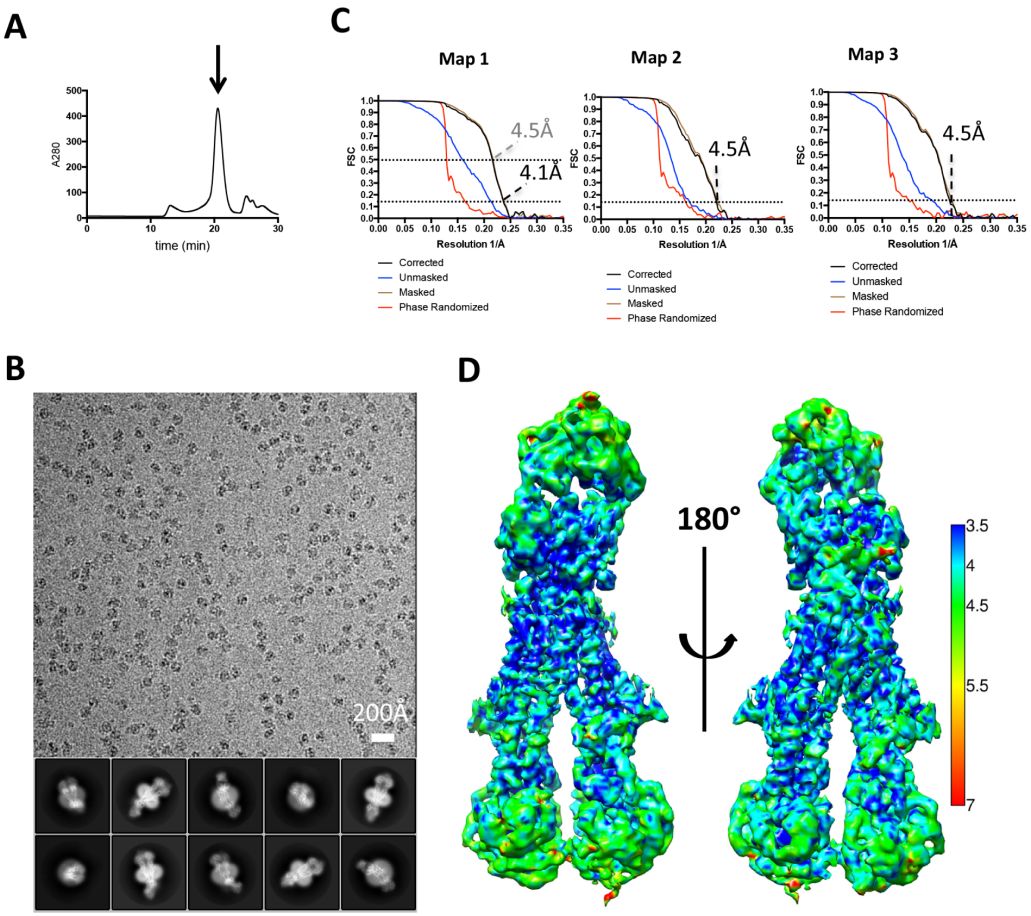


Figure 12: Cryo-EM analysis of disulfide-trapped apo ABCB1$_{HM-X}$-UIC2. A Size exclusion purification of detergent-purified ABCB1$_{HM-EQ}$-UIC2 complex with arrow showing peak fraction used for grid preparation. B Representative micrograph of cross-linked ABCB1$_{HM-X}$-UIC2 at -2.5µm defocus along with representative 2D classes. The scale bar is indicated in white. C FSC curves showing resolutions estimate determined by 0.143 and 0.5 cutoff criterion (black and grey dashed lines, respectively). D front and back views of cryo-EM volume colored according to local resolution estimate. The color key is shown on the right, numbers indicate Å resolution.

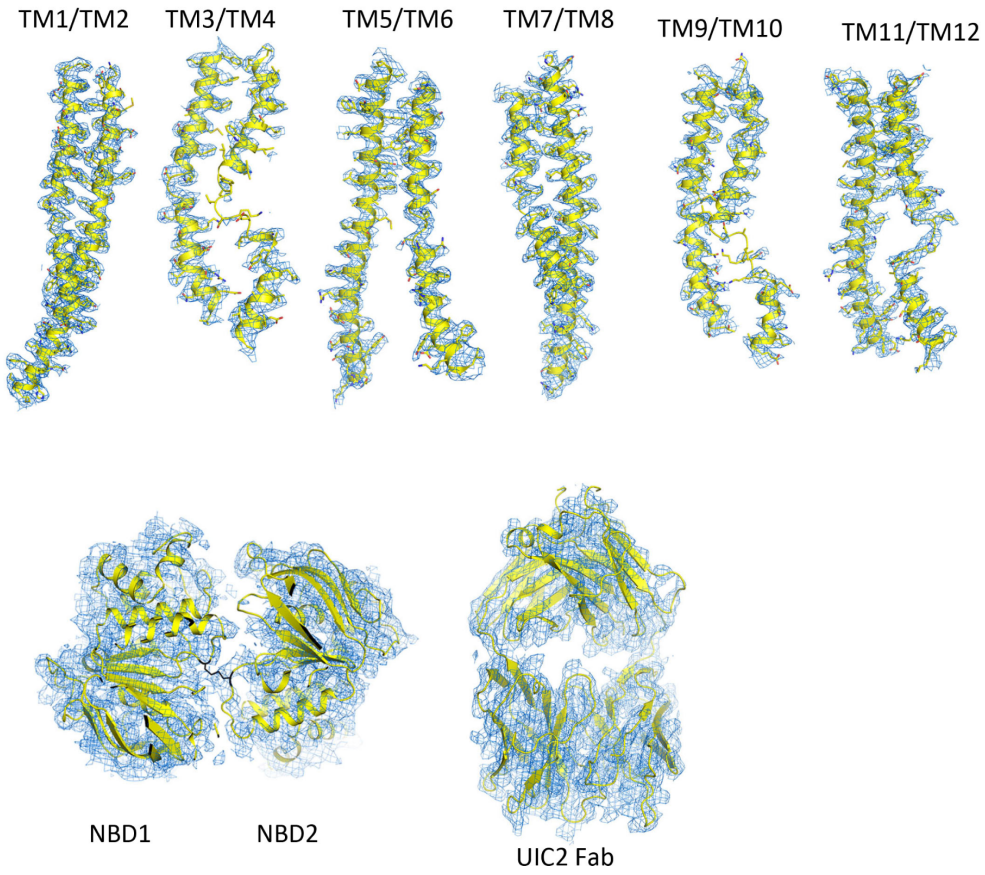


Figure 13: Quality of EM density (blue mesh) of the structure of disulfide-trapped apo ABCB1$_{HM-X}$-UIC2. Top, pairs of transmembrane domains are shown as ribbons (yellow), with selected side chains shown as sticks. Bottom, NBDs and UIC2-Fab are shown as ribbons. The introduced cysteine residues in both NBD D-loops are shown as black sticks.

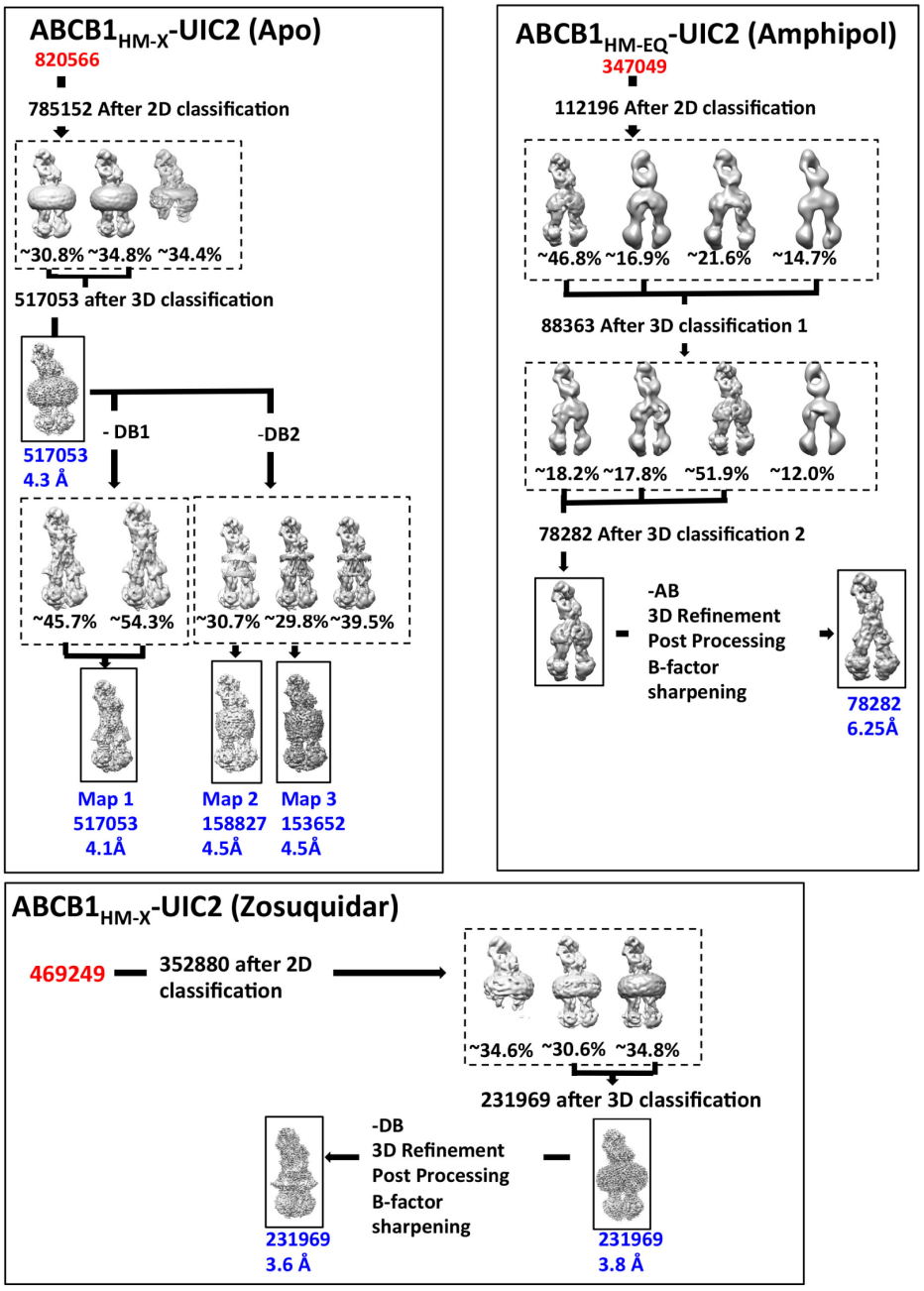


Figure 14: Pipeline of EM data processing and 3D classification for all datasets included in manuscript. Numbers in red starting set of all picked particles. 3D classification steps are boxed (dashed lines) and include the percentage of particles in each class indicated below the respective 3D classes. Final post processed maps are boxed (solid lines) with final number of particles and map resolution (blue text) indicated below each. −DB and −AB refer to subtraction of the detergent and amphipol belts, respectively.

| **Cryo-electron microscopy data collection** | | | | | |
|---|---|---|---|---|---|
| | $ABCB1_{HM-X}$-UIC2+ Zosuquidar | $ABCB1_{HM-X}$-UIC2 Apo | | | $ABCB1_{HM-EQ}$-UIC2 (Amphipol) |
| Microscope | FEI Titan Krios (1) | FEI Titan Krios (1) | | | FEI FEI Titan Krios (2) |
| Voltage (kV) | 300 | 300 | | | 300 |
| Camera | Gatan K2-Summit | Gatan K2 Summit | | | Gatan K2-Summit |
| Energy Filter | Gatan Quantum-LS (GIF) | Gatan Quantum-LS (GIF) | | | Gatan Quantum-LS (GIF) |
| Physical K2 pixel size (Å) | 0.84 | 1.387 | | | 1.336 |
| Defocus range (μm) | -0.2 - -4.8 | -0.2 - -5.2 | | | -1.4 - -2.5 |
| | | | | | |
| 3D reconstruction | | | | | |
| Number of micrographs | 2479 | 2614 | | | 2038 |
| Number of particles (3D Refinement) | 231969 | 517053 (Map 1) | 153652 (Map 2) | 158827 (Map 3) | 78282 |
| Resolution (Å) | 3.58 | 4.14 | 4.47 | 4.55 | 6.25 |
| Sharpening B-factor ($Å^2$) | -135 | -100 | -192 | -200 | -200 |
| Coordinate and B-factor refinement | | | | | |
| Number of protein atoms (non-H) | 12619 | 12609 | | | |
| Number of ligand atoms (non-H)<br>Zosuquidar<br>3PE<br>Glycans | 120<br><br>78<br>N/A<br>42 | 93<br><br>N/A<br>51<br>42 | | | |
| Mean B-factor protein atoms ($Å^2$) | 124.4 | 83 | | | |
| Mean B-factor ligand atoms ($Å^2$) | 49.7 | 99.3 | | | |
| RMSD bonds (Å) | 0.01 | 0.004 | | | |
| RMSD bond angles | 1.316 | 0.785 | | | |
| Map CC (whole map) | 0.5933 | 0.6142 | | | |
| Map CC (around atoms) | 0.7156 | 0.7180 | | | |
| FSC (Model, Map) | | | | | |
| Overall (entire box) | 0.5933 | 0.6142 | | | |
| Around atoms (masked) | 0.8059 | 0.8282 | | | |
| EM Ringer Score | 2.49 | 1.55 | | | |
| Molprobity Score<br>All atom clash score | 1.88<br>8.26 | 1.97<br>8.61 | | | |
| Ramachandran statistics<br>Favored (%)<br>Allowed (%)<br>Outliers (%) | <br><br>93.4<br>6.0<br>0.6 | <br><br>91.3<br>7.5<br>1.2 | | | |
| Rotamer Outliers (%) | 0.58 | 0 | | | |

**Table S1** Summary of Cryo-EM data and model parameters.

Figure 15: Summary of Cryo-EM data and model parameters.

# 3 Bile Salt Export Pump (BSEP)

The bile salt export pump (BSEP) belongs to the ATP binding cassette (ABC) superfamily. It is expressed in hepatocytes and is localized at the canalicular apical side. BSEP is the only transporter for conjugated monovalent bile salts into the bile. Bile salts facilitate digestion and absorption of dietary fat by formation of micelles with lipids. Inhibition of BSEP leads to reduced bile flow. This can cause accumulation of bile salts in the liver to a cytotoxic level. Thereby, BSEP deficiency can cause various genetic forms of cholestasis, such as progressive familial intrahepatic cholestasis type 2 (PFIC2), benign recurrent intrahepatic cholestasis type 2 (BRIC2) and drug-induced liver damage (DILI). To date, about 200 missense mutations in ABCB11, the gene encoding BSEP, have been reported. However, the phenotype-genotype correlation has not been clarified. In this work we present the first three structure based models of BSEP. BSEP bound to glibenclamide, a drug inhibiting BSEP function, and two structures in presence of substrate, describing different steps of the transport cycle. Potential models of the transport cycle are outlined in context of those models. Selected point mutations involved in disease conditions are pointed out and explained in context of the model. Despite the high sequence identity between BSEP and Pgp, these transporters show significantly different substrate specificity. While Pgp transport a host of substrates, BSEP transport is limited to monovalent conjugated bile salts. We show the presence of a loop reaching in the cavity on the cytosolic side. This could be an explanation for the strict selectivity of BSEP.

## Contents



## 3.1 Introduction

### 3.1.1 Enterohepatic Cycle: Release and Recovery of Bile Salts

Bile is a secretion produced by the liver. Its major components are water, conjugated bile salts and phospholipids. Further components are electrolytes,

cholesterol, alkaline phosphatase, lecithin, and metabolic products ([147]). Hepatocytes excrete bile components to the canaliculi, from where the bile flows to the gall bladder ([148]). Contraction of the gall bladder and subsequent bile flow to the duodenum is triggered by cholecystokinin, a peptide hormone acting on the smooth muscle cell of the gall bladder ([149]). Release of cholecystokinin is controlled by specialized cells in the duodenum, capable to perceive the presence of dietary fat. In the duodenum conjugated bile salts help to emulsify lipids. This increases the surface area for pancreatic lipases to break down dietary fat. The alkaline pH of bile neutralizes the acidic pH of the chyme and activates pancreatic lipases. Bile salts form mixed micelles with free fatty acids and fat-soluble vitamins. This is crucial for effective resorption in the duodenum and jejunum. The majority of bile salts are resorbed in the ileum the most distal segment of the thin intestine. Bile salt resorption is accomplished by the apical sodium-dependent bile acid cotransporter (ASBT) in an active process using the sodium gradient as driving force. Subsequently the heteromeric organic solute transporter (OST$\alpha$–OST$\beta$) transports the bile salts over the basolateral membrane into the blood stream ([150]). The hepatic portal system carries bile salts directly back to the liver. Sodium-taurocholate cotransorting polypeptide (NTCP) mediates uptake of bile salts into hepatocytes from where they are secreted over the canalicular membrane by the bile salt export pump (BSEP) ([151]). The circulation of bile salts and other substances from the liver into bile, followed by resorption in the small intestine and transport to the liver over the portal circulation is called enterohepatic circulation. This process is important for the recovery of bile salts, as a grown up person has a pool of bile salts of only 2-4 gram. This pool cycles several times a day to ensure a efficient uptake of fat from chyme. Daily up to 30 gram of bile salt are secreted to the gall bladder and reabsorbed ([148]). However only 0.5 grams are lost, what implies a recovery rate above 90% ([152]).

### 3.1.2 What Are Bile Salts?

Bile salts belong to the class of steroids. As such they contain 3 cyclohexane and a cyclopentyl ring. By IUPAC conventions the cyclohexane rings are labeled ring A, B, C and the cyclepentyl ring is labeled D. Hydroxygroups at C3, C7 and C12 render bile salts more polar than cholesterols. These hydroxyl groups point to the concave side adapted by the ring structure, whereas the methyl groups at positions 18 and 19 point to the convex side (Figure 16). This renders the concave side hydrophilic and the convex side lipophilic, causing surfactant properties of bile salts ([153]). The primary bile salts cholic acid and chenodeoxycholic acid are synthesized from cholesterol. At physiological pH the carboxyl group is ionized. Therefore bile acid and bile salt are the same

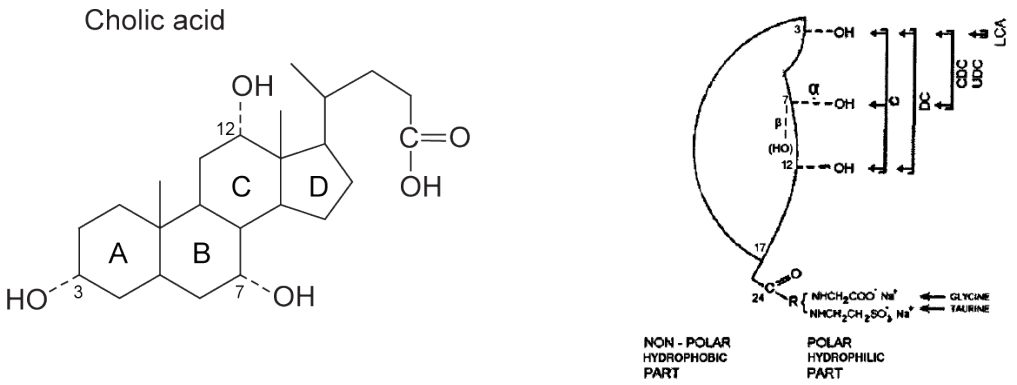


Figure 16: Chemical structure of cholic acid on the left, with labeled positions of hydroxy groups, cyclohexane, and cyclopentane rings. On the right a schematic drawing indicates the orientation of hydrophilic groups in 3D. ([154])

in a physiological context. For simplification we refer to them as bile salts. Conjugated bile salts consist of primary bile salt linked to glycine or taurine by an amide bond. Secondary bile salts are the result of bacterial modifications on conjugated bile salts in the colon. A fraction of bile salt not resorbed in the small intestine is modified by colonic microbiota and then recovered in the colon by passive absorption. Conjugation of bile salts decreases the pKa of a primary bile salt. This enhances the emulsifying capacity. Bile salts are essential for efficient uptake of dietary fat and fat-soluble vitamins. The surfactant property of bile salts emulsifies dietary fat to increase the surface for enzymatic digest. Mixed micelles of bile salts and lipophilic substances assist uptake of these lipophilic compounds. In addition bile salts are the major way for disposal of cholesterol in humans. This is important as humans lack the enzyme to catabolize sterols. On one hand loss of not resorbed bile salts is compensated by synthesis of bile salts from cholesterol. On the other hand cholesterol is also secreted BSEP independent into bile. In this case bile salts keep cholesterol soluble to prevent formation of gallstones. Due to their antimicrobial activity, mostly on gram-positive bacteria, bile salts regulate the bacterial growth and microbial composition in the gut. At higher concentration bile salts are cytotoxic. Therefore secretion to the gall bladder and formation of mixed micelles are required to protect hepatocytes. ([154], ([155])

### 3.1.3 Bile Salt Synthesis

Despite the high recovery rate of bile salts from the intestine, humans loose about 0.5 gram of bile salt per day. To keep the pool of available bile salts constant, new primary bile salt has to be synthesized de novo. This process takes place in hepatocytes. Starting product for the synthesis is cholesterol, which is transformed in several steps to cholyl-CoA or chenodeoxycholyl-CoA. The hydroxylation at position 7 by cholesterol 7α-hydroxylase is the first and rate-limiting step of this pathway. At the third step the pathway bifurcates and 7α-Hydroxy-4-cholesten-3-one can either react with 7α-hydroxy-4-cholesten-3-one 12α-monooxygenase to build cholyl-CoA as a final product or it can react with sterol 12α-hydroxylase to follow the pathway leading to chenodeoxycholyl-CoA. The ratio of chenodeoxycholate and cholate is regulated by the activity of sterol 12α-hydroxylase. In addition, alternative pathways exist to build chenodeoxycholyl-CoA from cholesterol. As last step bile acid-CoA:amino acid N-acyltransferase conjugates primary bile salts by the formation of an amide bond between the primary bile salt carboxyl group and the amine of a glycine or taurine. This leads to the 4 major conjugated bile salts glycocholic acid, taurocholic acid, glycochenodeoxycholic acid and taurochenodeoxycholic acid. De novo synthesis of bile salts is a complicated and slow process. Therefore this process cannot compensate for impaired recovery of bile salts in the ileum. ([154], ([155])

### 3.1.4 BSEP and Secretion of Bile Salts into Bile

The bile salt export pump (BSEP) is an ATP dependent bile salt transporter in the canalicular membrane. It belongs to the ATP-binding cassette transporter family, in particular to the MDR/TAP subfamily. Context dependent it can be named BSEP, ABCB11 or sister of P-glycoprotein (s-Pgp). The name s-Pgp refers to the high sequence identity of BSEP to Pgp found, when it was identified at the canalicular membrane the first time. Sequence alignment of BSEP indicates a high similarity of the N- and C-terminal half. Alignments and secondary structure prediction propose that BSEP forms a pseudo-symmetric full transporter with six transmembrane helices and a nucleotide binding domain (NBD) followed by another six transmembrane helices and a second NBD ([156]). According to sequence alignments NBD1 should be able to bind ATP, but incapable of hydrolyzing it due to a degeneration in the walker B motif, where M584 replaces the catalytically crucial glutamate. BSEP is presumed to be the rate limiting step in hepatocellular bile salt secretion. Compared to Pgp, BSEP has a very large extracellular loop between transmembrane domain 1 (TMD1) and TMD2. On this loop four potential N-linked glycosylation sites are identified. The four sites N109, N116, N122 and N125 were shown to

be glycosylated in a biochemical approach. Removal of glycans decreases the biochemical half-life and thereby reduces the measured transport activity of BSEP. While mutants of N109 and N116 still target the apical plasma membrane, mutation of an additional glycosylation site leads to retention of BSEP ([157]). Substrates for transport by BSEP are conjugated bile salts. Primary bile salts and cholesterol are not or not efficiently transported by BSEP. For cholesterol other transporters in the canalicular membrane account for. The transport path of bile salts across hepatocytes to the canalicular membrane is not fully understood yet. However, multiple proteins are known to bind bile salts and to potentially shuttle them through the cell for secretion by BSEP such as 3α-hydroxysteroid dehydrogenase (3α-HSD), glutathione-S-transferase (GST) and fatty acid binding protein (FABP) ([158], [159]).

### 3.1.5 Other Transporters of The Canalicular Membrane

At the canalicular membrane of hepatocytes many transporters work side by side. Some of them have a very broad range of substrate, whereas others are rather specific. Aside from BSEP we find ABCB1, ABCB4, ABCC2, and ABCG5/ABCG8. These are the principal transporters at the canalicular membrane ([152]).

**ABCB1** is a transporter for xenobiotics. It has a broad range of substrates. Intriguingly ABCB1 shares a very high sequence identity with BSEP of 51%. Therefore substrates for ABCB1 can easily show affinity for BSEP and act as inhibitor. More details for ABCB1 can be found in Chapter 2.

**ABCB4** is a phospholipid transporter, selective for phosphatidylcholine. Malfunction of ABCB4 causes progressive familial intrahepatic cholestasis type 3 (PFIC3). Phospholipids transported by ABCB4 over the canalicular membrane form mixed micelles with bile salts, reducing bile salt toxicity. This is important to protect cholangiocytes and cholecystocytes, the epithelial cells in the bile duct and gall bladder. ([160])

**ABCC2** is also known as canalicular multispecific organic anion transporter 1. It has a very wide substrate range and excretes numerous organic anions including bilirubin conjugates from the cytoplasm across the canalicular membrane. Apparently it can cotransport uncharged compound with glutathione. ([161]).

**Sterolin:** The heterodimer of ABCG5 and ABCG8 forms the sterol pump sterolin. Apparently other sterols than cholesterol can be excreted too. Excretion of cholesterol and bile salts has to be in balance. Otherwise cholesterol precipitates and forms gallstones. ([162])

### 3.1.6 Diseases Associated With Mutations in BSEP

Cholestasis is a condition where bile flow is strongly reduced or completely abolished. The most common cause for cholestasis are gallstones blocking the bile duct. This type is called obstructive cholestasis. In case of a metabolic type of cholestasis, bile formation in the liver is impaired. This condition can be caused by mutations in transporters involved in bile formation or by interference with those transporters. This type is often referred to as intrahepatic cholestasis. To date two diseases are connected to mutations in the gene Abcb11 coding for BSEP ([152]). ([163])

**BRIC:** Benign recurrent intrahepatic cholestasis (BRIC) type 2 is a benign disease caused by mutations in Abcb11. Episodes of cholestasis from weeks to months are followed by episodes without symptoms for weeks or years. The first episode of cholestasis takes places in the second or third decade of a patients live. Symptoms for BRIC episode are itchiness (pruritus), yellowing of skin and eyes (jaundice), discomfort, nausea, lack of appetite, excess fat in feces and in long-lasting episodes of cholestasis a shortage of fat soluble vitamins. BRIC can be induced by mutations in various genes; type 2 is caused by a deficiency of BSEP. Normally patients can regenerate during symptom free episodes and do not develop a progressive disease. ([164])

**PFIC:** Progressive familial intrahepatic cholestasis (PFIC) type 2 is the severe form of cholestasis triggered by BSEP malfunction. In contrary to BRIC the symptoms show up within the first ten years of life. In some cases cholestasis manifests in the very first year of a patients life. The disease develops progressively and leads to liver disease and finally liver failure. In patients with PFIC type 2 liver failure develops within the first few years of life. It is assumed that liver failure is induced by bile salt accumulation in hepatocytes. Especially on mitochondria bile salts show a toxic effect.

BRIC and PFIC can be considered to be part of a spectrum of intrahepatic cholestasis disorders of varying severity. In BRIC type 2 bile salt transport is impaired, whereas in PFIC type 2 transport is abolished. This can be caused by changes in BSEP activity or by an impaired trafficking of BSEP in the cell, reducing abundance of the transporter at the canalicular membrane. While PFIC, including all types, is very rare with 1 case in 50'000 to 100'000 people, BRIC is even less frequent. ([165])

### 3.1.7 Interactions of Drugs With BSEP and Triggered Cholestasis

Apart from mutation derived BRIC and PFIC conditions, there are cases of intrahepatic cholestasis triggered by drugs ([166]). A variety of drugs have been found to be able to block BSEP as adverse effect. This can lead to drug induced liver injury. Drugs as cyclosporin A, rifampicin, bosentan, and glibenclamide have been shown to be competitive inhibitors of BSEP ([167]. Furthermore bosentan has been shown to increased the plasma level of bile salts in a reversible way, accompanied by transaminase elevations in blood plasma, a marker for liver injury ([168]). While detecting the inhibitory action on BSEP is straightforward for some drugs, it can be more complicated in other cases. Ethinylestradiol shows no sign of BSEP inhibition in some test. Only if BSEP is coexpressed with MRP2 an inhibition can be detected. Apparently MRP2 transports ethinylestradiol over the canalicular membrane. Solely from the luminal side ethinylestradiol can inhibit transportation of conjugated cholates ([167], [169]). Drug induced cholestasis is clinically relevant, but still rather rare. There are indications for genetic risk factors for drug induced cholestasis. Two single nucleotide polymorphisms (SNPs) associated with drug induced cholestasis are c.1331T>C (p.V444A) and c.2029A>G (p.M677V). These variants have the same transport activity, but lead to a lower abundance of BSEP at the canalicular membrane. This is a possible explanation for a higher susceptibility for drug induced cholestasis in the genetic background of SNP c.1331T>C and c.2029A>G. ([170])

## 3.2 Results

This work on BSEP is an ongoing project in collaboration with Lancien Loïck and Kaspar Locher at ETH Zürich. Expression and purification of BSEP as well as functional assays are performed by Lancien Loïck. Because results of this project are not published yet, Loïcks data are not shown here. Results are restrained to following four structures obtained from three different samples. BSEP_glibenclamide represents wild type BSEP inhibited by the antidiabetic drug glibenclamide. BSEPeqATP is inactivated by a glutamate to glutamine (EQ) mutation in the walker B motive. This mutation still allows binding, but disables hydrolysis of ATP. BSEPeqATP_closed and BSEPeqATP_CL represent two different structures, derived from independent purifications of BSEP harboring an EQ mutation in presence of ATP and taurocholate. All samples are prepared in HEK cells and purified in n-Decyl-β-D-Maltopyranoside.

My contribution to this work comprised data collection, processing, model building, and interpretation as written in this chapter.

### 3.2.1 Data Collection, Processings, and Model Building

All datasets were collected as image stacks comprising 50 frames at a nominal magnification of 165,000× in super-resolution mode with an estimated dose per frame of 2-2.5 electron per square angstrom, corresponding to a total dose of 100-125 electrons per square angstrom. The software suite Focus ([139]) was used for data pruning and preprocessing, applying twofold binning of the recorded micrographs to a calibrated pixel size of 0.831Å, motion correction with MotionCor2 [131] and CTF estimation with CTFFIND4. Particles were picked with gAUTOMATCH ([140]) initially without template, followed by a template-based approach. Templates were created from the initial reconstruction using e2proc2d.py (EMAN2) ([141]). Therefore Relion 3D initial model was used to generate a starting model. Micrographs were exported to scicore for processing in Relion. For BSEP in presence of the inhibitor glibenclamide (BSEP_glib) a total of 579,628 particles were extracted using a box size of 250px from 11,589 micrographs, followed by three rounds of 2D classification, to yield a particle set of 390,372 particles. After one round of 3D classification, the remaining 179,782 particles from the major of four classes were used for 3D auto-refinement and postprocessing. Relion postprocess reported an estimated resolution of 3.7Å. For processing Relion version 2.0.4 was used. Due to a bug affecting this version, the resolution of 3.7Å cannot be claimed as gold standard resolution. Processing was repeated with a fixed version of Relion (2.1b1), resulting in a resolution of 4.1Å. The map generated by the bugged version shows only light signs of overfitting mostly in the worse resolved NBDs

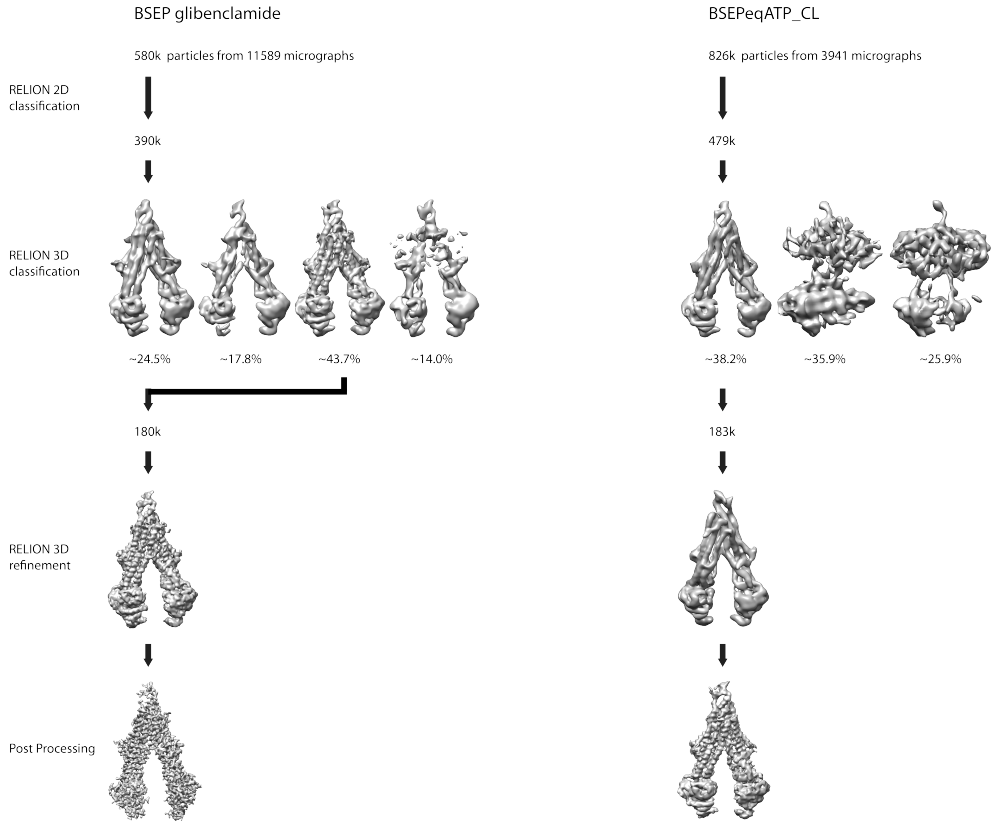


Figure 17: Pipeline of EM data processing for the datasets of BSEP in presence of glibenclamide (BSEP_glib) and BSEP with an glutamate to glutamine mutation in presence of MgATP and taurocholate adopting a seemingly open conformation (BSEPeqATP_CL). Arrows indicate which classes were used in the subsequent step.

and is in good agreement with the map from Relion 2.1b1. Therefore model building was performed on the initial map, which showed significantly more details consistent with sidechains of the model and a clear helical pitch. For all other datasets the fixed version of Relion was used only.
For the map of BSEPeqATP_CL 826,072 particles were picked from 3941 micrographs. Most of those were actually not particles of BSEP, but detergent micelles. Two rounds of 2D classification could remove most micelles, reducing the particle set to 478,758 particles. In 3D classification remaining micelles and broken particles were removed. A set of 183,457 particles from the best class could finally be refined to a resolution of 4.8Å. For extraction a box size of 384px was used for all samples except for BSEP_glib. For speed improvements

particles were binned 3× for classification runs. Figure 17 shows an overall scheme for data processing of BSEP_glib and BSEPeqATP_CL.
For BSEPeqATP_closed 3504 micrographs were recorded. An initial set of 253,677 particles was reduced to 125,043 in a singe round of 2D classification. Subsequent 3D classification with three classes led to a major class in closed conformation. 73,121 particles from this class could be refined and postprocessed to a resolution of 5.1Å.
Micrographs of BSEPeqATP showed a very low concentration of particles, but many micelles. In order to miss no particle all micelles and particles were boxed. As 2D classification did not work well due to the high number of micelles in the particle set and due to the proximity of micelles to boxed BSEL particles, only ice contaminations and boxes on the carbon edge were removed by 2D classification. This reduced the set of 978,783 particles from 3754 micrographs to 813,720 particles. 3D classification using a low-pass filtered map of BSEP_glib with a mask successfully separated real BSEP particles from detergent micelles. Remaining 94,452 particles were sent to another round of 3D classification using four classes. Particles of the two major open classes were combined and refined. The resolution of the postprocessed map reached 7.3Å. Figure 18 shows an overall data processing scheme for BSEPeqATP_closed and BSEPeqATP.
For model building a model of Pgp (pdb:3g5u) was morphed into the map of BSEP_glib, using iMODfit ([171]). The morphed model was then used to trace the chain. Transmembrane domains and loops could be build manually de-novo in Coot [142]. For NBDs the domains of our ABCB1 model (pdb:6fn1) were fitted using iMODfit, followed by a local refinement. The model was then refined in phenix [144] followed by manual corrections. Molprobity reported an all-atom clashscore of 6.4%, ramachandran plot outliers of only 0.67% and 90,4% in favored region. Phenix was used to convert the refined map into MTZ format to allow in-situ adjustments of B-factor sharpening. For other maps the model build in BSEP_glib was morphed into position by iMODfit, and refined in phenix and manually in Coot.

### 3.2.2 Structure of BSEP Bound to Glibenclamide

The structure of BSEP in complex with glibenclamide was solved at a gold-standard resolution of 4.1Å. Particles of this sample adapted a wide range of conformations from wide open to rather closed. The classification of different conformations was therefore not possible. The best resolution could be obtained with all particles refined together in one class. The map of BSEP with glibenclamide displays a inward open conformation. A total of 12 transmembrane domains (TMDs) build two bundles. Bundle A comprises H1,2,3,6,10,11,

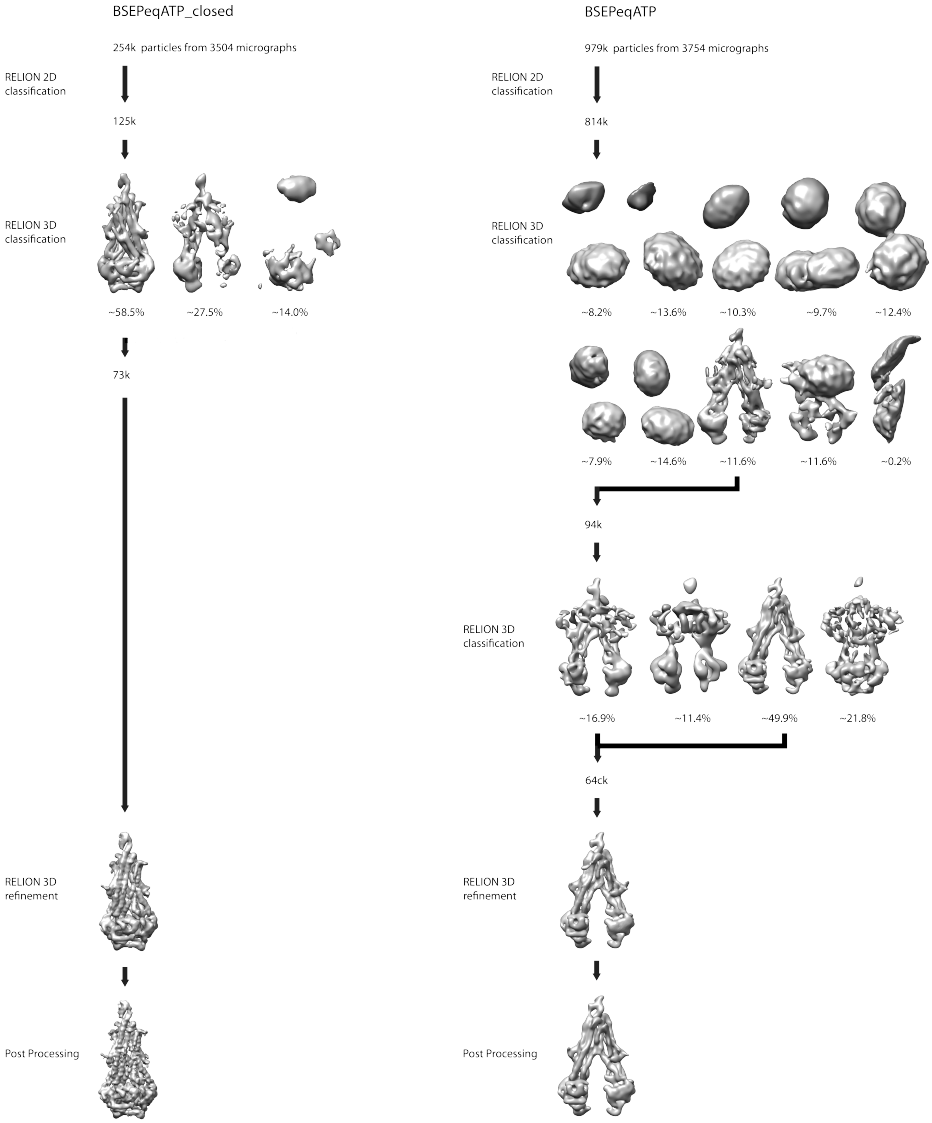


Figure 18: Pipeline of EM data processing for the datasets of BSEP with an glutamate to glutamine mutation in presence of MgATP and taurocholate adopting a closed conformation and (BSEPeqATP_closed) and the same construct in the absence of taurocholate (BSEPeqATP). Arrows indicate which classes were used in the subsequent step.

whereas H4,5,7,8,9,12 build bundle B. The two bundles are opened to the cytosolic side by an opening angle of 37°. The resolution in transmembrane domains allowed an unambiguous placement of the polypeptide chain. Loops were more difficult to fit, but could be build de novo after all. Due to the flexibility of BSEP, nucleotide-binding domains (NBDs) could not be build de novo. NBDs from ABCB1 model (PDB:6fn1) were fitted individually to the densities and refined locally. The connection between H1 and H2 adapts a beta-turn-beta-loop structure. This motif is a new feature not found in related ABCB transporters so far. The subsequent helix 2 shows less side chain densities, probably due to an increased flexibility, based on the loop. At a low threshold densities for two glycosylations can be observed. One glycosylation site collocates with N109. A second glycosylation is detected for N116. No densities were observable for potential glycosylation sites N122 and N125, but N125 makes a contact to E96 on helix 1 instead. In the most extracellular region of the cavity formed by BSEP an additional density is observable. A single molecule of glibenclamide can be fitted in this density. Despite the limited resolution, the orientation of glibenclamide is unambiguous. Coordination of glibenclamide by sidechains of H1 (F83), H2 (Y145), H6 (V368 and L364), H7 (Y772, F776), H11 (N996 and Y1000), and H12 (F1018) is consistent. Additional densities in the cavity close to glibenclamide are observable, but not part of the drug not the protein. As expected no further densities matching ATP of taurocholate were detected. For simplicity we refer to this model as BSEL_glib.

### 3.2.3 Structure of BSEP$_{EQ}$ATP with Taurocholate

BSEP with an E to Q point mutation in the Walker B motif adapted 2 different conformations in presence of MgATP. Particles of one sample preparation led to a map in closed conformation (BSEP$_{EQ}$ATP_closed). This dataset could be refined to an overall resolution of 5.1Å. Bundle A and bundle B have a opening angle of only 20°. The model shows no access to the internal cavity, neither from the internal, nor from the external site. From bundle A only H10 has missing densities, whereas from bundle B all helices have missing densities, especially in the external facing TMS portion. Despite sample preparation in presence of taurocholate and ATP, no additional density for taurocholate could be found in the map. Two ATP molecules can be placed in the NBD densities, using the outward facing map of ABCB1 (PDB:6c0v) as template. Domains interacting with glibenclamide in the inhibitor bound map are packed very tightly but interact only sparsely with each other. Encountered contacts are Y145 with N996, Y83 with F1018, and Y772 with M805.
Particles from the other sample preparation gave rise to a map of BSEP in a

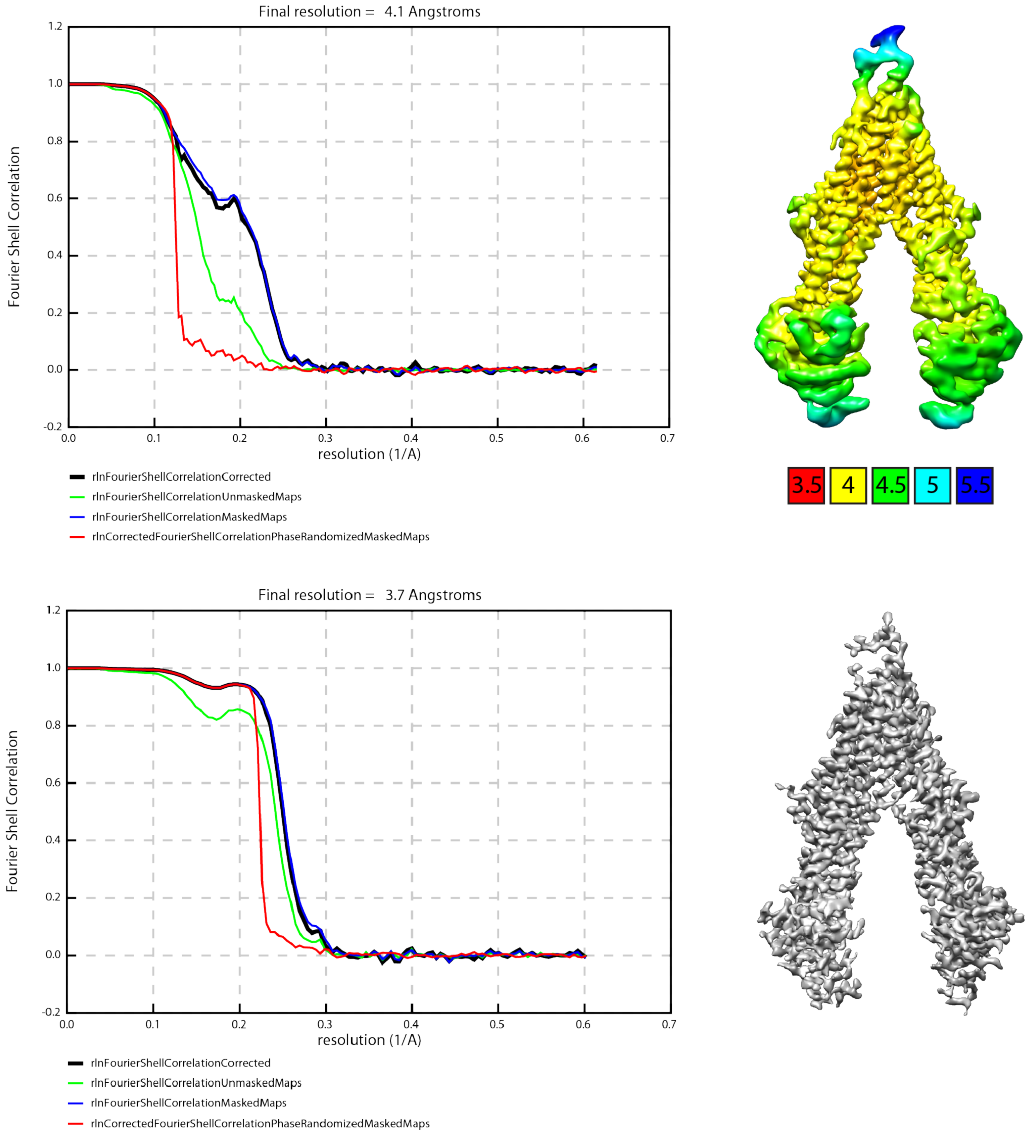


Figure 19: Resolution estimation of BSEP_glib after refinement with Relion2.0.4 on top and Relion2.1b1 on bottom. Due to a bug in versions 2.0.4 the reported resolution does not fulfill gold standard. Owing to additional details the higher resolution map was used for model building, though the lower resolution estimate has to be claimed. FSC curves on the left indicate resolution estimate determined by 0.143 cutoff criterion. The volume on the right shows local resolution estimated in Relion.

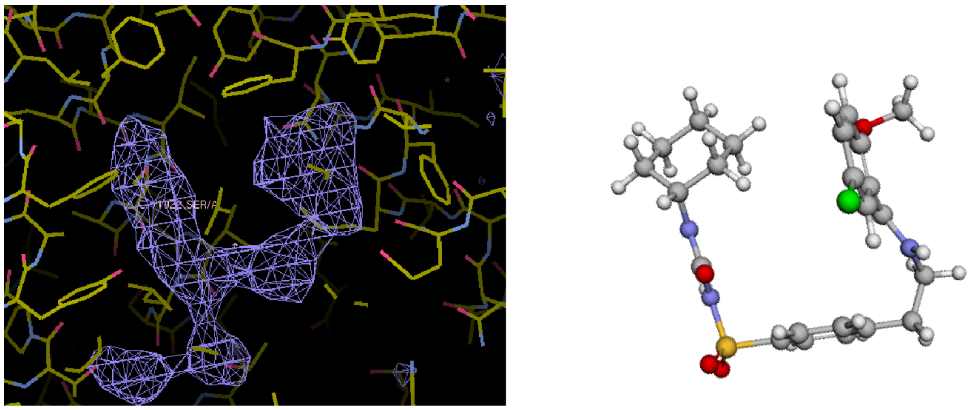

Figure 20: On the left the difference density accounting for glibenclamide bound in the cytosol facing cavity of BSEP_glib is depicted. Additional densities are in proximity to the sulfonyl group of glibenclamide and might represent coordinated water or ions. On the right a model of glibenclamide is shown.

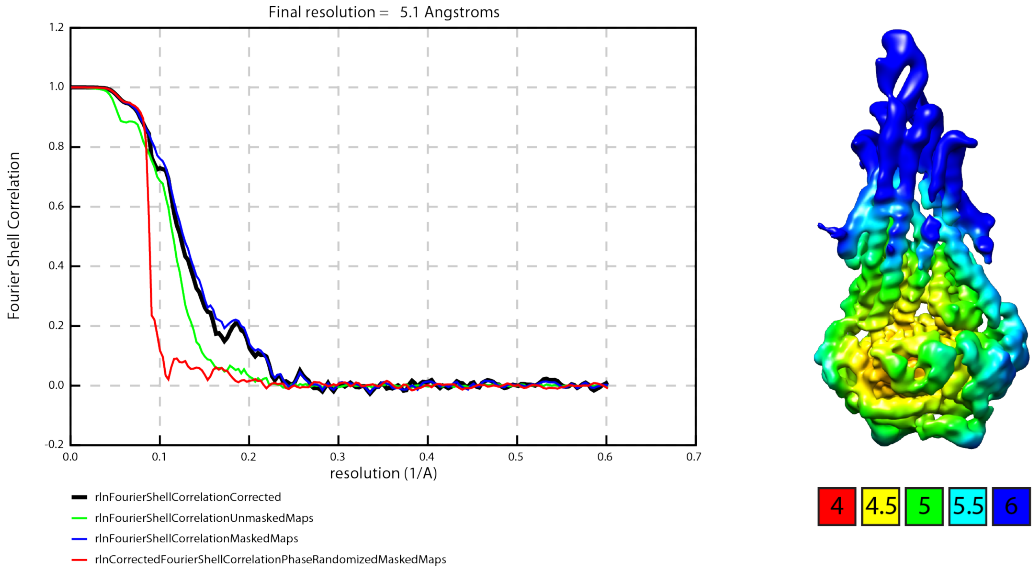


Figure 21: Resolution estimation of BSEPeqATP_closed: FSC curves on the left indicate resolution estimate determined by 0.143 cutoff criterion. The volume on the right shows local resolution estimated in relion.

seemingly open conformation. Bundle A and bundle B have an opening angle of 40°. This map could be refined to a resolution of 4.8Å (Figure 21). TMDs colocalize very well with the model build in the glibenclamide bound map. Surprisingly, an additional density shows up in the central cavity. This additional density forms a helix directing from the internal to the external side, followed by a turn induced by two succeeding prolines. A stretch of coil connects this density to the shoulder helix starting the second half of BSEP. We refer to this density as the connecting loop (CL) as it is part of the connection between the N- and C-terminal half of BSEP. The ABTMpro server (SSpro/SSpro8) predicts corresponding amino acid sequence to form a α-helix in the N-terminal and coil in the C-terminal part (Figure 22C). The sequence is clearly predicted to be not a TMD. The turn region of this additional density interacts with residues Y772, Y1000, Y772, F83, F776, F993, F1018, N996, Q76, V368 M992, and L364. Most of these residues interact with glibenclamide in BSEP-glib. In Proximity of the CL α-helix the helix bundles A and B separate in the membrane area. There an additional density shows up between H4 and H6, facing the detergent region as well. Taurocholate fits to this density, directing the hydrophobic surface towards the very hydrophobic helix 4. The hydroxygroup at position C3 points towards S249 of H4, whereas hydroxygroups at position C7 and C12 on the hydrophilic site face the slightly more hydrophilic helix 6 (Figure 22B and D). The conjugated taurine is surrounded by charged residues E381 of helix 6, R696 and K700 of the CL helix, E723 and K726 of CL coil. In NBD2 a density is present giving a potential fit of ATP. Due to the bad local resolution in the NBDs the fit of ATP is not very good. For simplicity we refer to this model as BSEP$_{EQ}$ATP_CL.

### 3.2.4 Structure of BSEP$_{EQ}$ATP without Taurocholate

Most particles of BSEP with an E to Q mutation bound to ATP adapt a conformation similar to BSEPqeATP_CL. Due to the low resolution of this map interpretation are not easy. The most interesting feature we see is the helix of the CL sitting in the cytosolic facing cavity. The coil directing back is not visible presumably owed to the resolution.

## 3.3 Discussion

### 3.3.1 Glycosylation of BSEP

Based on our data we conclude that in human BSEP only the first two of four potential glycosylation sites are actually glycosylated. This is in disagreement with biochemical experiments performed on rat BSEP in the lab of Irwin M. Arias ([157]). In principle this inconsistency can be explained by differences

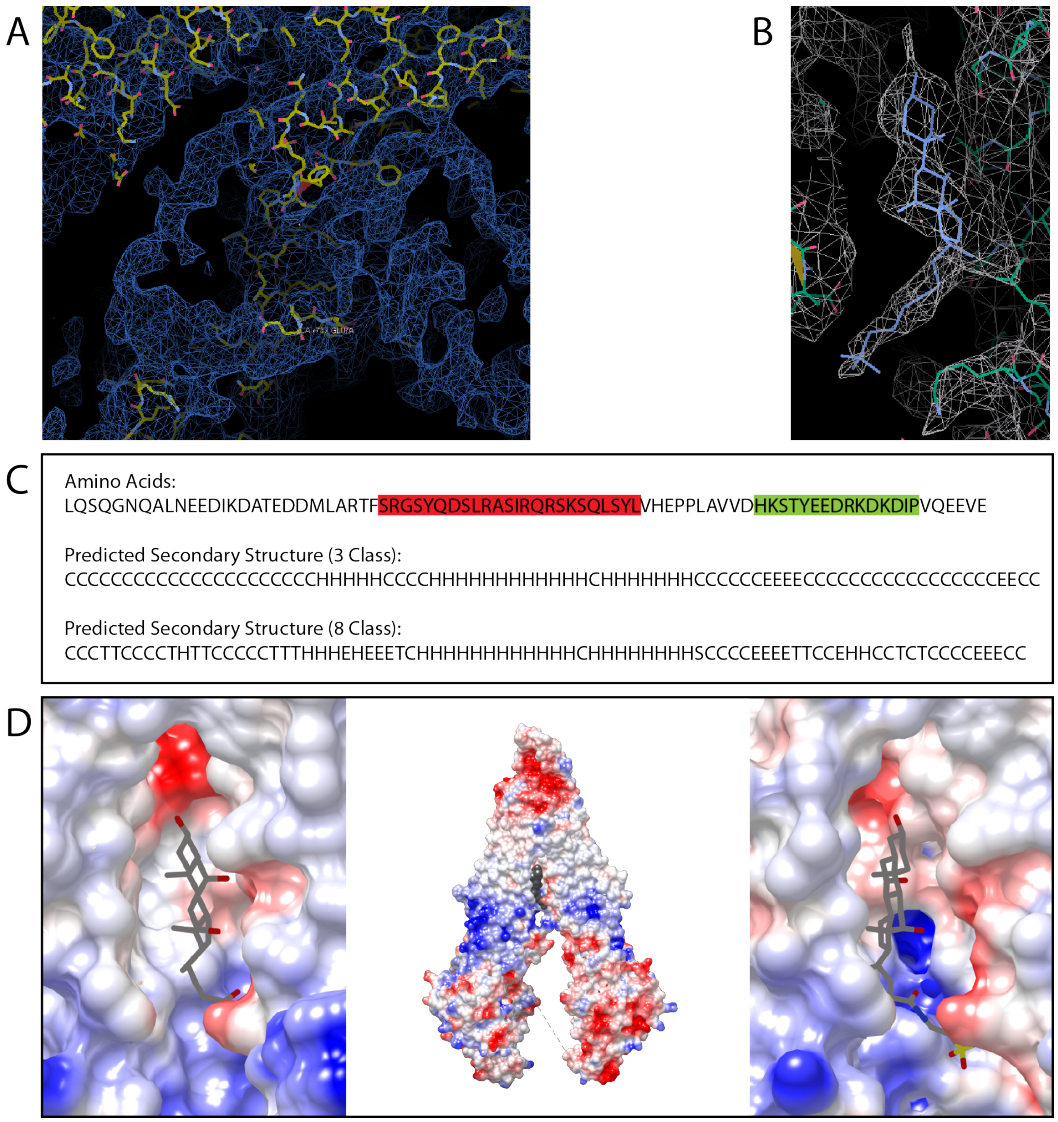


Figure 22: **(A)** Density for the CL leaving the cavity and directing to glutamate E737, the starting point of the C-terminal half of BSEP as it could be build in the map of BSEP_glib. **(B)** Taurocholate placed in the density between helix 4 and 6. **(C)** Secondary structure prediction of the CL using ABTMpro. The α-helix build in our density is marked red, whereas green marks the coil region found in BSEPeqATP_CL. The single letter code of the prediction is H (α-helix), C (coil), E (extended strand), T (turn), and S (bend). **(D)** Taurocholate sitting between helix 4 and 6. The left panel is focusing on the hydrophobic and the right on the hydrophilic side. The central representation shows taurocholate positioned in the observed binding site. The color code from blue to red indicates the coulomb potential calculated in Chimera from blue (-10), light blue (-5), white, light red (+5) to red (+10) in kcal/(mol·e)

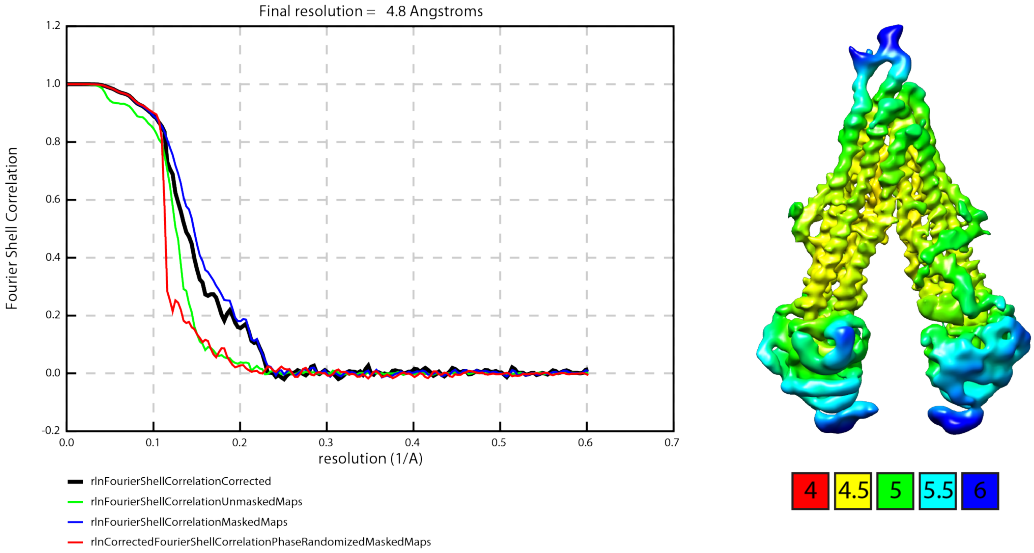


Figure 23: Resolution estimation of BSEPeqATP_CL: FSC curves on the left indicate resolution estimate determined by 0.143 cutoff criterion. The volume on the right shows local resolution estimated in relion.

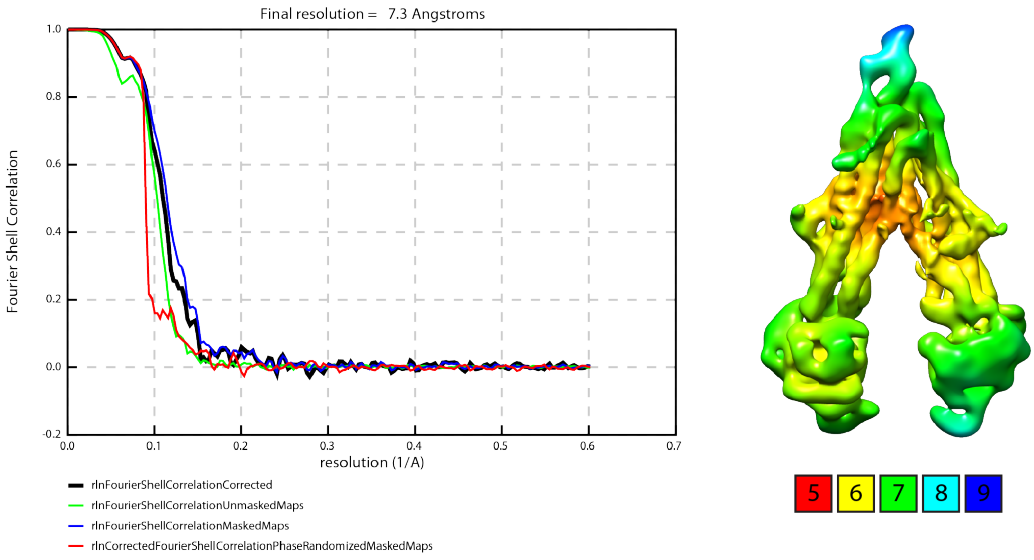


Figure 24: Resolution estimation of BSEPeqATP: FSC curves on the left indicate resolution estimate determined by 0.143 cutoff criterion. The volume on the right shows local resolution estimated in relion.

in glycosylation between human BSEP and the rat homolog used for the biochemical approach. Another reason could be the different expression system, as rat BSEP was expressed in MDCK II cells, whereas human BSEP for our experiments is expressed in HEK-293 cells. Nevertheless the extracellular loop between helix 1 and 2 is highly conserved (Figure 25A) and therefore these prior biochemical results should be reviewed. The glycosylation profile of rat BSEP (Figure 25B) shows a reduction in molecular weight for BSEP harboring mutated glycosylation sites. Thereby potentially glycosylated asparagine residues were mutated to glutamine. For wild type and glycosylated versions, a second band at a lower molecular weight appears. This band is interpreted as core glycosylated BSEP. This represents BSEP with the initial immature glycosylation. The same two bands are detectable in the half-life experiment, marked as C and D band. Intriguingly, a second band is visible in the quadruple mutated BSEP too (Figure 25D). Figure 25C shows expression levels of BSEP constructs. For wild type, single and double mutant BSEP, the decrease in molecular weight is consistent with the assumed loss of glycans. But For the triple mutant BSEP only the lower band initially interpreted as core glycosylated BSEP is detectable. For quadruple mutant BSEP no band is detectable. Bands of Figure 25C are not in ratio with those shown in Figure 25B. The signal for triple and quadruple mutated BSEP in Figure 25B is too strong compared to wild type, single and double mutant BSEP, even taking into account that sample amount for triple and quadruple mutated BSEP is 4 times larger than for wild type, single and double mutant. We can therefore not be sure that the bands for triple and quadruple mutants derive from the BSEP mutant. Analysis of different numbers and combinations of mutations showed a strong correlation between the number of mutations and expression levels. With up to two mutations BSEP expression is still good, but not in triple mutants. Unfortunately not all 16 combinations were tested. This implies a pivotal stabilizing effect of N122, though we cannot see a reasoning in our model. On the other hand a mutation of N125 has more adverse effects than mutating N122. This is in agreement with our structure. To clarify the impact of the four potential glycosylation sites, corresponding experiments need to be repeated. In addition to the 16 N to Q knock out combinations, a mutation of T124 and T127 should be tested. This would change the Asn - X - Thr/Ser glycosylation consensus sequence of N122 and N125, without replacing the asparagine. Therefore potential interactions of the asparagine side chain would stay preserved.

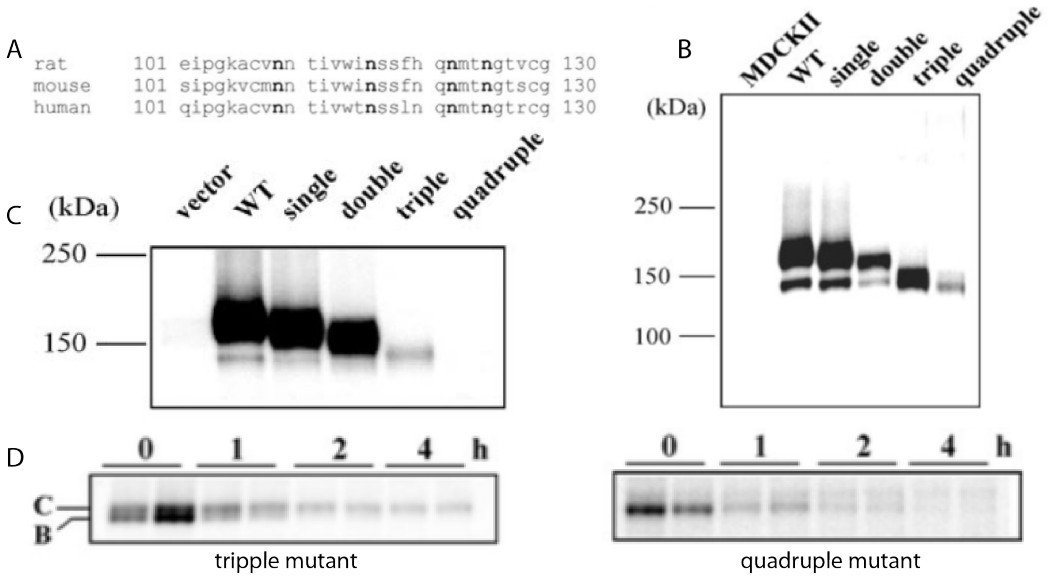


Figure 25: All panels are taken from [157] **(A)** Sequence alignment of BSEP covering the extracellular loop between helix 1 and 2. Potential glycosylation sites are marked bold. **(B)** Difference of the molecular weight of wild type BSEP and single, double, triple, and quadruple glycosylation site KO constructs. **(C)** Basically the same experiment as in B, but with equal amounts loaded in every lane. **(D)** Biochemical half-lives experiment showing degradation of triple and quadruple mutant BSEP. Quadruple mutants show an unexpected second band, which might have been misinterpreted.

### 3.3.2 BSEP Inhibition by Glibenclamide

The map of BSEP inhibited by glibenclamide on its own looks straightforward for interpretation. BSEP is in an inward open conformation and glibenclamide sits in the cavity, blocking either the gateway for bile salt transport or locks BSEP in an inward open conformation. The map of $BSEP_{EQ}$ATP_closed supports the idea of locking the inward open conformation, as in this structure residues involved in coordinating glibenclamide are packed very tightly. In this conformation no ligand could bind in this location. The map of $BSEP_{EQ}$ATP_CL on the other hand shows a direct interaction of the CL with most residues involved in glibenclamide coordination. Assuming that the CL is involved in the transport of bile salts, blocking access to this side by glibenclamide represents a convincing model for inhibition.

### 3.3.3 Bile Salt Transport

Most reliable information for the transport of bile salts we obtain from $BSEP_{EQ}$ATP _CL. In this map we see densities for ATP bound to NBDs and a single molecule of taurocholate near the BSEP-detergent interface. The placement of taurocholate might seem unexpected at a first glance. But taking into account the detergent property of bile salts, a transport passing the protein-lipid interface is not that unlikely. Access form the cytosolic side is blocked by the CL reaching into the cavity formed by bundle A and B. Taken together $BSEP_{EQ}$ATP_CL shows BSEP in an occluded state in the middle of a transport cycle. In BSEP_glib, neither ATP nor taurocholate is present. The overall conformation is still similar to $BSEP_{EQ}$ATP_CL. The main difference is the missing CL reaching into the cavity of BSEP. In fact, no density is observable from this loop at all. This conformation is induced or stabilized by glibenclamide blocking the CL out of the cavity. This gives a potential opening for bile salt access. It is not clear if this structure represents a real state of the transport cycle, stabilized by glibenclamide or if we see a non-native conformation induced by glibenclamide binding. Further structural data of BSEP without ATP, taurocholate and glibenclamide could give more insight, but is difficult to obtain due to the low stability and flexibility of BSEP in complete absence of ligands. Based on our maps, various models can be assumed for bile salt transport. Most promising models are illustrated in Figure 26. The most convincing model assumes a spontaneous entry of bile salts into the inner leaflet of the plasma membrane. From there bile salt can access BSEP similar to the vacuum cleaner model ([21]). As taurocholate is still bound to BSEP in the map of BSEPeqATP_CL we have to assume that not only ATP binding, but also hydrolysis is required for the transport. This model would imply that the CL is natively always in the cavity for the transport cycle and

that the structure of BSEP_glib would therefore not represent a state of bile salt transport. BSEPeqATP agrees with this model by showing densities for the CL even in absence of bile salts, which is the closest model to BSEP in apo state we have. BSEPeqATP_closed disagrees with this model unless we assume that there exists a inactivated state of BSEP in which the CL faces the cytosol. In addition we have to keep in mind, that in 3D classification of BSEPeqATP and BSEPeqATP_CL we find minor classes describing a closed conformation, which does not provide space for the CL. In principle this closed state could represent baseline ATPase activity of BSEP in a locked state with ATP binding inducing closure of the cytosolic cavity. A second model for bile salt transport implies a complicated re-orientation of the CL. We assume that in apo state the CL sits in the cytosol. A bile salt molecule binds to the CL and thereby induces a reorientation into the cavity. From there bile salts are exported upon ATP binding and hydrolysis. This model would assume that the glibenclamide bound state represents the apo state. BSEPeqATP_closed could be explained either as BSEP having bound ATP before bile salt binding to the CL or it could be seen as an expansion of this model. Hereby bile salts interact with the CL and translocate to the cavity. Here bile salt is released and the CL moves back to the cytosol. Now the closing of helix bundles A and B upon ATP binding leads to the final export. In this context BSEPeqATP_closed describes the state after bile salt export, unable to return to the inward open conformation due to the lack of ATP hydrolyzing capability. This model seems nearly too complex, but might be the reason for the extremely low transport rate of BSEP of less than one molecule per transporter and minute, estimated by in-vitro measurements. This model allows further assumptions regarding bile salt transport through hepatocytes. In fish and bird the liver bile acid binding protein (L-BABP) is supposed to shuttle bile salts across the cytosol ([172]). L-BABP is not conserved in mammals, but the related liver fatty acid-binding protein (FABPL) can potentially fill in. The involvement of FABPL in transport is in question, as its deletion has no effect at normal bile salt levels. Still the CL of BSEP might be involved in binding FABPL and releasing shuttled bile salt. But we have to state that this model is in disagreement with the map of BSEPeqATP, where the CL sits in the cavity in absence of bile salts. The third model is very simple and assumes the direct access of bile salt to the cavity. ATP binding then induces closure and export of bile salts. In this model glibenclamide would block BSEP in an inward open state. The CL has no function in this model apart of a potential inactivation of BSEP by blocking the cytosolic cavity. This model seems quite unlikely, as glibenclamide makes contact to most residues interacting with the CL. Furthermore this model can not explain the high substrate specificity of BSEP compared to Pgp. Substrate densities of BSEPeqATP_CL clash with this model as well,

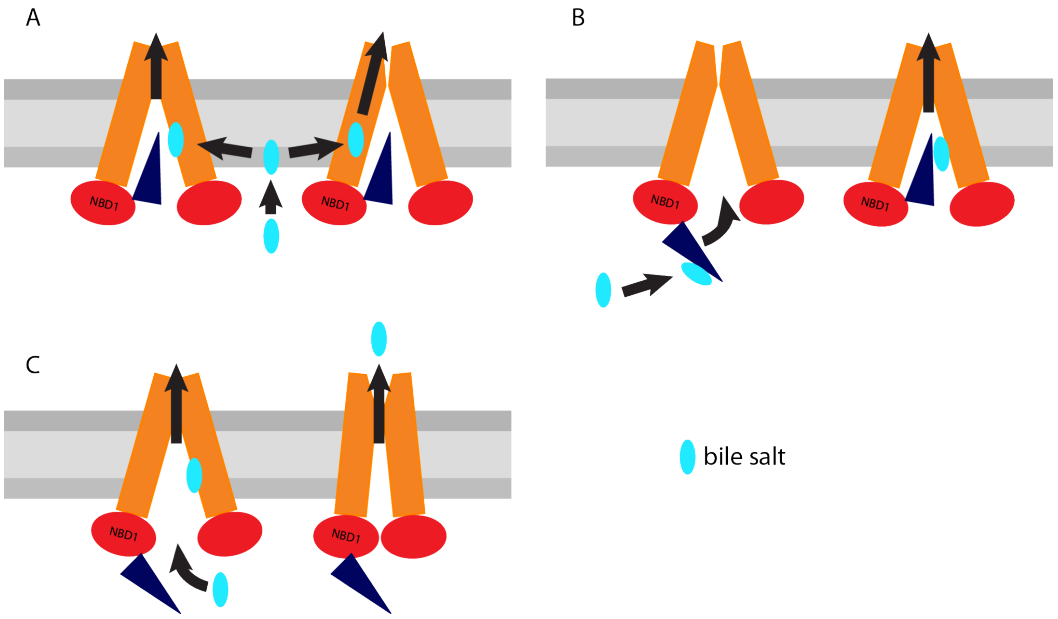


Figure 26: Three models for bile salt transport. The models are reduced to bile salt binding. ATP binding to NBDs is not indicated explicitly. **(A)** Bile salt enters the inner leaflet of the canalicular membrane. From there bile salts are bound by BSEP and translocate to the extracellular side, either along the BSEP-membrane interface or through a cavity build by hydrolysis of ATP. The CL blocks access from the cytosolic side and interacts with bile salt. **(B)** In the apo state the CL faces the cytosol. Upon bile salt binding the CL translocates into the cytosolic cavity. ATP binding and hydrolysis leads to final bile salt export. **(C)** Bile salts enter the cytosolic cavity and are transported to the extracellular side upon ATP binding. The CL is not involved in the transportation, but might still act as a regulator, blocking access to the cytosolic cavity.

because in this state taurocholate is present in BSEP though the CL blocks cytosolic access.
The role of the CL in ABC-transport is unknown so far. In structures of monomeric ABC transporters the CL remains mostly unstructured and a function in transport has not been discussed to our knowledge. Intriguingly, in the case of BSEP mutations placed in the CL are known to trigger PFIC. Therefore we have to assume a functional role for this domain like binding and/or transport of cytosolic bile salts. In summary a model including bile salt entry to BSEP though the inner leaflet or mediated by the CL are much in favor, despite conflicts mentioned previously. Further experiments have to provide more information to come up with more precise transport models.

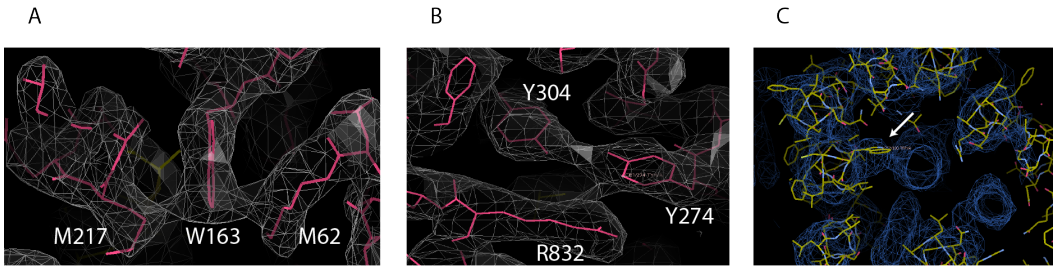


Figure 27: Panel A and B show interactions seen in BSEP_glib, whereas panel C shows an interaction seen in BSEPeqATP_CL. **(A)** M62, W163, and M217 connect helix1, 2, and 3 of helix bundle A. Mutation of these two methionine provokes PFIC. **(B)** PFIC relevant R832 interacts with Y274 and Y304. These three residues are placed in helix bundle B. Y304 might couple interactions of R303 with NBDs to Y274 and R832. **(C)** W330 (white arrow) interacts with the helical part of the CL. Mutating W330 to an arginine leads to PFIC.

### 3.3.4 PFIC and BRIC Related Mutations

Multiple mutations BSEP have been reported to trigger PFIC or BRIC. Mutations affecting gene splicing and nonsense mutations are not to be explained by our structure. Neither are silent mutations, which can be involved in drug induced cholestasis. Table 2 shows a list of missense mutations , sorted according to our models. Least interesting are mutations to a proline, like A390P or Q869P. In this case we can assume that these prolines disrupt the secondary structure they're part of. We will not analyze them in more detail. Other mutations exchange an amino acid by another one with adverse properties: This can affect folding or stability of the transporter. Examples for this type of mutations are G982R, T1029K and I182K. Of most interest are mutations affecting residues showing some interactions, either with a ligand or with other domains. These residues might be part of the transport cycle or key points in stabilizing important domains. Due to the relative low resolution of our maps we pinpoint only some rather clear cases as examples, indicating a potential interaction.
Our model build into BSEP_glib shows a clear interaction of both methionine M217 and M62 with tryptophan W163. These interactions connect helix 1, 2, and 3 of helix bundle A. Arginine 832 is associated with PFIC disease. Here BSEP_glib shows an interaction with tyrosine Y304 and Y274. Especially Y304 is interesting, as preceding arginine R303 is as well associated with PFIC and can make a potential interaction with NBD domains upon an ATP-induced conformational change. Glycine 188 on the other hand sits in the

loop between helix 2 and 3. It forms a cis peptide bond end enables thereby following tryptophan W189 to interact with methionine M185 at the end of helix 2. This leads to a very short loop connecting these two helices. Mutation of G188 would therefore interfere with the formation of this loop and could thereby distort the cytosolic fraction of helix 2 and 3. Tryptophan 330 could be shown to interact with the CL in BSEPeqATP_CL. This is a strong indication for an involvement of the CL in the transport cycle. Involvement of W330 mutations in PFIC supports the idea of CL interactions in ligand transport. R689 sits in the CL of BSEP and correlates with PFIC disease. Based on our BSEPeqATP_CL map this residue is potentially interacting with E825. Intriguingly both residues are conserved between BSEP and ABCB1.

### 3.3.5 Potential Further Experiments

So far no final model for the BSEP transport cycle can be concluded. More structural data as well as biochemical experiments are needed to rule out wrong transport models. An apo structure of BSEP in absence of ATP, taurocholate and glibenclamide could answer the question, whether the CL is in the cytosol in absence of any ligands. A better structure of $BSEP_{EQ}$ with ATP, but without taurocholate and a structure of BSEP with taurocholate, but without ATP would help us to match conformational features with the ligand triggering them. On the biochemical side mutations of some potential key residues from the CL should be tested in a transport assay. Especially L706 interacting with W330, K700 interacting with E723 sitting in the coil region of the CL, and L712 interacting with F83 in the turn between CL helix and coil would be interesting. Furthermore all residues having a potential interaction with PFIC/BRIC relevant residues would be exciting. To assess a potential conformational change of the CL, circular dichroism spectroscopy could be used to monitor reactions of the CL on taurocholate. To get more insight in the glycosylation of BSEP, all 16 N to Q knock out combinations of N109, N116, N122, and N125 should be tested. In addition point mutations at T124 and T127 could be used to prevent glycosylation independent side effects.

## 3.4 Conclusion

For BSEP the goal was to obtain first structural data. We were able to generate four maps and build three models. So far the mechanism of transport is still elusive, as no model can explain all maps we obtained. Nevertheless we could come up with three potential transport models. Two of models give a potential explanation for the high substrate specificity of BSEP compared to ABCB1, by using the transport over the inner membrane leaflet or binding to

| TMD/loop | BRIC type 2 | PFIC type 2 |
|---|---|---|
| Inside | | M1V, G19R |
| TMD 1 | | L50S, M62K, C68Y |
| Outside | | C107R, I112T, W114R |
| TMD 2 | E135K, E137K, E186G | Y157C, A167T, A167V, I182K, M183T, M183V |
| Inside | | G188W |
| TMD3 | L198P | M217R, R223C, S226L |
| Outside | | G238V |
| TMD 4 | | T242I, A257G, V284L |
| Inside | E297G | E297G |
| TMD 5 | | R303G, R303K, Q312H, R313S, G327E, W330R, C336S, W342G |
| Outside | | |
| TMD 6 | G374S, A390P | A382G, R387H, A390P |
| NBD1 | A390P, R432T, V444A, I498T, A570T, T586I, G648V, T655I | G410D, L413W, I420T, D440E, G455E, K461E, T463I, Q466K, R470Q, Y472C, V481E, D482G, R487H, R487P, N490D, I498T, G499E, I512T, N515T, R517H, F540L, I541L, I541T, F548Y, D549V, G556R, G562D, A570T, L581F, A588V, S593R, I627T, E636G |
| CL | | R698C, S699P, E709K |
| TMD 7 | | G758R, G766R |
| Outside | | |
| TMD 8 | | Y818F, R832C, R832H |
| Inside | | |
| TMD 9 | | T859R, A865V, Q869P, G877R |
| Outside | | S901R |
| TMD 10 | T923P, A926P | |
| Inside | R948C | R948C |
| TMD 11 | | N979D, G982R, G1004D |
| Outside | G1004D | |
| TMD 12 | R1050C | T1029K, G1032R, A1044P |
| NBD2 | G1116R, R1128H, L1197G, R1231Q | L1055P, C1083Y, A1110E, S1114R, G1116E, G1116F, G1116R, S1120N, R1128C, S1144R, R1153C, R1153H, S1154P, N1173D, T1210P, N1211D, V1212F, R1231Q, R1231W, L1242I, D1243G, R1268Q, A1283V, G1292V, G1298R |

Table 2: Missense mutations associated with benign recurrent intrahepatic cholestasis and progressive familial intrahepatic cholestasis. Some mutations are associated with both diseases. Table is adapted from ([173]).

the connecting loop as additional selectivity filter. In regard of glycosylation we could show that BSEP is at least glycosylated at N109 and N116. While we cannot rule out an unlikely glycosylation of N122, N125 could be shown to be involved in an interaction with helix 1 instead. As previous experiments indicated a strong impact of mutations at N125, we can assume an involvement of N125 in stabilization or functional rearrangement during the transport cycle. For the inhibitor glibenclamide we describe the binding site and show interactions of the connecting loop with the very same residues in absence of inhibitor. Very important are structural explanations for mutations leading to a disease state. This will help to better interpret future biochemical and genetic data and confirms our model. Some mutations connected with BSEP related intrahepatic cholestasis were addressed. As many questions remain unanswered, further experiments will be needed to find the correct transport model.

## 3.5 Considerations for Pgp Based on BSEP Results

Pgp and BSEP share a high sequence identity. Therefore a similar overall structure was assumed and finally confirmed. Sequence alignments show, that the CL of Pgp is shorter than in BSEP and most CL residues placed in the cavity in BSEP are missing in Pgp. Therefore we have to assume that in Pgp we cannot find the CL facing the cavity. Nevertheless CL residue R698 in BSEP shown to be sensitive to mutation and its interaction partner E825 are conserved in Pgp as R666 and E782. Q869, a second potential interaction partner of R698 is not conserved in Pgp, but all surrounding amino acids are. Maybe interaction is rather with the glycine backbone of G870. In regard of the drastic effect of an R698C mutation in BSEP, an experiment in Pgp with mutations in corresponding residues could give further insight to Pgp based transport.
Pgp and BSEP show both a wide spread of the two helix bundles in the inward open conformation. In case of an amphiphilic molecule a like taurocholate, transport along the protein-membrane interface appears reasonable. For Pgp ligands on the other hand we assume a transport path through the cavity. As the CL of Pgp does not extend into the cavity and as transported molecules do not show detergent characteristics, this transport model is still preferred. Still we have to consider a possible side entry of certain ligands to the cavity. This mode has been proposed before ([21]).

# 4 Sodium Calcium Exchanger (NCX)

This section is based on a unpublished manuscript jointly written by Mark Hilge and Raphael Küng.

All steps of this work were performed by Mark Hilge and Raphael Küng equally, with exception of data processing and the transport assay. Data processing was mostly done by Mark Hilge and the transport assay was performed by Raphael Küng.

**Contents**



## 4.1 Abstract


The plasma membrane $Na^+/Ca^{2+}$ exchanger (NCX) removes bulk amounts of $Ca^{2+}$ from the cytosol by expelling one $Ca^{2+}$ ion for the uptake of three $Na^+$ ions. Here, we report the crystal structures describing two distinct substrate-free states of a NCX homolog from *Thermotoga maritima* (NCX_Tm) in the outward-facing conformation. While one of the forms displays entirely empty ion binding sites, the other shows the presence of a water molecule, restricting and rigidifying the ion binding sites. Comparison with the $Na^+$-bound form of a NCX homolog from *Methanococcus* suggests that re-orientation of the first part of helix M7 is sufficient to form and seal ion access and exit pathways as well as to induce the transition from the outward- to the inward-facing conformation.


## 4.2 Introduction

$Ca^{2+}$ is an ambivalent signal that is both essential and potentially dangerous for cell life [174]. The accurate control of the spatio-temporal homeostasis of

$Ca^{2+}$ is achieved by the concerted interplay of $Ca^{2+}$ channels, $Ca^{2+}$ pumps, and $Ca^{2+}$ exchangers, located in the plasma membrane, the inner mitochondrial membrane, and the membrane of the endoplasmic reticulum [175]; [176]. As a high-capacity $Ca^{2+}$ export system the $Na^+/Ca^{2+}$ exchanger (NCX) enables muscle relaxation in the heart [177]; [178]; [179] and guarantees rapid $Ca^{2+}$ fluxes, important in signaling pathways in excitable cells [180]; [181]. Making use of the $Na^+$ gradient established by the $Na^+/K^+$ ATPase NCX expels one $Ca^{2+}$ ion for the uptake of three $Na^+$ ions [182]; [183]. In animals $Na^+/Ca^{2+}$ exchange is regulated by either $Ca^{2+}$ binding to two $Ca^{2+}$ binding domains present in the intracellular exchanger loop [184]; [185]; [186] or by an interaction of $PIP_2$ [187]; [188] with a third domain referred to as catenin-like domain. In contrast, the $K^+$-dependent NCX (NCKX) and the NCX homologs in plants and lower organisms lack these regulatory domains. Together they form the cation/$Ca^{2+}$ exchanger superfamily of $Na^+/Ca^{2+}$ and $H^+/Ca^{2+}$ exchangers that was divided into five subfamilies, dubbed NCX, NCKX, YRBG, CAX, and CCX [189]. This classification is based on the existence of two homologous, conserved regions of approximately 40 residues designated as α-1 and α-2 repeats [190]; [191]. The repeats comprise transmembrane helices M2 and M3 in the first and M7 and M8 in the second half of the cation/$Ca^{2+}$ exchangers. With the exception of those for glycine and proline, mutations of conserved residues in the α-repeats of NCX and NCKX almost exclusively resulted in loss of exchange activity [190]; [192]. Recently, the structure of a NCX homolog from *Methanococcus jannaschii* (NCX_Mj) was determined at exceptionally high resolution [193]. Intriguingly, the NCX_Mj structure was initially interpreted as a state simultaneously binding one $Ca^{2+}$ and three $Na^+$ ions, thus contradicting the mutually-exclusive mode suggested by many transport experiments [194]; [177]. Subsequent analyses using molecular dynamics indicated that the electron density modeled by a $Ca^{2+}$ ion would better accommodate a $Na^+$ ion and the site located opposite to it, appears to be more compatible with a binding site for a water molecule [195]. Furthermore, from the examination of the ion binding sites it is evident that the ion-coordinating residues constitute a large part of the highly mutation-sensitive amino acids in the α-repeat regions while the remaining conserved residues are probably required to maintain the binding sites. The NCX_Mj structure also revealed the symmetric arrangement of transmembrane helices M1-M5 with respect to helices M6-M10, thus corroborating the hypothesis that cation/$Ca^{2+}$ exchangers originate from an ancient gene duplication event [191]. To obtain a detailed understanding of the transport mechanism of cation/$Ca^{2+}$ exchangers, structural information of as many key intermediate states as possible is essential. Presently, there is one structure of a $Na^+/Ca^{2+}$ exchanger (NCX_Mj) in an outward-facing conformation and three structures, Vcx1 [196], CAX_Af [197], and YfkE [198],

representing $H^+/Ca^{2+}$ exchangers in the inward-facing conformation. Here, we report two new conformational states of the $Na^+/Ca^{2+}$ exchanger from *Thermotoga maritima* (NCX_Tm), constituting the first substrate-free structures of a cation/$Ca^{2+}$ exchanger. Together with the structures of the other exchangers, we assigned the NCX_Tm structures to a specific state in the transport cycle and propose a model for a simple alternate access mechanism, adjusted to cation/$Ca^{2+}$ exchangers.

## 4.3 Results

### 4.3.1 Functional characterization of NCX_Tm

In a GFP-fusion protein screen [199] with about thirty putative cation/$Ca^{2+}$ exchangers from diverse sources NCX_Tm displayed suitable properties for structural studies. To determine its ion selectivity we reconstituted purified NCX_Tm into lipid vesicles. These proteoliposomes were loaded with a 25mM HEPES, pH 6.8 buffer, containing 200mM XCl (X = $Na^+$, $Li^+$, $K^+$, or $NMDG^+$). $Ca^{2+}$ import was initiated by diluting proteoliposomes into external buffer, consisting of 25mM HEPES, pH 6.8, 200mM NMDG-Cl, and 250µM $CaCl_2$. To test for $H^+/Ca^{2+}$ exchange the pH of the external buffer was adjusted to 7.6 and 8.2, respectively. $Ca^{2+}$ accumulation within the vesicles was monitored by measuring the time-dependent increase in fluorescence as a result of $Ca^{2+}$ binding to the dye Fluo-3. As an increase in fluorescence could be detected even in the absence of an ion gradient, all measurements were corrected for this background fluorescence. The highest rate of $Ca^{2+}$ influx was observed upon application of an outwardly directed $Na^+$ gradient, while no transport activity could be detected in the presence of a $H^+$ gradient (Figure 28a and b). Tests with $Li^+$ and $K^+$ as counter ions displayed slower and approximately four-fold reduced $Ca^{2+}$ uptake compared to assays with $Na^+$. The presence of an additional, inwardly directed $K^+$ gradient showed no effect on $Ca^{2+}$ transport (Figure 28b). In summary, the transport assay data are consistent with the properties of a $Na^+/Ca^{2+}$ exchanger. To thermodynamically characterize $Ca^{2+}$ binding to NCX_Tm, we employed isothermal titration calorimetry (ITC). Fitting of the integrated heat pulses suggests that NCX_Tm binds one $Ca^{2+}$ ion with an affinity of 84 ± 5µM (Figure 28c).

### 4.3.2 NCX_Tm structures

To get deeper insight into the $Na^+/Ca^{2+}$ exchange mechanism we conducted vapor diffusion and liquid cubic phase crystallization experiments with NCX_Tm. Our vapor diffusion efforts yielded two crystal forms which belong to space group C2 and C2221, respectively. Initially, the structure of the C2

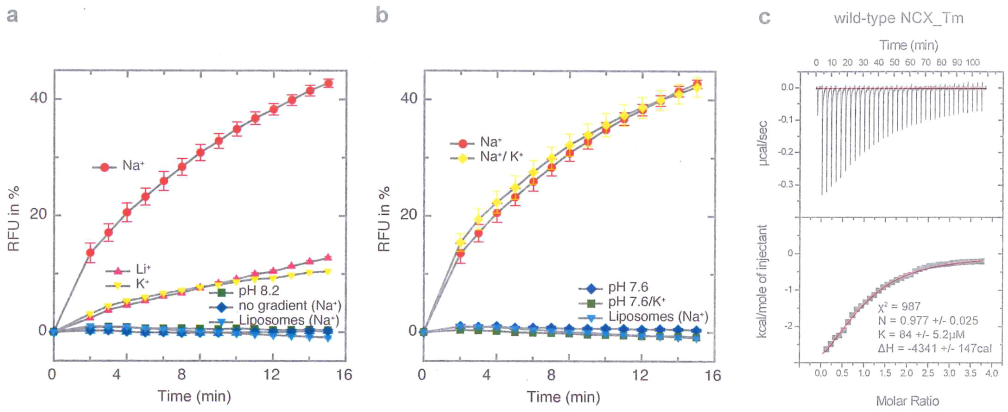


Figure 28: $Ca^{2+}$ transport and binding. **(a)** Counter ion selectivity of NCX_Tm-mediated $Ca^{2+}$ uptake into proteoliposomes by monitoring the increase in fluorescence in response to $Ca^{2+}$ binding to the dye Fluo-3. Transport assays were performed for $Na^+$, $Li^+$, $K^+$, and $H^+$. To explore potential $H^+$-coupled $Ca^{2+}$ transport, pH gradients were applied employing a luminal pH of 6.8 against an extraliposomal pH of 7.6 or 8.2. As controls transport assays were conducted in the absence of a $Na^+$ gradient and in the presence of equimolar concentrations of NMDG-Cl. The latter measurements were subtracted from all other experiments to account for $Ca^{2+}$ contaminations in the buffers and potential $Ca^{2+}$ leakage. **(b)** An additional inwardly directed $K^+$ gradient was applied to evaluate the possibility of a $K^+$-dependent NCX. All experimental details concerning the transport assays can be found in Supplementary Table 3. **(c)** Thermodynamic characterization of NCX_Tm using isothermal titration calorimetry (ITC). The top graph displays the recorded heat pulses, observed upon injection of 1µl of 3mM $Ca^{2+}$ containing buffer, while the data points in the bottom graph are the result of the integration of the heat pulses. Fitting of the data points yields the binding isotherm, the stoichiometry, and the binding constant.

crystal form was determined by molecular replacement using the coordinates of NCX_Mj [193]. The structure of the C2221 crystal form was obtained using the C2 crystal structure as search model. The C2 and C2221 structures were refined using data to 3.5 and 3.55Å, respectively. In both crystal forms, NCX_Tm crystallizes as a dimer with both protomers in the same orientation, adopting an outward-facing conformation (Figure 29a). This arrangement was also found in four additional crystal forms, we investigated. The overall differences between the protomers are relatively subtle. However, the two crystal

forms display marked differences in their ion binding sites. In particular, in the C2 form no electron density was observed for multiple side chains, which are strictly conserved among NCX and were shown to be crucial for ion coordination [193]. Furthermore, there is no indication for substrate binding in the electron density at positions where ions bind in the NCX_Mj structure (Figure 29b). Taken together, the structure of the C2 crystal form appears to be compatible with a substrate-free state. In comparison, with the exception of Glu215 the side chains of the ion-coordinating residues in the structure of the C2221 crystal form are visible in the electron density. At the position similar to the binding site previously referred to as $Na^+$mid a density peak above $1\sigma$ in the 2Fo-Fc and above $3\sigma$ in the Fo-Fc map is observed (Figure 29c). However, there is no electron density indicative of the coordination of a $Ca^{2+}$ ion or a $Na^+$ ion at a location comparable to $Na^+$int or $Na^+$ext. In contrast to the C2 crystal form, the binding sites of the C2221 form are considerably more restricted. For instance, the distance between the Cα atoms of Pro50 and Pro214, strictly conserved residues preceding the $Ca^{2+}$ coordinating glutamates in NCX and NCKX, is 2Å shorter and comparable with the distance found in NCX_Mj. This suggests that the initial binding of a water molecule brings helices M2 and M7 closer together at the ion binding sites.

### 4.3.3 Structural comparison with NCX_Mj

Superposition of the structure of NCX_Mj onto the structure of the C2 crystal form shows an rmsd of 1.58Å on 235 Cα positions. Aside the deviations at the N- and C-termini and regions before and after the central disordered loop (Figure 29a), the most prominent difference is observed for the position of helix M7a that is rotated by approximately 43° in NCX_Mj with respect to NCX_Tm. As a result helix M7 is bent in NCX_Mj, but kinked in NCX_Tm (Figure 30a). Examination of the surroundings of helix M7a in NCX_Tm and NCX_Mj reveals a relative paucity of hydrogen bonds and van der Waals interactions with the remainder of the protein. A similar, albeit less pronounced re-orientation is found for the symmetry-related helix M2a in $H^+/Ca^{2+}$ exchangers in the inward-facing conformation, between the $Ca^{2+}$ bound structure of Vcx1 [196] and the fully protonated form of CAX_Af [197] (Figure 32). Helices M1 and M6 are somewhat detached from the helical core that comprises the environment for the ion binding sites. While they superimpose well for a large part of their length deviations of 2.5 and 1.5Å are observed at the end of helix M6 and the beginning of helix M1, probably as a consequence of the distinct positions of helix M7a in NCX_Tm and NCX_Mj (Figure 30b). Close inspection of generally conserved residues in helices M2 and M7 that are not directly involved in ion coordination, reveals predominately hydrophobic

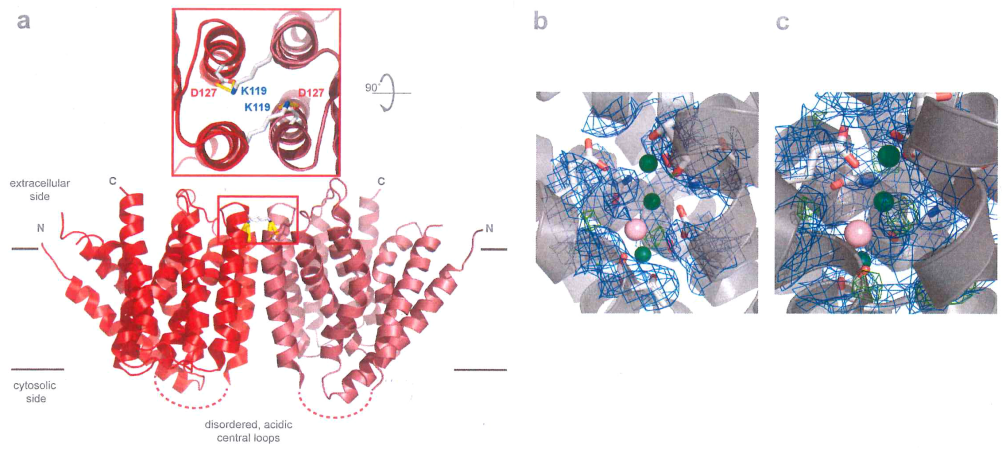


Figure 29: Overall structure and ion binding sites of NCX_Tm in the outward-facing conformation. **(a)** Dimeric structure of NCX_Tm with protomer A shown in red and protomer B in rose. The highly acidic central loop is disordered and indicated by red dashes. The salt-bridges between Lys119 and Asp127 are highlighted in the blow-up. **(b)** Empty ion binding sites of the C2 crystal form. Positions, at which ions bind in the NCX_Mj structure, are indicated by dashed circles. **(c)** Occupied binding site opposite to the empty $Na^+_{mid}$ site in the C2221 crystal form. The $2F_o$-$F_c$ and $F_o$-$F_c$ maps are contoured at 1σand 3σ, respectively. All structural figures were generated in PyMOL

interactions with non-conserved residues in helix M6. In NCX_Tm, Leu49, Pro50, and Val53, located in helix M2 at the center of the ion binding sites, form extensive van der Waals interactions mostly with Ile174 and Trp178 in helix M6 (Figure 30c). In contrast, the corresponding residues in helix M7, Leu213, Pro214, and Val217, maintain a comparably reduced number of hydrophobic interactions. In NCX_Mj, with the ion binding sites occupied by three $Na^+$ ions, the situation is reversed, i.e. the corresponding residues in helix M7, but not those in M2, maintain numerous van der Waals contacts with residues in helix M6.

### 4.3.4 Ion pathway analysis of NCX_Tm and related cation/$Ca^{2+}$ exchanger structures

To support an assignment of the NCX_Tm structures to specific states in the transport cycle of cation/$Ca^{2+}$ exchangers we performed ion pathway analyses using the program MOLE 2.0 [200]. As a starting point for the calculations, we chose Glu51 and Glu215 at the center of the ion binding sites. For both

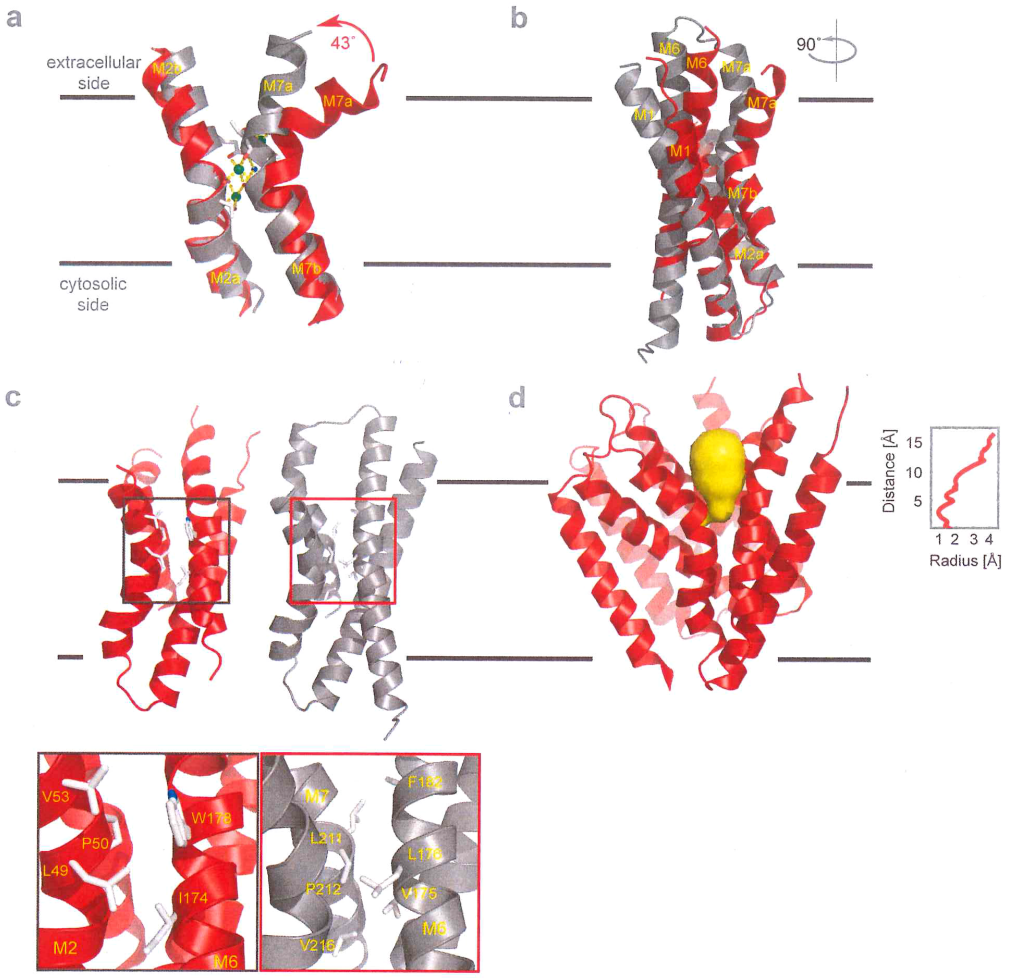


Figure 30: Conformational changes in bacterial $Na^+/Ca^{2+}$ exchangers in the outward-facing conformation upon $Na^+$ binding. **(a)** Re-orientation of helix M7a between NCX_Tm (red) and NCX_Mj (grey) in response to $Na^+$ binding. **(b)** Impact of $Na^+$ binding on helices M6 and M1 as well as the hydrophobic interactions **(c)** with helix M6 for NCX_Tm (red) and NCX_Mj (grey). **(d)** Ion pathway analysis of the NCX_Tm structures using the program MOLE 2.0 [200]. The tunnel detected in protomer A of the C2 crystal form is colored yellow. The graph on the right shows the tunnel radius as a function of the distance to Glu51, which was chosen as a starting point for the calculations.

NCX_Tm structures, the calculations revealed an approximately 17Å long pathway that gradually widens towards the surface of the exchanger (Fig-

ure 30d). Strikingly, application of the same parameters as used in the calculations for the NCX_Tm structures, yields, in disagreement with previous suggestions [193], no ion pathways for NCX_Mj. To extend the ion pathway analysis to the entire transport cycle we also performed the corresponding calculations with identical parameter settings to the available, superimposed $H^+/Ca^{2+}$ exchanger structures in the inward-facing conformation (Figure 33). For each protomer at least one ion pathway could be detected. While the protomers of CAX_Af and YfkE display similar pathway diameters, substantially different profiles were found for the $Ca^{2+}$ bound protomers of Vcx1.

### 4.3.5 Dimer interface and 2nd $Ca^{2+}$ binding site

In contrast to the dimers found in the asymmetric units of the Vcx1 and CAX_Af structures, there are several lines of evidence that protomers A and B form a physiological dimer in NCX_Tm. First, both protomers display the same orientation in the NCX_Tm crystal structures (Figure 29a). Thereby, protomers A and B interact via an interface of 1001$Å^{-2}$. Its main feature is Lys119, which forms a salt-bridge with Asp127 in the other protomer. Second, analyses using multi-angle light scattering (SEC-MALS) suggest a tetramer for wild-type NCX_Tm (Figure 31b), but predominantly only a dimer for the K119A and K119E mutants (Supplementary Fig. 3). The additional dimerization may be explained by the interaction of the N- and C-termini of one dimer with the corresponding termini of another dimer, resulting in an arrangement found in the C2 and C2221 crystal forms. Aside its importance in dimer formation, intriguingly the NZ group of Lys119 coincides with a second $Ca^{2+}$ binding site in NCX1 and NCKX2. Conserved mutations of residues Asp121 and Asp127 that coordinate the second $Ca^{2+}$ ion, resulted in non-functional canine NCX1 [190] and human NCKX2 [192]. In the case of NCX_Mj a corresponding second $Ca^{2+}$ binding site is found on the extracellular side in the loop connecting helices M4 and M5, whereas in the $H^+/Ca^{2+}$ exchangers, an analogous second $Ca^{2+}$ binding site is found on the cytosolic side between helices 9 and 10 in the Vcx1 and CAX_Af structures, but not in the YfkE structure, determined at pH 4. To assess the potential relevance of Lys119 in the exchange mechanism as an alternative to the second $Ca^{2+}$ binding site in other cation/$Ca^{2+}$ exchangers, we analyzed the K119A and K119E mutants by means of the proteoliposomal transport assay, previously used for wild-type NCX_Tm. As no differences in activity could be observed in the transport assays for the mutants compared to wild-type NCX_Tm (Figure 31c), the function of the second $Ca^{2+}$ binding site remains enigmatic.

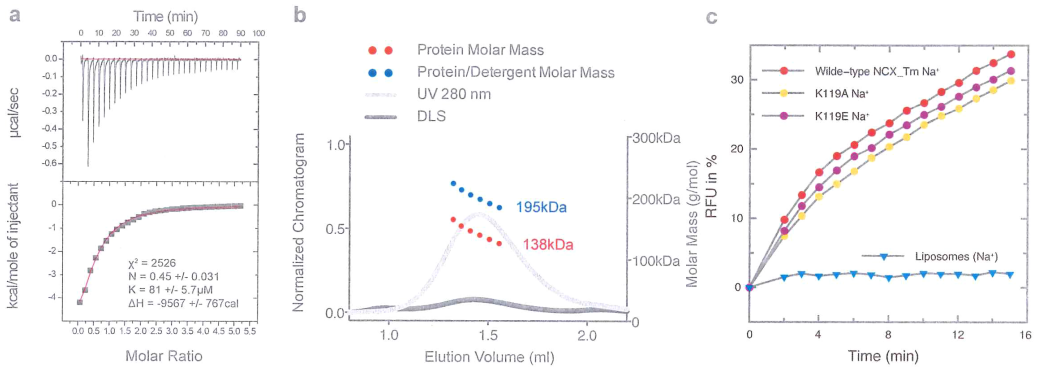


Figure 31: Characterization of the Lys119 mutants in the dimer interface. **(a)** Thermodynamic characterization of the K119A mutant by ITC. The top graph displays the recorded heat pulses, while the data points in the bottom graph are the result of the integration of the heat pulses. Fitting of the data points yields the binding isotherm, the stoichiometry, and the binding constant. **(b)** SEC-MALS analysis performed at 6°C. Results of the SEC-MALS experiments of the Lys119 mutants can be found in Supplementary Figure 34. **(c)** $Ca^{2+}$ transport properties of the K119A and K119E mutants with respect to wild-type NCX_Tm.

## 4.4 Discussion

Bioenergetically, protons are the most common coupling ions in bacterial transport. However, some bacteria utilize, similarly to animals, a $Na^+$ gradient for coupled transport [201]. With the help of transport assays based on proteoliposomes we demonstrate that NCX_Tm, like NCX_Mj, is a $Na^+/Ca^{2+}$ exchanger. In contrast, the structurally characterized Vcx1, CAX_Af, and YfkE were shown to be $H^+/Ca^{2+}$ exchangers. This raises the question whether it would be possible to predict the nature of the counter ion from the primary sequence. Comparison of residues involved in ion coordination in the available $Na^+/Ca^{2+}$ exchanger structures reveals that Thr50, Ser51, Thr209, and Ser210 are generally conserved in the large body of intensively studied mammalian NCX and NCKX, but are absent in the $H^+/Ca^{2+}$ exchanger structures. These four residues crucially coordinate the $Na^+{}_{int}$ and $Na^+{}_{ext}$ ions via the free electron pairs of their hydroxyl groups. The importance of these residues in $Na^+$ binding and their conservation in the YRBG subfamily of cation/$Ca^{2+}$ exchangers, suggests that its members can probably be regarded as bacterial $Na^+/Ca^{2+}$ exchangers. In comparison a high percentage of $H^+/Ca^{2+}$ exchangers show conservation of the GNxxE motif in the α-repeats. In the $Ca^{2+}$ bound Vcx1 structure the conserved Gly102, Asn103, Gly298, and Asn299

form hydrogen bonds to three water molecules that assist the coordination of the $Ca^{2+}$ ion. In contrast, the distantly related CAX_Af represents a minority of $H^+/Ca^{2+}$ exchangers and possesses instead of the conserved glycine and asparagine residues two additional acidic residues, Asp82 and Glu25, in the ion binding sites. Hence, the presence of either the GNxxE motif or two additional acidic residues in the center of helices M2 and M7 is indicative of a $H^+/Ca^{2+}$ exchanger. To get a detailed overview of the entire transport cycle of cation/$Ca^{2+}$ exchangers we made an attempt to assign each of the presently available structures to a specific state in the cycle. Thereby, we predominantly based our assignment on the angle between helices M2 and M7a in the outward- and the angle between helices M2a and M7 in the inward-facing conformation, the presence of a tunnel and the substrates bound to the exchangers. In the C2 crystal form of NCX_Tm disordered side chains of the ion-coordinating residues, the absence of bound $Na^+$ or $Ca^{2+}$ ions, a kinked helix M7 and wide ion binding sites are compatible with a substrate-free conformation (state 1). The C2221 crystal form of NCX_Tm displays an occupied water binding site. In contrast to the entirely empty sites of the C2 crystal form, the water binding appears to bring helices M2 and M7 closer together and causes a rigidification of side chains of the ion-coordinating residues with the exception of the side chain of Glu215 (state 2). Probably upon occupation of the external $Na^+$ binding site Comparison of the substrate-bound form of NCX_Tm with the NCX_Mj structure suggests that the interactions of the strictly conserved Thr211 and Ser212 with the third $Na^+$ ion lead to a re-orientation of helix M7a. This transition is probably facilitated by the relative paucity of interactions of residues in helix M7a with the remainder of NCX_Tm and NCX_Mj. As a consequence, the kinked helix M7, present in NCX_Tm, is converted into a bent helix as found in NCX_Mj. While tunnel analyses of the two states of NCX_Tm reveal very similar profiles for their ion access/exit pathways, no ion pathway could be identified in NCX_Mj, thus suggesting an occluded state (state 3). The re-orientation of helix M7a also appears to alter the interactions of in NCX and NCKX conserved apolar residues with residues in helix M6. Directly located at the ion binding sites, Leu49, Pro50, and Val53 in helix M2 of the substrate-free states of NCX_Tm form numerous hydrophobic interactions with residues in helix M6, which are mostly absent in NCX_Mj. Instead, as a sort of compensation, NCX_Mj maintains van der Waals interactions between Leu211, Pro212, and Val215 in helix M7 with non-conserved apolar residues in helix M6 (Figure 30c). Consequently, the end of helix M6 and the beginning of helix M1 are relocated accordingly (Figure 30b). In analogy to the state-dependent positions of helix M7a in the outward-facing conformations of NCX_Tm and NCX_Mj, comparable orientations are observed for the symmetry-related helix M2a in the inward-facing

conformations of the CAX structures. As helices M2b and M7b are considerably less affected by substrate binding, we superimposed the structures of the outward- onto the inward-facing conformations, using these constant regions of helices M2 and M7 as alignment anchors. This structural alignment reveals that at least the end of helix M7a in NCX_Mj and the beginning of helix M2a in CAX_Af adopt positions similar to the same helices in the oppositely oriented inward- and outward-facing conformations. Hence the re-orientation of helix M7a, accompanied by small adjustments in the position of helix M6 and even smaller changes with respect to helix M1 (Figure 30b), is sufficient to close the extracellular ion pathway(s) in NCX_Mj. However, although protomer A of CAX_Af is fully protonated and its helix M2 maintains a conformation very close to the one of helix M2 in NCX_Tm and NCX_Mj, the exchanger from *Archaeoglobus* does not constitute an occluded state, but rather reflects a state either immediately before or after due to the presence of an ion pathway (state 4). Protomer B of CAX_Af shows the same orientation for helices M2 and M7 as protomer A, however probably as a consequence of the unprotonated state of Glu258 wider ion binding sites. Similarly to the orientation of helix M7 in states 1 and 2 in the outward-facing conformation the structures of $Ca^{2+}$ bound Vcx1 possess a kinked helix M2 (state 5). Finally, the structure of YfkE, obtained from crystals grown at pH 4, probably represents an inactive or locked state as His256 occupies a position normally maintained by the $Ca^{2+}$ coordinating Glu255. The outlined model for transport is depicted in Figure 35. Despite the increasing number of cation/$Ca^{2+}$ exchanger structures shedding more and more light on the mechanism of the transport cycle, several questions, especially those regarding the exact location of the $Ca^{2+}$ binding site and how $Ca^{2+}$ binding can induce the transition from the inward- to the outward-facing conformation, remain. Furthermore, there is presently no explanation for the relatively large differences in the orientation of helices M1 and M6 between the outward- and inward-facing conformations. As there are no conserved residues in these helices varying conformations may also be attributed to differences between $Na^+/Ca^{2+}$ and $H^+/Ca^{2+}$ exchangers. Our study has revealed the first substrate-free structures of a cation/$Ca^{2+}$ exchanger in the outward-facing conformation. Comparison with the previously reported structures of cation/$Ca^{2+}$ exchangers the NCX_Tm structures suggest that re-orientation of helix M7a is basically sufficient to seal the extracellular pathways. In agreement with the high turnover rates reported for mammalian NCX [202]; [177] such a simple mechanism could provide the basis for an alternate access mechanism, generally expected for cation/$Ca^{2+}$ exchangers.

## 4.5 Methods

### 4.5.1 Cloning, screening and expression

To identify cation/$Ca^{2+}$ exchangers suitable for structural studies we cloned 20 genes encoding putative bacterial and mammalian $Na^+/Ca^{2+}$ as well as ten fungal and plant $H^+/Ca^{2+}$ exchangers using a ligation independent cloning (LIC) approach. For efficiency purposes we utilized a modified pGAPZ vector to create C-terminal GFP fusion constructs for expression in Pichia pastoris. Exchanger expression levels were monitored by in-gel fluorescence analysis of 2ml cultures, harvested at different optical densities. In this screen the $Na^+/Ca^{2+}$ exchanger of *Thermotoga maritima* (NCX_Tm) was identified as a promising candidate for structural studies. Solubilization efficiency and detergent compatibility was assessed by fluorescence size-exclusion chromatography [203]; [199]. Best results with respect to stability and monodispersity were obtained with 5-cyclohexyl-1-pentyl-β-D-maltoside (CYMAL-5 ANAGRADE®, Anatrace). For large-scale expressions and the establishment of a purification protocol the C-terminal GFP-tag, fused to full-length NCX_Tm (309 residues, UniProt accession code: Q9WZI3) was replaced by a Strep-II-tag (WSHPQFEK). As a relict of the 5' LIC primer this construct contained four non-coding residues, MLFQ, at the N-terminus.

### 4.5.2 Purification

A pre-culture of 10ml, grown at 30°C in the presence of 1mg of zeocin™(InvivoGen), was used to inocculate 4L of YPD medium (Invitrogen *Pichia pastoris* User Manual). At an OD600 of 8-10 cells were harvested by centrifugation. For crude membrane preparation cell pellets were dissolved in buffer A (50mM Tris, pH 8.0, 10% glycerol) supplemented with 300mM NaCl, 10mM β-mercaptoethanol, 1mM benzamidine, DNAse I, and Complete EDTA-free protease inhibitors (Roche). Cells were broken by performing ten passes through an M-110P Microfluidizer (Microfluidics) applying 20'000 PSI. After removal of the cell debris by centrifugation (11'000g for 30min), crude membranes were harvested by ultracentrifugation at 195'000g for 3h. To remove membrane-associated contaminants the crude membranes were washed in buffer A supplemented with 1M NaCl and 5mM β-mercaptoethanol and were pelleted at 195'000g for another 3h. The washed crude membranes were then solubilized in buffer B (50mM Tris, pH 8.0, 300mM NaCl, 5mM β-mercaptoethanol) supplemented with 20mM n-dodecyl-β-D-maltopyranoside (DDM SOL-GRADE®, Anatrace) for 3h. Subsequently, insoluble parts were removed by centrifugation at 70'000g for 1h and the cleared, solubilized extract was exposed to buffered streptactin beads for 2h using gentle rotation.

The beads were collected in a Biorad Econo column and the flow-through was re-loaded three times to increase the binding efficiency of NCX_Tm. After washing the beads with 13 column volumes of buffer B supplemented with 6mM CYMAL-5, NCX_Tm was eluted with the wash buffer containing 5mM desthiobiotin. For crystallization NCX_Tm was first concentrated to a volume of 500µl, washed twice with 50mM Tris, pH 8, 300mM NaCl and 6mM CYMAL-5, and was finally concentrated to 9-12mg/ml using a 50kDa cut-off filter (Amicon® Ultra-4). To remove potential aggregates the NCX_Tm concentrate was ultracentrifuged at 220'000g for 20min. All purification steps were performed at 4°C.

### 4.5.3 Crystallization

By mixing 100nl of concentrated NCX_Tm with 100nl of reservoir solution using the standard MemStart, MemSys, and MemGold screens (Molecular Dimensions) several initial hits in vapor diffusion crystallization experiments were obtained at 20°C. From the crystal forms we investigated two forms diffracted to approximately 3.5Å resolution. Crystals of form 1 belonged to space group C2 and grew in the presence of 100mM $Na^+$ citrate, pH 4.75-5.5, 200mM $(NH_4)_2SO_4$, and 33-36% PEG 200. These either rod- or plate-like crystals appeared after 30 days and reached their final dimensions of up to 500 × 100 × 10µm within 60 days. Crystals of form 2 belonged to space group C2221 and were obtained with reservoir solution containing 100mM $Na^+$ citrate, pH 5.0, 100mM $Li_2SO_4$, and 10-10.5% PEG 4000. These cat eye-like crystals were generally visible after ten days and grew to full dimensions of 200 x 100 x 20µm within a few days. While crystallization conditions of the C2 crystal form already included a cryoprotectant, freezing of the C2221 crystals required the addition of 30% ethylene glycol. All crystal forms investigated diffracted X-rays anisotropically and substantial efforts to obtain more isotropic diffraction failed.

### 4.5.4 Structure determination

All data sets were collected from frozen crystals at the X06SA beamline at the Swiss Light Source of the Paul Scherrer Institut using a PILATUS 6M detector. The data were indexed and integrated with XDS [204] while merging of the data was carried out with aimless [205] within the CCP4 suite [206]. Anisotropy correction [207] was carried out in Phaser [208] prior to structure determination of the C2 crystal form by molecular replacement (MR). The best MR solution was obtained using the coordinates of the $Na^+/Ca^{2+}$ exchanger from *Methanococcus jannaschii* (pdb code: 3V5U) [193] and was initially re-

fined with phenix.mr_rosetta [209]. The NCX_Tm structure was then further improved in several alternating rounds of model building in COOT and refinement using PHENIX [144] and Buster-TNT [210], employing two-fold NCS restraints, restrained individual B factors and TLS. Despite the anisotropic data the electron density of the C2 form was of high quality and resulted in a model comprising good geometry. The structure of the C2221 crystal form was determined using the C2 structure as a search model, while refinement was carried out analogously to the C2 structure. Rfree was calculated by selecting 10% of the reflection data that were omitted throughout the refinement. The final structures of the C2 and C2221 crystal forms have R/Rfree values of 0.330/0.370 and 0.285/0.331.

### 4.5.5 Reconstitution and transport assay

Liposomes were prepared by mixing chloroform stocks of 1-palmitoyl-2-oleoyl-sn-glycero-3-phosphocholine (POPC), 1-palmitoyl-2-oleoyl-sn-glycero-3-[phospho-rac-(1-glycerol)] (POPG), and 1-palmitoyl-2-oleoyl-sn-glycero-3-phosphoethanolamine (POPE) at a 3:1:1 ratio. Prior to dissolving the lipids in PBS buffer (137mM NaCl, 2.7mM KCl, 10mM $Na_2HPO_4$, 1.8mM $KH_2PO_4$) chloroform was evaporated. For NCX_Tm reconstitution liposomes were sonicated, extruded through a 400nm filter using a mini-extruder for large unilaminar vesicles (Avanti), and destabilized with Triton X-100. Purified NCX_Tm (1mg/ml) was then mixed with the liposomes at a ratio of 1:50. After removal of the detergent with the bio-beads, the proteoliposomes were fractionated and stored at -80°C [211]. To determine the counter-ion specificity of NCX_Tm the PBS buffer of the proteoliposomes was changed to 25mM HEPES, pH 6.8 buffer supplemented with 100µM of the fluorescent dye Fluo-3 (F-1240, Fisher Scientific), 200mM NMDG+ or 200mM of XCl where X is either $Na^+$, $K^+$, or $Li^+$. To load the vesicles, the proteoliposomes were briefly sonicated, subjected to three freeze/thaw cycles, and extruded through a 200nm filter. To remove the fluorescent dye outside the vesicles, proteoliposomes were pelleted by centrifugation at 21'000g for 90min and re-suspended in the buffer used to load the vesicles. This washing step was repeated four times. Finally, the proteoliposomes were aliquoted at a concentration of 100mg/ml. The transport assays were performed in black, flat-bottom 96-well plates using a Synergy H1 fluorescence plate-reader. Thereby, 4µl of proteoliposomes were diluted in 200µl of external buffer (for details see Table 3). The initial three minutes of the experiments were used to determine the baseline. $Ca^{2+}$ uptake into the vesicles was initiated by the addition of 250µM CaCl−2 to the external buffer and the change of fluorescence was monitored during 1h. To equilibrate the $Ca^{2+}$ concentration across the proteoliposomal membrane, calcimycin to a fi-

nal concentration of 100nM was added. This allowed for the normalization of the fluorescence data using the baseline before $CaCl_2$ addition and the signal of the saturated dye after calcimycin addition. To correct for background fluorescence, values obtained with a "zero-gradient" experiment employing a 25mM HEPES, pH 6.8 200mM NMDG inside and outside of the vesicle, were subtracted from each experiment. Measurements were performed in triplicate with the standard errors of the mean indicated by error bars. All buffers used in the transport assays were prepared with $Ca^{2+}$-free water (H2OMB0501, Merck Millipore) and residual $Ca^{2+}$ was chelated by appropriate amounts of EGTA, which were estimated by measuring the fluorescence of the dye fluo-3 in the corresponding buffers.

### 4.5.6 Isothermal titration calorimetry (ITC)

NCX_Tm (wild-type and mutants) samples for ITC measurements were prepared using $Ca^{2+}$-free water and high-quality chemicals to minimize the amount of contaminating $Ca^{2+}$ ions. Protein concentrations were determined using a Nanodrop® spectrophotometer ND-1000 (Isogen Life Science) and were 254µM and 150µM in the case of wild-type NCX_Tm and mutant NCX_K119A, respectively. Metal salts were prepared in the same buffers as the corresponding protein samples. ITC experiments were carried out with an ITC200 (Microcal LLC) device. Following thermal equilibration at 293K, 38 serial injections of 1µl were performed at 500 rpm stirring speed with an injection spacing of 3min. Constructs were measured at least three times to determine the optimal experimental conditions with respect to signal-to-noise ratio and the number of data points. In all cases, experiments were consistent and reproducible. To correct the experimental binding isotherm for background heat effects, we also titrated $CaCl_2$ containing buffer into buffer. Data were analyzed with the "one set of sites" model implemented in the Origin 7.0 software.

### 4.5.7 Multi-angle light scattering (SEC-MALS)

SEC-MALS [212] experiments were performed at 6°C using a 5/150 Superdex S200 column (GE Healthcare) equilibrated in 50mM Tris, pH 8.0, 300mM NaCl, 5mM β-mercaptoethanol and 6mM CYMAL-5, on an Agilent 1260 HPLC system with a Wyatt Heleos 2 8-angle light-scattering detector and a Wyatt Optilab Rex differential refractive index detector. Signal alignment, band-broadening correction and detector normalization were performed according to the manufacturers instructions, using bovine serum albumin monomer (Sigma Aldrich) in the experimental buffer. For the analysis of

purified NCX_Tm or the K119A mutant, 50µl samples were injected. Weight-average molecular weights for protein and detergent components were determined for each point in the chromatogram by global fitting of light-scattering, UV absorbance at 280nm, and differential refractive index data, using the protein conjugate analysis method in the Wyatt Astra 6 package.

## 4.6 Conclusion

Our NCX project provides a first apo conformation. This helps to fill up gaps in the current list of available conformations. In addition our model gives the first structural evidence for a dimerization of a $Na^+/Ca^{2+}$ exchanger. However we have to assume that this is a feature of the *Termotoga maritima* NCX homolog. In a transport assay we shower that NCX_Tm is actually a real $Na^+/Ca^{2+}$ exchanger like NCX_Mj, and not a $H^+/Ca^{2+}$ exchanger as assumed. Sequence alignments could show common features, which might help to predict the counter ion for other NCX homologs. Based on structures available up to date, we propose a very simple model of alternative access. This model is in line with the high exchange rate of NCX. In contrary to alternative models conformational changes of helix 1 and 6 are not considered to be part of the transport cycle.

## 4.7 Supplementary Figures

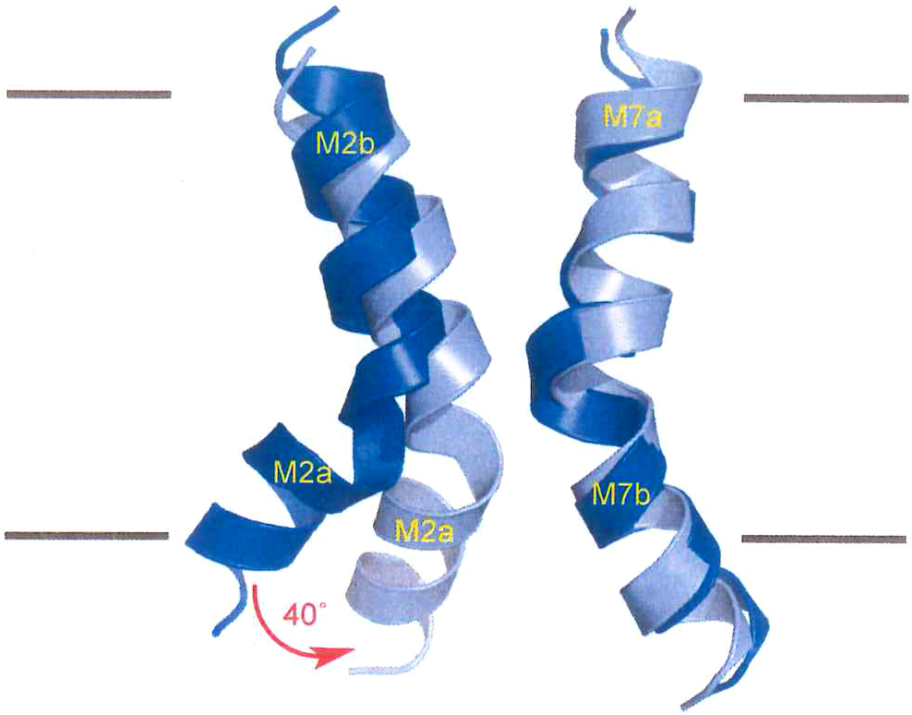


Figure 32: Conformational changes in $H^+/Ca^{2+}$ exchangers in the inward-facing conformation. Superposition of helices M2 and M7 of $Ca^{2+}$ bound Vcx1 (blue) and fully protonated CAX_Af (light blue).

| Measurement | Inside | | Outside | | |
|---|---|---|---|---|---|
| Na | 200mM NaCl | 50mM HEPES pH 6.8 | 200mM NMDG | 50mM HEPES pH 6.8 | |
| Na/K | 200mM NaCl | 50mM HEPES pH 6.8 | 200mM NMDG | 50mM HEPES pH 6.8 | 200mM KCl |
| No gradient (Na) | 200mM NaCl | 50mM HEPES pH 6.8 | 200mM NaCl | 50mM HEPES pH 6.8 | |
| pH 7.6 | 200mM NMDG | 50mM HEPES pH 6.8 | 200mM NMDG | 50mM HEPES pH 7.6 | |
| pH 8.2 | 200mM NMDG | 50mM HEPES pH 6.8 | 200mM NMDG | 50mM HEPES pH 8.2 | |
| No gradient (NMDG) | 200mM NMDG | 50mM HEPES pH 6.8 | 200mM NMDG | 50mM HEPES pH 6.8 | |
| pH 7.6/K | 200mM NMDG | 50mM HEPES pH 6.8 | 200mM NMDG | 50mM HEPES pH 7.6 | 200mM KCl |
| No gradient (NMDG)/K | 200mM NMDG | 50mM HEPES pH 6.8 | 200mM NMDG | 50mM HEPES pH 6.8 | 200mM KCl |
| K gradient | 200mM KCl | 50mM HEPES pH 6.8 | 200mM NMDG | 50mM HEPES pH 6.8 | |
| Li gradient | 200mM LiCl | 50mM HEPES pH 6.8 | 200mM NMDG | 50mM HEPES pH 6.8 | |
| Liposomes | 200mM NaCl | 50mM HEPES pH 6.8 | 200mM NMDG | 50mM HEPES pH 6.8 | |

Table 3: For three minutes the baseline was determined. After the addition of 250µM $CaCl_2$ the change of fluorescence was recorded for 1h. Then 100nM calcimycin was added to equilibrate $[Ca^{2+}]$ over the proteoliposoms. Recorded data were scaled using the baseline before $CaCl_2$ addition and the signal of saturated dye after calcimycin addition. All measurements were done three times. Standard error of the mean (N=3) are given for all measuring points. Buffers for the transport assay were prepared with Ca-free water (Millipore) and residual $Ca^{2+}$ was complexed with 20µM EGTA. Free $[Ca^{2+}]$ was estimated by measuring fluo-3 saturation in the corresponding buffer.

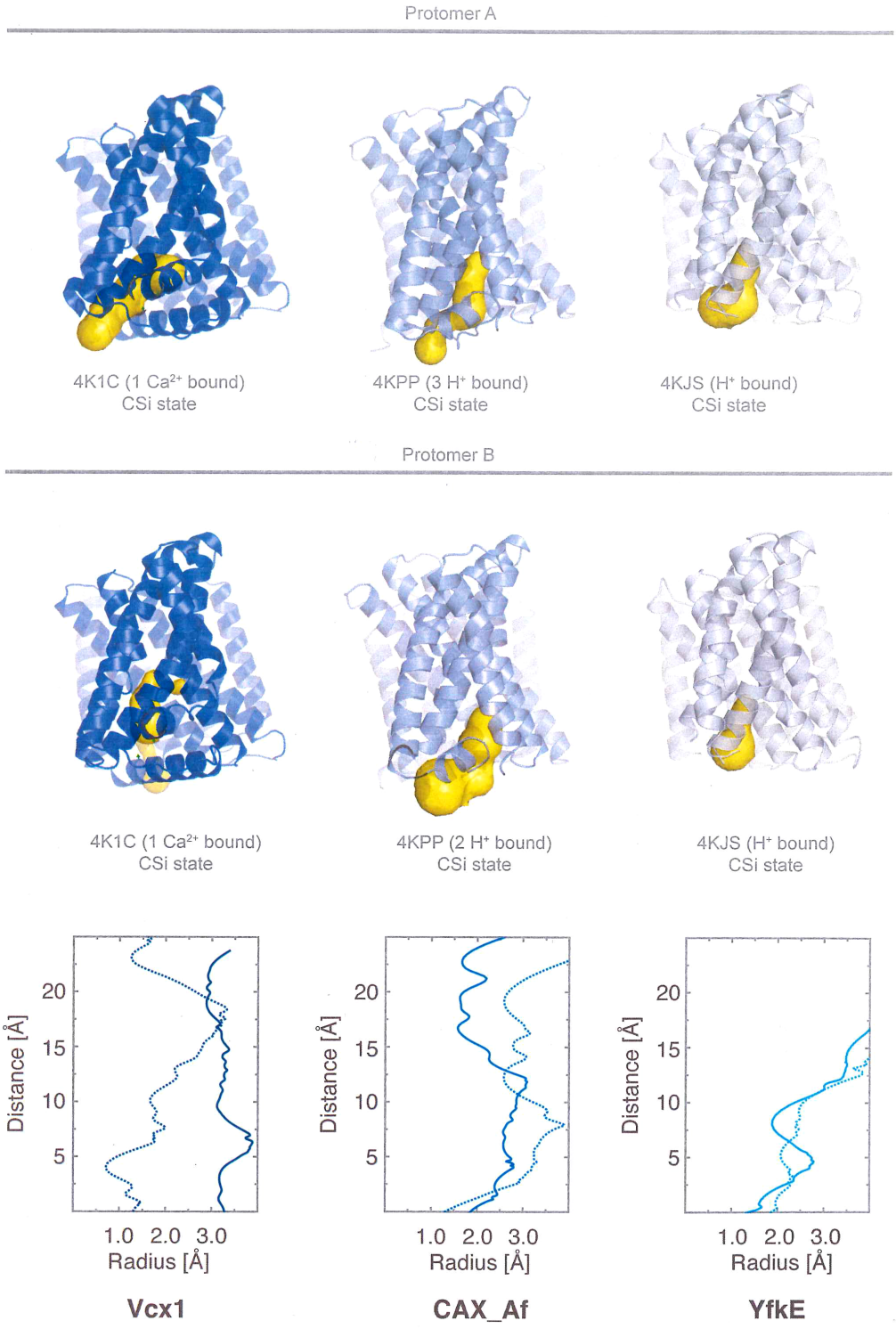


Figure 33: Ion pathway analysis of cation/$Ca^{2+}$ exchanger structures Vcx1, Cax_Af, and YfkE.

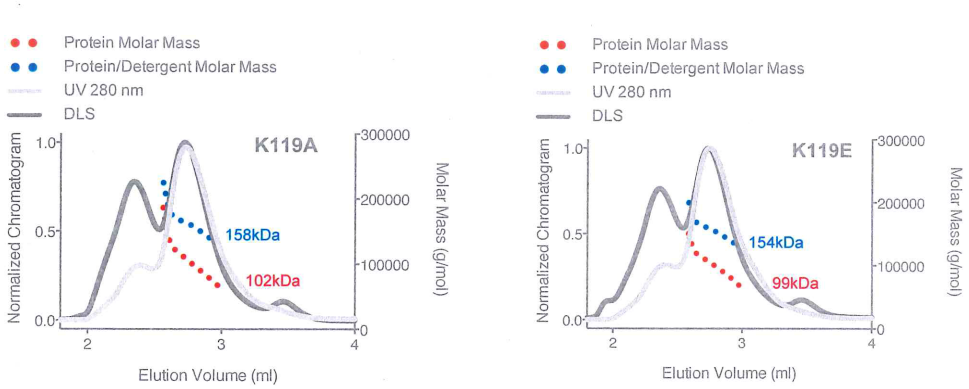


Figure 34: SEC-MALS analyses of the K119A and K119E mutants. Derived molecular weights for the protein alone (red dots) and in complex with the detergent (blue dots) were obtained. In contrast to wild-type NCX_Tm not only a single species is observed, likely influencing the molecular weight calculations.

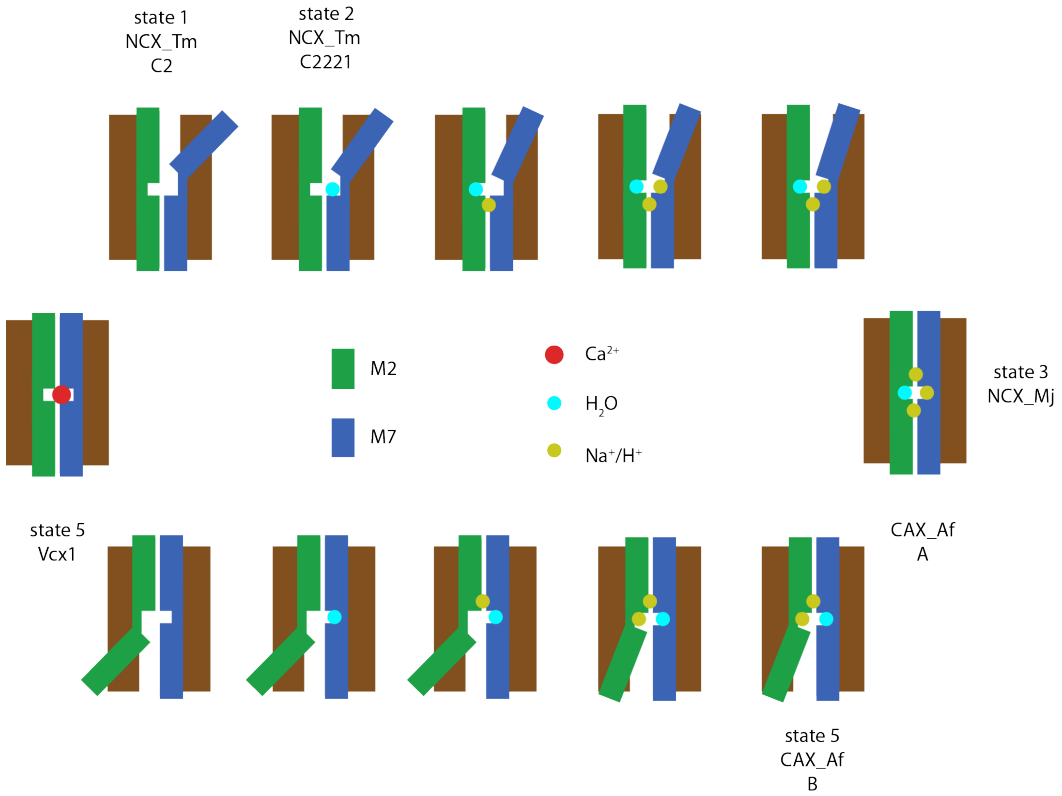


Figure 35: Transport model for NCX. Helix M2 and M7 are shown in green and blue respectively. Structures corresponding to a state are indicated. In cases a structure represents an intermediate of depicted states, corresponding structure is noted in between.

# 5 Conclusions

This thesis covered three projects for which we aimed to get deeper structural and functional understanding. The project on P-glycoprotein was accomplished and provided new insights. We provide the first occluded model of Pgp. In addition we identified and described binding sites of the third generation inhibitor zosuquidar. This can potentially help to generate new generations of optimized inhibitors. Furthermore we could show that paclitaxel is able to abrogate ATPase stimulation. Finally we described the conformational epitope of UIC2, an antibody capable to inhibit Pgp. The structure of ABCB1$_{HM-EQ}$-UIC2 I contributed was not used for model building, but it served as a link between the cross-linked ABCB1$_{HM-X}$-UIC2 and the not solved structure of human ABCB1. The similar overall structure supports the models obtained from the strongly modified constructs. The low resolution of ABCB1$_{HM-EQ}$-UIC2 is attributed to the high flexibility in absence of a crosslink.

For BSEP the goal was to obtain first structural data. We were able to generate four maps and build three models. So far the mechanism of transport is still elusive, as no model can explain all maps we obtained. Nevertheless we could come up with three potential transport models. Two of models give a potential explanation for the high substrate specificity of BSEP compared to ABCB1, by using the transport over the inner membrane leaflet or binding to the connecting loop as additional selectivity filter. In regard of glycosylation we could show that BSEP is at least glycosylated at N109 and N116. While we cannot rule out an unlikely glycosylation of N122, N125 could be shown to be involved in an interaction with helix 1 instead. As previous experiments indicated a strong impact of mutations at N125, we can assume an involvement of N125 in stabilization or functional rearrangement during the transport cycle. For the inhibitor glibenclamide we describe the binding site and show interactions of the connecting loop with the very same residues in absence of inhibitor. Very important are structural explanations for mutations leading to a disease state. This will help to better interpret future biochemical and genetic data and confirms our model. Some mutations connected with BSEP related intrahepatic cholestasis were addressed. As many questions remain unanswered, further experiments will be needed to find the correct transport model.

Our NCX project provides a first apo conformation. This helps to fill up gaps in the current list of available conformations. In addition our model gives the first structural evidence for a dimerization of a $Na^+/Ca^{2+}$ exchanger.

However we have to assume that this is a feature of the *Termotoga maritima* NCX homolog. In a transport assay we shower that NCX_Tm is actually a real $Na^+/Ca^{2+}$ exchanger like NCX_Mj, and not a $H^+/Ca^{2+}$ exchanger as assumed. Sequence alignments could show common features, which might help to predict the counter ion for other NCX homologs. Based on structures available up to date, we propose a very simple model of alternative access. This model is in line with the high exchange rate of NCX. In contrary to alternative models conformational changes of helix 1 and 6 are not considered to be part of the transport cycle.

## 6 Acknowledgments

I want to thank my thesis supervisor Henning Stahlberg for giving me the opportunity to work on many different project in a inspiring environment.

Furthermore I would like to thank my project supervisors Mark Hilge and Julia Kowal for all the training and their help in demanding projects.

Thanks to Paul Baumgartner and Inayatulla Mohammed for their help in the wetlab.

I like to thank Philippe Ringler and Mohamed Chami for many interesting discussions about electron microscopy and biological topics in general.

I'd like to thank Ricardo Righetto, and Robert McLeod for their help in processing and computer issues in general.

A big thank you goes to our EM support team, who makes sure that microscopes are performing at their best. Thanks Kenneth Goldie, Ariane Fecteau-LeFebvre, Lubomir Kovacik, and Daniel Caujolle-Bert.

I want to thank Karen Bergmann for the administrative support.

In addition I would like to thank all so far unmentioned members of C-CINA in all the years I had the luck to be part of this lab.

Finally I have to thank my family for supporting me in all the hard times, which are inevitable for every PhD-student.

## References

[1] Bin Wang, Maxim Dukarevich, Eric I. Sun, Ming Ren Yen, and Milton H. Saier. Membrane Porters of ATP-Binding Cassette Transport Systems Are Polyphyletic. *Journal of Membrane Biology*, 231(1):1, September 2009. (Cited on page 1.)

[2] Josy ter Beek, Albert Guskov, and Dirk Jan Slotboom. Structural diversity of ABC transporters. *The Journal of General Physiology*, 143(4):419–435, April 2014. (Cited on page 1.)

[3] Amy L. Davidson and Jue Chen. ATP-Binding Cassette Transporters in Bacteria. *Annual Review of Biochemistry*, 73(1):241–268, June 2004. (Cited on page 1.)

[4] Hiroshi Nikaido. How are the ABC transporters energized? *Proceedings of the National Academy of Sciences of the United States of America*, 99(15):9609–9610, July 2002. (Cited on page 2.)

[5] J. E. Walker, M. Saraste, M. J. Runswick, and N. J. Gay. Distantly related sequences in the alpha- and beta-subunits of ATP synthase, myosin, kinases and other ATP-requiring enzymes and a common nucleotide binding fold. *The EMBO journal*, 1(8):945–951, 1982. (Cited on page 2.)

[6] P. M. Jones and A. M. George. Subunit interactions in ABC transporters: towards a functional architecture. *FEMS microbiology letters*, 179(2):187–202, October 1999. (Cited on page 2.)

[7] Kaspar Hollenstein, Dominik C. Frei, and Kaspar P. Locher. Structure of an ABC transporter in complex with its binding protein. *Nature*, 446(7132):213–216, March 2007. (Cited on pages 2 and 3.)

[8] Douglas C. Rees, Eric Johnson, and Oded Lewinson. ABC transporters: The power to change. *Nature reviews. Molecular cell biology*, 10(3):218–227, March 2009. (Cited on pages 2 and 3.)

[9] M. F. Rosenberg, Q. Mao, A. Holzenburg, R. C. Ford, R. G. Deeley, and S. P. Cole. The structure of the multidrug resistance protein 1 (MRP1/ABCC1). crystallization and single-particle analysis. *The Journal of Biological Chemistry*, 276(19):16076–16082, May 2001. (Cited on page 2.)

[10] Suresh V. Ambudkar, In-Wha Kim, Di Xia, and Zuben E. Sauna. The A-loop, a novel conserved aromatic acid subdomain upstream of the Walker

A motif in ABC transporters, is critical for ATP binding. *FEBS letters*, 580(4):1049–1055, February 2006. (Cited on page 3.)

[11] Rachelle Gaudet and Don C. Wiley. Structure of the ABC ATPase domain of human TAP1, the transporter associated with antigen processing. *The EMBO Journal*, 20(17):4964–4972, September 2001. (Cited on page 3.)

[12] H. W. Pinkett, A. T. Lee, P. Lum, K. P. Locher, and D. C. Rees. An Inward-Facing Conformation of a Putative Metal-Chelate-Type ABC Transporter. *Science*, 315(5810):373–377, January 2007. (Cited on page 3.)

[13] Paul C. Smith, Nathan Karpowich, Linda Millen, Jonathan E. Moody, Jane Rosen, Philip J. Thomas, and John F. Hunt. ATP Binding to the Motor Domain from an ABC Transporter Drives Formation of a Nucleotide Sandwich Dimer. *Molecular Cell*, 10(1):139–149, July 2002. (Cited on page 3.)

[14] Grégory Verdon, Sonja V. Albers, Bauke W. Dijkstra, Arnold J. M. Driessen, and Andy-Mark W. H. Thunnissen. Crystal Structures of the ATPase Subunit of the Glucose ABC Transporter from Sulfolobus solfataricus: Nucleotide-free and Nucleotide-bound Conformations. *Journal of Molecular Biology*, 330(2):343–358, July 2003. (Cited on page 3.)

[15] Phyllis I. Hanson and Sidney W. Whiteheart. AAA+ proteins: have engine, will work. *Nature Reviews Molecular Cell Biology*, 6(7):519–529, July 2005. (Cited on page 3.)

[16] A. E. Senior, M. K. al Shawi, and I. L. Urbatsch. The catalytic cycle of P-glycoprotein. *FEBS letters*, 377(3):285–289, December 1995. (Cited on page 3.)

[17] M. Gao, H. R. Cui, D. W. Loe, C. E. Grant, K. C. Almquist, S. P. Cole, and R. G. Deeley. Comparison of the functional characteristics of the nucleotide binding domains of multidrug resistance protein 1. *The Journal of Biological Chemistry*, 275(17):13098–13108, April 2000. (Cited on page 3.)

[18] P. Borst and R. Oude Elferink. Mammalian ABC Transporters in Health and Disease. *Annual Review of Biochemistry*, 71(1):537–592, 2002. (Cited on pages 3, 6, 10 and 11.)

[19] Geoffrey Chang. Multidrug resistance ABC transporters. *FEBS Letters*, 555(1):102–105, November 2003. (Cited on page 3.)

[20] Christopher F. Higgins and Kenneth J. Linton. The ATP switch model for ABC transporters. *Nature Structural & Molecular Biology*, 11(10):918–926, October 2004. (Cited on page 4.)

[21] Frances Jane Sharom. Complex Interplay between the P-Glycoprotein Multidrug Efflux Pump and the Membrane: Its Role in Modulating Protein Function. *Frontiers in Oncology*, 4, March 2014. (Cited on pages 4, 64 and 70.)

[22] S. V. Ambudkar, S. Dey, C. A. Hrycyna, M. Ramachandra, I. Pastan, and M. M. Gottesman. Biochemical, cellular, and pharmacological aspects of the multidrug transporter. *Annual Review of Pharmacology and Toxicology*, 39:361–398, 1999. (Cited on page 4.)

[23] L. J. Bain, J. B. McLachlan, and G. A. LeBlanc. Structure-activity relationships for xenobiotic transport substrates and inhibitory ligands of P-glycoprotein. *Environmental Health Perspectives*, 105(8):812–818, August 1997. (Cited on page 4.)

[24] A. Seelig. A general pattern for substrate recognition by P-glycoprotein. *European Journal of Biochemistry*, 251(1-2):252–261, January 1998. (Cited on page 4.)

[25] A. Seelig and E. Landwojtowicz. Structure-activity relationship of P-glycoprotein substrates and modifiers. *European Journal of Pharmaceutical Sciences: Official Journal of the European Federation for Pharmaceutical Sciences*, 12(1):31–40, November 2000. (Cited on page 4.)

[26] G. D. Eytan, R. Regev, G. Oren, and Y. G. Assaraf. The role of passive transbilayer drug movement in multidrug resistance and its modulation. *The Journal of Biological Chemistry*, 271(22):12897–12902, May 1996. (Cited on page 4.)

[27] R. Regev and G. D. Eytan. Flip-flop of doxorubicin across erythrocyte and lipid membranes. *Biochemical Pharmacology*, 54(10):1151–1158, November 1997. (Cited on page 4.)

[28] I. L. Urbatsch, M. K. al Shawi, and A. E. Senior. Characterization of the ATPase activity of purified Chinese hamster P-glycoprotein. *Biochemistry*, 33(23):7069–7076, June 1994. (Cited on page 4.)

[29] S. V. Ambudkar, C. O. Cardarelli, I. Pashinsky, and W. D. Stein. Relation between the turnover number for vinblastine transport and for vinblastine-stimulated ATP hydrolysis by human P-glycoprotein. *The*

*Journal of Biological Chemistry*, 272(34):21160–21166, August 1997. (Cited on page 4.)

[30] Adam B. Shapiro, Adam B. Corder, and Victor Ling. P-Glycoprotein-Mediated Hoechst 33342 Transport Out of the Lipid Bilayer. *European Journal of Biochemistry*, 250(1):115–121, 1997. (Cited on page 4.)

[31] Adam B. Shapiro and Victor Ling. Extraction of Hoechst 33342 from the Cytoplasmic Leaflet of the Plasma Membrane by P-Glycoprotein. *European Journal of Biochemistry*, 250(1):122–129, 1997. (Cited on page 4.)

[32] Alfred H. Schinkel, Ulrich Mayer, Els Wagenaar, Carla A. A. M. Mol, Liesbeth van Deemter, Jaap J. M. Smit, Martin A. van der Valk, Arie C. Voordouw, Hergen Spits, Olaf van Tellingen, J. Mark J. M. Zijlmans, Willem E. Fibbe, and Piet Borst. Normal viability and altered pharmacokinetics in mice lacking mdr1-type (drug-transporting) P-glycoproteins. *Proceedings of the National Academy of Sciences of the United States of America*, 94(8):4028–4033, April 1997. (Cited on page 4.)

[33] Jan Wijnholds, Elizabeth C.M. de Lange, George L. Scheffer, Dirk-Jan van den Berg, Carla A.A.M. Mol, Martin van der Valk, Alfred H. Schinkel, Rik J. Scheper, Douwe D. Breimer, and Piet Borst. Multidrug resistance protein 1 protects the choroid plexus epithelium and contributes to the blood-cerebrospinal fluid barrier. *Journal of Clinical Investigation*, 105(3):279–285, February 2000. (Cited on page 4.)

[34] Dennis R. Johnson, Rick A. Finch, Z. Ping Lin, Caroline J. Zeiss, and Alan C. Sartorelli. The Pharmacological Phenotype of Combined Multidrug-Resistance mdr1a/1b- and mrp1-deficient Mice. *Cancer Research*, 61(4):1469–1476, February 2001. (Cited on page 4.)

[35] Ingolf Cascorbi. Role of pharmacogenetics of ATP-binding cassette transporters in the pharmacokinetics of drugs. *Pharmacology & Therapeutics*, 112(2):457–473, November 2006. (Cited on page 4.)

[36] Roberto Canaparo, Niklas Finnström, Loredana Serpe, Anna Nordmark, Elisabetta Muntoni, Mario Eandi, Anders Rane, and Gian Paolo Zara. Expression of CYP3a isoforms and P-glycoprotein in human stomach, jejunum and ileum. *Clinical and Experimental Pharmacology & Physiology*, 34(11):1138–1144, November 2007. (Cited on page 5.)

[37] Roberto Canaparo, Anna Nordmark, Niklas Finnström, Stefan Lundgren, Janeric Seidegård, Bengt Jeppsson, Robert J. Edwards, Alan R.

Boobis, and Anders Rane. Expression of cytochromes P450 3a and P-glycoprotein in human large intestine in paired tumour and normal samples. *Basic & Clinical Pharmacology & Toxicology*, 100(4):240–248, April 2007. (Cited on page 5.)

[38] Mari Thörn, Niklas Finnström, Stefan Lundgren, Anders Rane, and Lars Lööf. Cytochromes P450 and MDR1 mRNA expression along the human gastrointestinal tract. *British Journal of Clinical Pharmacology*, 60(1):54–60, July 2005. (Cited on page 5.)

[39] R. P. Keller, H. J. Altermatt, P. Donatsch, H. Zihlmann, J. A. Laissue, and P. C. Hiestand. Pharmacologic interactions between the resistance-modifying cyclosporine SDZ PSC 833 and etoposide (VP 16-213) enhance in vivo cytostatic activity and toxicity. *International Journal of Cancer*, 51(3):433–438, May 1992. (Cited on page 5.)

[40] S. F. Su and J. D. Huang. Inhibition of the intestinal digoxin absorption and exsorption by quinidine. *Drug Metabolism and Disposition: The Biological Fate of Chemicals*, 24(2):142–147, February 1996. (Cited on page 5.)

[41] T. Terao, E. Hisanaga, Y. Sai, I. Tamai, and A. Tsuji. Active secretion of drugs from the small intestinal epithelium in rats by P-glycoprotein functioning as an absorption barrier. *The Journal of Pharmacy and Pharmacology*, 48(10):1083–1089, October 1996. (Cited on page 5.)

[42] U. Mayer, E. Wagenaar, J. H. Beijnen, J. W. Smit, D. K. Meijer, J. van Asperen, P. Borst, and A. H. Schinkel. Substantial excretion of digoxin via the intestinal mucosa and prevention of long-term digoxin accumulation in the brain by the mdr 1a P-glycoprotein. *British Journal of Pharmacology*, 119(5):1038–1044, November 1996. (Cited on page 5.)

[43] Siegfried Drescher, Hartmut Glaeser, Thomas Mürdter, Monika Hitzl, Michel Eichelbaum, and Martin F. Fromm. P-glycoprotein-mediated intestinal and biliary digoxin transport in humans. *Clinical Pharmacology and Therapeutics*, 73(3):223–231, March 2003. (Cited on pages 5 and 7.)

[44] J. H. Schellens, M. M. Malingré, C. M. Kruijtzer, H. A. Bardelmeijer, O. van Tellingen, A. H. Schinkel, and J. H. Beijnen. Modulation of oral bioavailability of anticancer drugs: from mouse to man. *European Journal of Pharmaceutical Sciences: Official Journal of the European Federation for Pharmaceutical Sciences*, 12(2):103–110, December 2000. (Cited on page 5.)

[45] Nadia Romiti, Gianfranco Tramonti, Andrea Donati, and Elisabetta Chieli. Effects of grapefruit juice on the multidrug transporter P-glycoprotein in the human proximal tubular cell line HK-2. *Life Sciences*, 76(3):293–302, December 2004. (Cited on page 5.)

[46] Sven Deferme and Patrick Augustijns. The effect of food components on the absorption of P-gp substrates: a review. *The Journal of Pharmacy and Pharmacology*, 55(2):153–162, February 2003. (Cited on page 5.)

[47] E. G. Schuetz, K. N. Furuya, and J. D. Schuetz. Interindividual variation in expression of P-glycoprotein in normal human liver and secondary hepatic neoplasms. *The Journal of Pharmacology and Experimental Therapeutics*, 275(2):1011–1018, November 1995. (Cited on page 5.)

[48] Oliver von Richter, Oliver Burk, Martin F. Fromm, Klaus P. Thon, Michel Eichelbaum, and Kari T. Kivistö. Cytochrome P450 3a4 and P-glycoprotein Expression in Human Small Intestinal Enterocytes and Hepatocytes: A Comparative Analysis in Paired Tissue Specimens. *Clinical Pharmacology & Therapeutics*, 75(3):172–183, March 2004. (Cited on pages 5 and 7.)

[49] R. G. del Moral, A. Olmo, M. Aguilar, and F. O'Valle. P glycoprotein: a new mechanism to control drug-induced nephrotoxicity. *Experimental Nephrology*, 6(2):89–97, April 1998. (Cited on page 5.)

[50] A H Schinkel, E Wagenaar, L van Deemter, C A Mol, and P Borst. Absence of the mdr1a P-Glycoprotein in mice affects tissue distribution and pharmacokinetics of dexamethasone, digoxin, and cyclosporin A. *Journal of Clinical Investigation*, 96(4):1698–1705, October 1995. (Cited on page 5.)

[51] A H Schinkel. Disruption of the mouse mdr1a P-glycoprotein gene leads to a deficiency in the blood-brain barrier and to increased sensitivity to drugs - ScienceDirect, 1994. (Cited on pages 5 and 6.)

[52] Alfred H Schinkel. P-Glycoprotein, a gatekeeper in the blood–brain barrier. *Advanced Drug Delivery Reviews*, 36(2):179–194, April 1999. (Cited on page 5.)

[53] Ikumi Tamai and Akira Tsuji. Transporter-Mediated Permeation of Drugs Across the Blood–Brain Barrier. *Journal of Pharmaceutical Sciences*, 89(11):1371–1388, November 2000. (Cited on page 5.)

[54] M. F. Fromm. P-glycoprotein: a defense mechanism limiting oral bioavailability and CNS accumulation of drugs. *International Journal*

*of Clinical Pharmacology and Therapeutics*, 38(2):69–74, February 2000. (Cited on page 5.)

[55] Amber M Young, Courtni E Allen, and Kenneth L Audus. Efflux transporters of the human placenta. *Advanced Drug Delivery Reviews*, 55(1):125–132, January 2003. (Cited on page 5.)

[56] J. W. Smit, M. T. Huisman, O. van Tellingen, H. R. Wiltshire, and A. H. Schinkel. Absence or pharmacological blocking of placental P-glycoprotein profoundly increases fetal drug exposure. *The Journal of Clinical Investigation*, 104(10):1441–1447, November 1999. (Cited on page 5.)

[57] G. R. Lankas, L. D. Wise, M. E. Cartwright, T. Pippert, and D. R. Umbenhauer. Placental P-glycoprotein deficiency enhances susceptibility to chemically induced birth defects in mice. *Reproductive Toxicology (Elmsford, N.Y.)*, 12(4):457–463, August 1998. (Cited on page 6.)

[58] P. M. Chaudhary, E. B. Mechetner, and I. B. Roninson. Expression and activity of the multidrug resistance P-glycoprotein in human peripheral blood lymphocytes. *Blood*, 80(11):2735–2739, December 1992. (Cited on page 6.)

[59] P. M. Chaudhary and I. B. Roninson. Expression and activity of P-glycoprotein, a multidrug efflux pump, in human hematopoietic stem cells. *Cell*, 66(1):85–94, July 1991. (Cited on page 6.)

[60] Arcadi I. Svirnovski, Tatsiana V. Shman, Tatsiana F. Serhiyenka, Valery P. Savitski, Victoria V. Smolnikova, and Uladzimir U. Fedasenka. ABCB1 and ABCG2 proteins, their functional activity and gene expression in concert with drug sensitivity of leukemia cells. *Hematology (Amsterdam, Netherlands)*, 14(4):204–212, August 2009. (Cited on page 6.)

[61] K. Jones, P. G. Bray, S. H. Khoo, R. A. Davey, E. R. Meaden, S. A. Ward, and D. J. Back. P-Glycoprotein and transporter MRP1 reduce HIV protease inhibitor uptake in CD4 cells: potential for accelerated viral drug resistance? *AIDS (London, England)*, 15(11):1353–1358, July 2001. (Cited on page 6.)

[62] S. Hoffmeyer, O. Burk, O. von Richter, H. P. Arnold, J. Brockmöller, A. Johne, I. Cascorbi, T. Gerloff, I. Roots, M. Eichelbaum, and U. Brinkmann. Functional polymorphisms of the human multidrug-resistance gene: multiple sequence variations and correlation of one allele with P-glycoprotein expression and activity in vivo. *Proceedings*

*of the National Academy of Sciences of the United States of America*, 97(7):3473–3478, March 2000. (Cited on pages 6 and 7.)

[63] I. Cascorbi, T. Gerloff, A. Johne, C. Meisel, S. Hoffmeyer, M. Schwab, E. Schaeffeler, M. Eichelbaum, U. Brinkmann, and I. Roots. Frequency of single nucleotide polymorphisms in the P-glycoprotein drug transporter MDR1 gene in white subjects. *Clinical Pharmacology and Therapeutics*, 69(3):169–174, March 2001. (Cited on page 6.)

[64] Soichiro Ito, Ichiro Ieiri, Mizuho Tanabe, Akito Suzuki, Shun Higuchi, and Kenji Otsubo. Polymorphism of the Abc transporter genes, *mdr1*, *mrp1* and **mrp2/cmoat**, in healthy Japanese subjects. *Pharmacogenetics*, 11(2):175–184, March 2001. (Cited on page 6.)

[65] M. Tanabe, I. Ieiri, N. Nagata, K. Inoue, S. Ito, Y. Kanamori, M. Takahashi, Y. Kurata, J. Kigawa, S. Higuchi, N. Terakawa, and K. Otsubo. Expression of P-glycoprotein in human placenta: relation to genetic polymorphism of the multidrug resistance (MDR)-1 gene. *The Journal of Pharmacology and Experimental Therapeutics*, 297(3):1137–1143, June 2001. (Cited on page 6.)

[66] G. R. Lankas, M. E. Cartwright, and D. Umbenhauer. P-glycoprotein deficiency in a subpopulation of CF-1 mice enhances avermectin-induced neurotoxicity. *Toxicology and Applied Pharmacology*, 143(2):357–365, April 1997. (Cited on page 6.)

[67] Melanie Schaefer, Ivar Roots, and Thomas Gerloff. In-vitro transport characteristics discriminate wild-type ABCB1 (MDR1) from ALA893ser and ALA893thr polymorphisms. *Pharmacogenetics and Genomics*, 16(12):855–861, December 2006. (Cited on page 6.)

[68] S. Dulucq, S. Bouchet, B. Turcq, E. Lippert, G. Etienne, J. Reiffers, M. Molimard, M. Krajinovic, and F.-X. Mahon. Multidrug resistance gene (MDR1) polymorphisms are associated with major molecular responses to standard-dose imatinib in chronic myeloid leukemia. *Blood*, 112(5):2024–2027, September 2008. (Cited on page 7.)

[69] M. M. Ameyaw, F. Regateiro, T. Li, X. Liu, M. Tariq, A. Mobarek, N. Thornton, G. O. Folayan, J. Githang'a, A. Indalo, D. Ofori-Adjei, D. A. Price-Evans, and H. L. McLeod. MDR1 pharmacogenetics: frequency of the C3435t mutation in exon 26 is significantly influenced by ethnicity. *Pharmacogenetics*, 11(3):217–221, April 2001. (Cited on page 7.)

[70] Elke Schaeffeler, Michel Eichelbaum, Ulrich Brinkmann, Anja Penger, Steven Asante-Poku, Ulrich M Zanger, and Matthias Schwab. Frequency of C3435t polymorphism of MDR1 gene in African people. *The Lancet*, 358(9279):383–384, August 2001. (Cited on page 7.)

[71] Jun Lee, Rongrong Wang, Yuan Yang, Xiaoyang Lu, Xingguo Zhang, Linrun Wang, and Yan Lou. The Effect of ABCB1 C3435t Polymorphism on Cyclosporine Dose Requirements in Kidney Transplant Recipients: A Meta-Analysis. *Basic & Clinical Pharmacology & Toxicology*, 117(2):117–125, August 2015. (Cited on page 7.)

[72] Matthew H. Crouthamel, Daniel Wu, Ziping Yang, and Rodney J. Y. Ho. A novel MDR1 G1199t variant alters drug resistance and efflux transport activity of P-glycoprotein in recombinant Hek cells. *Journal of Pharmaceutical Sciences*, 95(12):2767–2777, December 2006. (Cited on page 7.)

[73] Ziping Yang, Daniel Wu, Tot Bui, and Rodney J. Y. Ho. A novel human multidrug resistance gene MDR1 variant G571a (G191r) modulates cancer drug resistance and efflux transport. *The Journal of Pharmacology and Experimental Therapeutics*, 327(2):474–481, November 2008. (Cited on page 7.)

[74] Ge Zhou and M. Tien Kuo. NF-κB-mediated Induction of mdr1b Expression by Insulin in Rat Hepatoma Cells. *Journal of Biological Chemistry*, 272(24):15174–15183, June 1997. (Cited on page 7.)

[75] J. M. Yang, A. D. Vassil, and W. N. Hait. Activation of phospholipase C induces the expression of the multidrug resistance (MDR1) gene through the Raf-MAPK pathway. *Molecular Pharmacology*, 60(4):674–680, October 2001. (Cited on page 7.)

[76] A. Geick, M. Eichelbaum, and O. Burk. Nuclear receptor response elements mediate induction of intestinal MDR1 by rifampin. *The Journal of Biological Chemistry*, 276(18):14581–14587, May 2001. (Cited on page 7.)

[77] Rommel G. Tirona, Wooin Lee, Brenda F. Leake, Lu-Bin Lan, Cynthia Brimer Cline, Vishal Lamba, Fereshteh Parviz, Stephen A. Duncan, Yusuke Inoue, Frank J. Gonzalez, Erin G. Schuetz, and Richard B. Kim. The orphan nuclear receptor HNF4alpha determines PXR- and CAR-mediated xenobiotic induction of CYP3a4. *Nature Medicine*, 9(2):220–224, February 2003. (Cited on page 7.)

[78] Yoav E. Timsit and Masahiko Negishi. CAR and PXR: The Xenobiotic-Sensing Receptors. *Steroids*, 72(3):231–246, March 2007. (Cited on page 7.)

[79] M. E. Cavet, M. West, and N. L. Simmons. Transport and epithelial secretion of the cardiac glycoside, digoxin, by human intestinal epithelial (Caco-2) cells. *British Journal of Pharmacology*, 118(6):1389–1396, July 1996. (Cited on page 7.)

[80] E. B. Leahey, J. A. Reiffel, R. E. Drusin, R. H. Heissenbuttel, W. P. Lovejoy, and J. T. Bigger. Interaction between quinidine and digoxin. *JAMA*, 240(6):533–534, August 1978. (Cited on page 7.)

[81] Piet Borst and Alfred H. Schinkel. P-glycoprotein ABCB1: a major player in drug handling by mammals. *The Journal of Clinical Investigation*, 123(10):4131–4133, October 2013. (Cited on pages 10 and 11.)

[82] Martin F. Fromm. Importance of P-glycoprotein at blood–tissue barriers - ScienceDirect, August 2004. (Cited on pages 8 and 11.)

[83] K. M. Hillgren, D. Keppler, A. A. Zur, K. M. Giacomini, B. Stieger, C. E. Cass, and L. Zhang. Emerging transporters of clinical importance: an update from the International Transporter Consortium. *Clinical Pharmacology and Therapeutics*, 94(1):52–63, 2013. (Cited on page 11.)

[84] Wolfgang Löscher and Heidrun Potschka. Drug resistance in brain diseases and the role of drug efflux transporters. *Nature Reviews Neuroscience*, 6(8):591–602, August 2005. (Cited on page 11.)

[85] Balázs Sarkadi, László Homolya, Gergely Szakács, and András Váradi. Human Multidrug Resistance ABCB and ABCG Transporters: Participation in a Chemoimmunity Defense System. *Physiological Reviews*, 86(4):1179–1236, October 2006. (Cited on page 11.)

[86] Michael M. Gottesman, Tito Fojo, and Susan E. Bates. Multidrug resistance in cancer: role of ATP–dependent transporters. *Nature Reviews Cancer*, 2(1):48–58, January 2002. (Cited on page 11.)

[87] Katalin Goda, Ferenc Fenyvesi, Zsolt Bacsó, Henrietta Nagy, Teréz Márián, Attila Megyeri, Zoltán Krasznai, István Juhász, Miklós Vecsernyés, and Gábor Szabó. Complete Inhibition of P-glycoprotein by Simultaneous Treatment with a Distinct Class of Modulators and the UIC2 Monoclonal Antibody. *Journal of Pharmacology and Experimental Therapeutics*, 320(1):81–88, January 2007. (Cited on pages 11 and 15.)

[88] E B Mechetner and I B Roninson. Efficient inhibition of P-glycoprotein-mediated multidrug resistance with a monoclonal antibody. *Proceedings of the National Academy of Sciences of the United States of America*, 89(13):5824–5828, July 1992. (Cited on page 11.)

[89] Todd E. Druley, Wilfred D. Stein, and Igor B. Roninson. Analysis of MDR1 P-Glycoprotein Conformational Changes in Permeabilized Cells Using Differential Immunoreactivity. *Biochemistry*, 40(14):4312–4322, April 2001. (Cited on page 11.)

[90] Eugene B. Mechetner, Brigitte Schott, Brian S. Morse, Wilfred D. Stein, Todd Druley, Kenneth A. Davis, Takashi Tsuruo, and Igor B. Roninson. P-glycoprotein function involves conformational transitions detectable by differential immunoreactivity. *Proceedings of the National Academy of Sciences of the United States of America*, 94(24):12908–12913, November 1997. (Cited on pages 11 and 15.)

[91] Lothar Esser, Suneet Shukla, Fei Zhou, Suresh V. Ambudkar, and Di Xia. Crystal structure of the antigen-binding fragment of a monoclonal antibody specific for the multidrug-resistance-linked ABC transporter human P-glycoprotein. *Acta Crystallographica. Section F, Structural Biology Communications*, 72(Pt 8):636–641, July 2016. (Cited on page 11.)

[92] Gabriel A. Frank, Suneet Shukla, Prashant Rao, Mario J. Borgnia, Alberto Bartesaghi, Alan Merk, Aerfa Mobin, Lothar Esser, Lesley A. Earl, Michael M. Gottesman, Di Xia, Suresh V. Ambudkar, and Sriram Subramaniam. Cryo-EM Analysis of the Conformational Landscape of Human P-glycoprotein (ABCB1) During its Catalytic Cycle. *Molecular Pharmacology*, 90(1):35–41, July 2016. (Cited on pages 11, 12, 19 and 22.)

[93] Stephen G. Aller, Jodie Yu, Andrew Ward, Yue Weng, Srinivas Chittaboina, Rupeng Zhuo, Patina M. Harrell, Yenphuong T. Trinh, Qinghai Zhang, Ina L. Urbatsch, and Geoffrey Chang. Structure of P-glycoprotein Reveals a Molecular Basis for Poly-Specific Drug Binding. *Science (New York, N.Y.)*, 323(5922):1718–1722, March 2009. (Cited on pages 11 and 16.)

[94] Jingzhi Li, Kimberly F Jaimes, and Stephen G Aller. Refined structures of mouse P-glycoprotein. *Protein Science : A Publication of the Protein Society*, 23(1):34–46, January 2014. (Cited on pages 11, 15, 16 and 19.)

[95] Mi Sun Jin, Michael L. Oldham, Qiuju Zhang, and Jue Chen. Crystal structure of the multidrug transporter P-glycoprotein from C. ele-

gans. *Nature*, 490(7421):566–569, October 2012. (Cited on pages 11, 19 and 22.)

[96] Sascha C. T. Nicklisch, Steven D. Rees, Aaron P. McGrath, Tufan Gökirmak, Lindsay T. Bonito, Lydia M. Vermeer, Cristina Cregger, Greg Loewen, Stuart Sandin, Geoffrey Chang, and Amro Hamdoun. Global marine pollutants inhibit P-glycoprotein: Environmental levels, inhibitory effects, and cocrystal structure. *Science Advances*, 2(4), April 2016. (Cited on pages 11 and 16.)

[97] Lothar Esser, Fei Zhou, Kristen M. Pluchino, Joseph Shiloach, Jichun Ma, Wai-kwan Tang, Camilo Gutierrez, Alex Zhang, Suneet Shukla, James P. Madigan, Tongqing Zhou, Peter D. Kwong, Suresh V. Ambudkar, Michael M. Gottesman, and Di Xia. Structures of the Multidrug Transporter P-glycoprotein Reveal Asymmetric ATP Binding and the Mechanism of Polyspecificity. *The Journal of Biological Chemistry*, 292(2):446–461, January 2017. (Cited on pages 11, 14, 15 and 19.)

[98] Elizabeth Fox and Susan E. Bates. Tariquidar (XR9576): a P-glycoprotein drug efflux pump inhibitor. *Expert Review of Anticancer Therapy*, 7(4):447–459, April 2007. (Cited on page 11.)

[99] Anne H. Dantzig, Robert L. Shepard, Jin Cao, Kevin L. Law, William J. Ehlhardt, Todd M. Baughman, Thomas F. Bumol, and James J. Starling. Reversal of P-Glycoprotein-mediated Multidrug Resistance by a Potent Cyclopropyldibenzosuberane Modulator, LY335979. *Cancer Research*, 56(18):4171–4179, September 1996. (Cited on page 11.)

[100] Ranjeet Prasad Dash, R. Jayachandra Babu, and Nuggehally R. Srinivas. Therapeutic Potential and Utility of Elacridar with Respect to P-glycoprotein Inhibition: An Insight from the Published In Vitro, Preclinical and Clinical Studies. *European Journal of Drug Metabolism and Pharmacokinetics*, 42(6):915–933, December 2017. (Cited on page 11.)

[101] Robert W. Robey, Paul R. Massey, Laleh Amiri-Kordestani, and Susan E. Bates. ABC Transporters: Unvalidated Therapeutic Targets in Cancer and the CNS. *Anti-cancer agents in medicinal chemistry*, 10(8):625–633, October 2010. (Cited on page 11.)

[102] W. T. Beck, T. M. Grogan, C. L. Willman, C. Cordon-Cardo, D. M. Parham, J. F. Kuttesch, M. Andreeff, S. E. Bates, C. W. Berard, J. M. Boyett, N. A. Brophy, H. J. Broxterman, H. S. Chan, W. S. Dalton, M. Dietel, A. T. Fojo, R. D. Gascoyne, D. Head, P. J. Houghton, D. K.

Srivastava, M. Lehnert, C. P. Leith, E. Paietta, Z. P. Pavelic, and R. Weinstein. Methods to detect P-glycoprotein-associated multidrug resistance in patients' tumors: consensus recommendations. *Cancer Research*, 56(13):3010–3020, July 1996. (Cited on page 11.)

[103] Suneet Shukla, Biebele Abel, Eduardo E. Chufan, and Suresh V. Ambudkar. Effects of a detergent micelle environment on P-glycoprotein (ABCB1)-ligand interactions. *The Journal of Biological Chemistry*, 292(17):7066–7076, April 2017. (Cited on pages 11, 21 and 22.)

[104] Vladimir M. Korkhov, Samantha A. Mireku, and Kaspar P. Locher. Structure of AMP-PNP-bound vitamin $B_{12}$ transporter BtuCD–F. *Nature*, 490(7420):367–372, October 2012. (Cited on page 12.)

[105] Michael Hohl, Lea M. Hürlimann, Simon Böhm, Jendrik Schöppe, Markus G. Grütter, Enrica Bordignon, and Markus A. Seeger. Structural basis for allosteric cross-talk between the asymmetric nucleotide binding sites of a heterodimeric ABC exporter. *Proceedings of the National Academy of Sciences of the United States of America*, 111(30):11025–11030, July 2014. (Cited on page 12.)

[106] Tip W. Loo and David M. Clarke. P-glycoprotein ATPase activity requires lipids to activate a switch at the first transmission interface. *Biochemical and Biophysical Research Communications*, 472(2):379–383, April 2016. (Cited on page 12.)

[107] Michael Hohl, Christophe Briand, Markus G. Grütter, and Markus A. Seeger. Crystal structure of a heterodimeric ABC transporter in its inward-facing conformation. *Nature Structural & Molecular Biology*, 19(4):395–402, April 2012. (Cited on pages 14 and 16.)

[108] Isabelle Carrier, Michel Julien, and Philippe Gros. Analysis of Catalytic Carboxylate Mutants E552q and E1197q Suggests Asymmetric ATP Hydrolysis by the Two Nucleotide-Binding Domains of P-Glycoprotein. *Biochemistry*, 42(44):12875–12885, November 2003. (Cited on pages 14 and 30.)

[109] Anne Nöll, Christoph Thomas, Valentina Herbring, Tina Zollmann, Katja Barth, Ahmad Reza Mehdipour, Thomas M. Tomasiak, Stefan Brüchert, Benesh Joseph, Rupert Abele, Vincent Oliéric, Meitian Wang, Kay Diederichs, Gerhard Hummer, Robert M. Stroud, Klaas M. Pos, and Robert Tampé. Crystal structure and mechanistic basis of a functional homolog of the antigen transporter TAP. *Proceedings of the National*

*Academy of Sciences of the United States of America*, 114(4):E438–E447, January 2017. (Cited on page 14.)

[110] Brandy Verhalen, Reza Dastvan, Sundarapandian Thangapandian, Yelena Peskova, Hanane A. Koteiche, Robert K. Nakamoto, Emad Tajkhorshid, and Hassane S. Mchaourab. Energy Transduction and Alternating Access of the Mammalian ABC Transporter P-glycoprotein. *Nature*, 543(7647):738–741, March 2017. (Cited on page 15.)

[111] Roger J. P. Dawson and Kaspar P. Locher. Structure of a bacterial multidrug ABC transporter. *Nature*, 443(7108):180–185, September 2006. (Cited on page 15.)

[112] Tasha K. Ritchie, Hyewon Kwon, and William M. Atkins. Conformational Analysis of Human ATP-binding Cassette Transporter ABCB1 in Lipid Nanodiscs and Inhibition by the Antibodies MRK16 and UIC2. *The Journal of Biological Chemistry*, 286(45):39489–39496, November 2011. (Cited on pages 15 and 19.)

[113] Hassanul G. Choudhury, Zhen Tong, Indran Mathavan, Yanyan Li, So Iwata, Séverine Zirah, Sylvie Rebuffat, Hendrik W. van Veen, and Konstantinos Beis. Structure of an antibacterial peptide ATP-binding cassette transporter in a novel outward occluded state. *Proceedings of the National Academy of Sciences of the United States of America*, 111(25):9145–9150, June 2014. (Cited on page 16.)

[114] Zhe Zhang, Fangyu Liu, and Jue Chen. Conformational Changes of CFTR upon Phosphorylation and ATP Binding. *Cell*, 170(3):483–491.e8, July 2017. (Cited on page 16.)

[115] Kaspar P. Locher. Mechanistic diversity in ATP-binding cassette (ABC) transporters. *Nature Structural & Molecular Biology*, 23(6):487–493, 2016. (Cited on page 16.)

[116] Eduardo E. Chufan, Khyati Kapoor, and Suresh V. Ambudkar. Drug-Protein Hydrogen Bonds Govern the Inhibition of the ATP Hydrolysis of the Multidrug Transporter P-glycoprotein. *Biochemical pharmacology*, 101:40–53, February 2016. (Cited on page 16.)

[117] Tip W. Loo and David M. Clarke. Mapping the Binding Site of the Inhibitor Tariquidar That Stabilizes the First Transmembrane Domain of P-glycoprotein. *The Journal of Biological Chemistry*, 290(49):29389–29401, December 2015. (Cited on pages 16 and 20.)

[118] Ilza K. Pajeva, Katja Sterz, Matthias Christlieb, Kerstin Steggemann, Federico Marighetti, and Michael Wiese. Interactions of the Multidrug Resistance Modulators Tariquidar and Elacridar and their Analogues with P-glycoprotein. *ChemMedChem*, 8(10):1701–1713, October 2013. (Cited on page 16.)

[119] Tip W. Loo and David M. Clarke. Mutational analysis of ABC proteins. *Archives of Biochemistry and Biophysics*, 476(1):51–64, August 2008. (Cited on page 16.)

[120] Tip W. Loo and David M. Clarke. [35] Mutational analysis of human P-glycoprotein. In *Methods in Enzymology*, volume 292 of *ABC Transporters: Biochemical, Cellular, and Molecular Aspects*, pages 480–492. Academic Press, January 1998. (Cited on page 16.)

[121] Eduardo E. Chufan, Khyati Kapoor, Hong-May Sim, Satyakam Singh, Tanaji T. Talele, Stewart R. Durell, and Suresh V. Ambudkar. Multiple Transport-Active Binding Sites Are Available for a Single Substrate on Human P-Glycoprotein (ABCB1). *PLoS ONE*, 8(12), December 2013. (Cited on page 16.)

[122] Paul Szewczyk, Houchao Tao, Aaron P. McGrath, Mark Villaluz, Steven D. Rees, Sung Chang Lee, Rupak Doshi, Ina L. Urbatsch, Qinghai Zhang, and Geoffrey Chang. Snapshots of ligand entry, malleable binding and induced helical movement in P-glycoprotein. *Acta Crystallographica Section D: Biological Crystallography*, 71(Pt 3):732–741, February 2015. (Cited on pages 16, 17, 19 and 22.)

[123] Tip W. Loo, M. Claire Bartlett, and David M. Clarke. Permanent activation of the human P-glycoprotein by covalent modification of a residue in the drug-binding site. *The Journal of Biological Chemistry*, 278(23):20449–20452, June 2003. (Cited on page 16.)

[124] Tip W. Loo, M. Claire Bartlett, and David M. Clarke. Simultaneous binding of two different drugs in the binding pocket of the human multidrug resistance P-glycoprotein. *The Journal of Biological Chemistry*, 278(41):39706–39710, October 2003. (Cited on page 17.)

[125] Tip W. Loo, M. Claire Bartlett, and David M. Clarke. Substrate-induced Conformational Changes in the Transmembrane Segments of Human P-glycoprotein DIRECT EVIDENCE FOR THE SUBSTRATE-INDUCED FIT MECHANISM FOR DRUG BINDING. *Journal of Biological Chemistry*, 278(16):13603–13606, April 2003. (Cited on page 17.)

[126] Zachary Lee Johnson and Jue Chen. Structural Basis of Substrate Recognition by the Multidrug Resistance Protein MRP1. *Cell*, 168(6):1075–1085.e9, March 2017. (Cited on page 20.)

[127] Vasundara Srinivasan, Antonio J. Pierik, and Roland Lill. Crystal structures of nucleotide-free and glutathione-bound mitochondrial ABC transporter Atm1. *Science (New York, N.Y.)*, 343(6175):1137–1140, March 2014. (Cited on page 22.)

[128] Gaurav Backliwal, Markus Hildinger, Sebastien Chenuet, Maria Dejesus, and Florian M. Wurm. Coexpression of acidic fibroblast growth factor enhances specific productivity and antibody titers in transiently transfected HEK293 cells. *New Biotechnology*, 25(2-3):162–166, December 2008. (Cited on page 24.)

[129] Tuan Anh Nguyen, Myung Hyun Jo, Yeon-Gil Choi, Joha Park, S. Chul Kwon, Sungchul Hohng, V. Narry Kim, and Jae-Sung Woo. Functional Anatomy of the Human Microprocessor. *Cell*, 161(6):1374–1387, June 2015. (Cited on page 24.)

[130] S. Chifflet, A. Torriglia, R. Chiesa, and S. Tolosa. A method for the determination of inorganic phosphate in the presence of labile organic phosphate and high concentrations of protein: application to lens ATPases. *Analytical Biochemistry*, 168(1):1–4, January 1988. (Cited on page 26.)

[131] Shawn Q. Zheng, Eugene Palovcak, Jean-Paul Armache, Kliment A. Verba, Yifan Cheng, and David A. Agard. MotionCor2 - anisotropic correction of beam-induced motion for improved cryo-electron microscopy. *Nature methods*, 14(4):331–332, April 2017. (Cited on pages 28 and 52.)

[132] Kai Zhang. Gctf: Real-time CTF determination and correction. *Journal of Structural Biology*, 193(1):1–12, January 2016. (Cited on page 28.)

[133] Sjors H.W. Scheres. RELION: Implementation of a Bayesian approach to cryo-EM structure determination. *Journal of Structural Biology*, 180(3):519–530, December 2012. (Cited on page 28.)

[134] Sjors H.W. Scheres. A Bayesian View on Cryo-EM Structure Determination. *Journal of Molecular Biology*, 415(2-4):406–418, January 2012. (Cited on page 28.)

[135] Dari Kimanius, Björn O Forsberg, Sjors HW Scheres, and Erik Lindahl. Accelerated cryo-EM structure determination with parallelisation using GPUs in RELION-2. *eLife*, 5, November 2016. (Cited on page 28.)

[136] Eric F. Pettersen, Thomas D. Goddard, Conrad C. Huang, Gregory S. Couch, Daniel M. Greenblatt, Elaine C. Meng, and Thomas E. Ferrin. UCSF Chimera–a visualization system for exploratory research and analysis. *Journal of Computational Chemistry*, 25(13):1605–1612, October 2004. (Cited on page 28.)

[137] Sjors H.W. Scheres and Shaoxia Chen. Prevention of overfitting in cryo-EM structure determination. *Nature methods*, 9(9):853–854, September 2012. (Cited on page 28.)

[138] Alp Kucukelbir, Fred J. Sigworth, and Hemant D. Tagare. The Local Resolution of Cryo-EM Density Maps. *Nature methods*, 11(1):63–65, January 2014. (Cited on page 28.)

[139] Nikhil Biyani, Ricardo D. Righetto, Robert McLeod, Daniel Caujolle-Bert, Daniel Castano-Diez, Kenneth N. Goldie, and Henning Stahlberg. Focus: The interface between data collection and data processing in cryo-EM. *Journal of Structural Biology*, 198(2):124–133, 2017. (Cited on pages 30 and 52.)

[140] Linas Urnavicius, Kai Zhang, Aristides G. Diamant, Carina Motz, Max A. Schlager, Minmin Yu, Nisha A. Patel, Carol V. Robinson, and Andrew P. Carter. The structure of the dynactin complex and its interaction with dynein. *Science (New York, N.Y.)*, 347(6229):1441–1446, March 2015. (Cited on pages 30 and 52.)

[141] Guang Tang, Liwei Peng, Philip R. Baldwin, Deepinder S. Mann, Wen Jiang, Ian Rees, and Steven J. Ludtke. EMAN2: An extensible image processing suite for electron microscopy. *Journal of Structural Biology*, 157(1):38–46, January 2007. (Cited on pages 30 and 52.)

[142] P. Emsley, B. Lohkamp, W. G. Scott, and K. Cowtan. Features and development of Coot. *Acta Crystallographica Section D: Biological Crystallography*, 66(Pt 4):486–501, April 2010. (Cited on pages 30 and 54.)

[143] Alan Brown, Fei Long, Robert A. Nicholls, Jaan Toots, Paul Emsley, and Garib Murshudov. Tools for macromolecular model building and refinement into electron cryo-microscopy reconstructions. *Acta Crystallographica Section D: Biological Crystallography*, 71(Pt 1):136–153, January 2015. (Cited on page 31.)

[144] Paul D. Adams, Pavel V. Afonine, Gábor Bunkóczi, Vincent B. Chen, Ian W. Davis, Nathaniel Echols, Jeffrey J. Headd, Li-Wei Hung, Gary J. Kapral, Ralf W. Grosse-Kunstleve, Airlie J. McCoy, Nigel W. Moriarty,

Robert Oeffner, Randy J. Read, David C. Richardson, Jane S. Richardson, Thomas C. Terwilliger, and Peter H. Zwart. PHENIX: a comprehensive Python-based system for macromolecular structure solution. *Acta Crystallographica Section D: Biological Crystallography*, 66(Pt 2):213–221, February 2010. (Cited on pages 31, 54 and 84.)

[145] Bosco K Ho and Franz Gruswitz. HOLLOW: Generating Accurate Representations of Channel and Interior Surfaces in Molecular Structures. *BMC Structural Biology*, 8:49, November 2008. (Cited on page 31.)

[146] Roman A. Laskowski and Mark B. Swindells. LigPlot+: Multiple Ligand–Protein Interaction Diagrams for Drug Discovery. *Journal of Chemical Information and Modeling*, 51(10):2778–2786, October 2011. (Cited on page 31.)

[147] James L. Boyer. Bile formation and secretion. *Comprehensive Physiology*, 3(3):1035–1078, July 2013. (Cited on page 46.)

[148] Joseph Feher. 8.4 - Pancreatic and Biliary Secretion. In *Quantitative Human Physiology (Second Edition)*, pages 810–820. Academic Press, Boston, 2017. (Cited on page 46.)

[149] Melanie Hundt and Savio John. Physiology, Bile Secretion. In *StatPearls*. StatPearls Publishing, Treasure Island (FL), 2018. (Cited on page 46.)

[150] Paul A. Dawson. Role of the intestinal bile acid transporters in bile acid and drug disposition. *Handbook of Experimental Pharmacology*, (201):169–203, 2011. (Cited on page 46.)

[151] B. Hagenbuch, B. Stieger, M. Foguet, H. Lübbert, and P. J. Meier. Functional expression cloning and characterization of the hepatocyte Na+/bile acid cotransport system. *Proceedings of the National Academy of Sciences of the United States of America*, 88(23):10629–10633, December 1991. (Cited on page 46.)

[152] Christiane Pauli-Magnus, Bruno Stieger, Yvonne Meier, Gerd A. Kullak-Ublick, and Peter J. Meier. Enterohepatic transport of bile salts and genetics of cholestasis. *Journal of Hepatology*, 43(2):342–357, August 2005. (Cited on pages 46, 49 and 50.)

[153] Alan F. Hofmann. Bile acids: trying to understand their chemistry and biology with the hope of helping patients. *Hepatology (Baltimore, Md.)*, 49(5):1403–1418, May 2009. (Cited on page 46.)

[154] S. Kevresan, K. Kuhajda, J. Kandrac, J. P. Fawcett, and M. Mikov. Biosynthesis of bile acids in mammalian liver. *European Journal of Drug Metabolism and Pharmacokinetics*, 31(3):145–156, September 2006. (Cited on pages 47 and 48.)

[155] Jiro Jerry Kaneko, John W. Harvey, and Michael L. Bruss. *Clinical Biochemistry of Domestic Animals*. Academic Press, September 2008. Google-Books-ID: spsD4WQbL0QC. (Cited on pages 47 and 48.)

[156] Ping Lam, Carol J. Soroka, and James L. Boyer. The bile salt export pump: clinical and experimental aspects of genetic and acquired cholestatic liver disease. *Seminars in Liver Disease*, 30(2):125–133, May 2010. (Cited on page 48.)

[157] Kaori Mochizuki, Tatehiro Kagawa, Asano Numari, Matthew J. Harris, Johbu Itoh, Norihito Watanabe, Tetsuya Mine, and Irwin M. Arias. Two N-linked glycans are required to maintain the transport activity of the bile salt export pump (ABCB11) in MDCK II cells. *American Journal of Physiology. Gastrointestinal and Liver Physiology*, 292(3):G818–828, March 2007. (Cited on pages 49, 59 and 63.)

[158] Luis B Agellon and Enrique C Torchia. Intracellular transport of bile acids. *Biochimica et Biophysica Acta (BBA) - Molecular and Cell Biology of Lipids*, 1486(1):198–209, June 2000. (Cited on page 49.)

[159] A Stolz, H Takikawa, M Ookhtens, and and N. Kaplowitz. The Role of Cytoplasmic Proteins in Hepatic Bile Acid Transport. *Annual Review of Physiology*, 51(1):161–176, 1989. (Cited on page 49.)

[160] A. M. Van der Bliek, F. Baas, T. Ten Houte de Lange, P. M. Kooiman, T. Van der Velde-Koerts, and P. Borst. The human mdr3 gene encodes a novel P-glycoprotein homologue and gives rise to alternatively spliced mRNAs in liver. *The EMBO journal*, 6(11):3325–3331, November 1987. (Cited on page 49.)

[161] Gabriele Jedlitschky, Ulrich Hoffmann, and Heyo K. Kroemer. Structure and function of the MRP2 (ABCC2) protein and its role in drug disposition. *Expert Opinion on Drug Metabolism & Toxicology*, 2(3):351–366, June 2006. (Cited on page 49.)

[162] Jyh-Yeuan Lee, Lisa N. Kinch, Dominika M. Borek, Jin Wang, Junmei Wang, Ina L. Urbatsch, Xiao-Song Xie, Nikolai V. Grishin, Jonathan C. Cohen, Zbyszek Otwinowski, Helen H. Hobbs, and

Daniel M. Rosenbaum. Crystal structure of the human sterol transporter ABCG5/ABCG8. *Nature*, 533(7604):561–564, 2016. (Cited on page 49.)

[163] Wendy L. van der Woerd, Saskia W. C. van Mil, Janneke M. Stapelbroek, Leo W. J. Klomp, Stan F. J. van de Graaf, and Roderick H. J. Houwen. Familial cholestasis: progressive familial intrahepatic cholestasis, benign recurrent intrahepatic cholestasis and intrahepatic cholestasis of pregnancy. *Best Practice & Research. Clinical Gastroenterology*, 24(5):541–553, October 2010. (Cited on page 50.)

[164] Saskia W. C. van Mil, Wendy L. van der Woerd, Gerda van der Brugge, Ekkehard Sturm, Peter L. M. Jansen, Laura N. Bull, Inge E. T. van den Berg, Ruud Berger, Roderick H. J. Houwen, and Leo W. J. Klomp. Benign recurrent intrahepatic cholestasis type 2 is caused by mutations in ABCB11. *Gastroenterology*, 127(2):379–384, August 2004. (Cited on page 50.)

[165] Anshu Srivastava. Progressive familial intrahepatic cholestasis. *Journal of Clinical and Experimental Hepatology*, 4(1):25–36, March 2014. (Cited on page 50.)

[166] Ralf Kubitz, Carola Dröge, Jan Stindt, Katrin Weissenberger, and Dieter Häussinger. The bile salt export pump (BSEP) in health and disease. *Clinics and Research in Hepatology and Gastroenterology*, 36(6):536–553, December 2012. (Cited on page 51.)

[167] B. Stieger, K. Fattinger, J. Madon, G. A. Kullak-Ublick, and P. J. Meier. Drug- and estrogen-induced cholestasis through inhibition of the hepatocellular bile salt export pump (Bsep) of rat liver. *Gastroenterology*, 118(2):422–430, February 2000. (Cited on page 51.)

[168] K. Fattinger, C. Funk, M. Pantze, C. Weber, J. Reichen, B. Stieger, and P. J. Meier. The endothelin antagonist bosentan inhibits the canalicular bile salt export pump: a potential mechanism for hepatic adverse reactions. *Clinical Pharmacology and Therapeutics*, 69(4):223–231, April 2001. (Cited on page 51.)

[169] L. Huang, J. W. Smit, D. K. Meijer, and M. Vore. Mrp2 is essential for estradiol-17beta(beta-D-glucuronide)-induced cholestasis in rats. *Hepatology (Baltimore, Md.)*, 32(1):66–72, July 2000. (Cited on page 51.)

[170] Yvonne Meier, Tina Zodan, Carmen Lang, Roland Zimmermann, Gerd A. Kullak-Ublick, Peter J. Meier, Bruno Stieger, and Chris-

tiane Pauli-Magnus. Increased susceptibility for intrahepatic cholestasis of pregnancy and contraceptive-induced cholestasis in carriers of the 1331t>C polymorphism in the bile salt export pump. *World Journal of Gastroenterology*, 14(1):38–45, January 2008. (Cited on page 51.)

[171] José Ramón Lopéz-Blanco and Pablo Chacón. iMODFIT: efficient and robust flexible fitting based on vibrational analysis in internal coordinates. *Journal of Structural Biology*, 184(2):261–270, November 2013. (Cited on page 54.)

[172] Marcos Ariel Villarreal, Massimiliano Perduca, Hugo L. Monaco, and Guillermo G. Montich. Binding and interactions of L-BABP to lipid membranes studied by molecular dynamic simulations. *Biochimica Et Biophysica Acta*, 1778(6):1390–1397, June 2008. (Cited on page 65.)

[173] Jan Stindt, Philipp Ellinger, Katrin Weissenberger, Carola Dröge, Diran Herebian, Ertan Mayatepek, Bernhard Homey, Stephan Braun, Jan Schulte am Esch, Michael Horacek, Ali Canbay, Lutz Schmitt, Dieter Häussinger, and Ralf Kubitz. A novel mutation within a transmembrane helix of the bile salt export pump (BSEP, ABCB11) with delayed development of cirrhosis. *Liver International: Official Journal of the International Association for the Study of the Liver*, 33(10):1527–1535, November 2013. (Cited on page 69.)

[174] Ernesto Carafoli. Calcium-mediated cellular signals: a story of failures. *Trends in Biochemical Sciences*, 29(7):371–379, July 2004. (Cited on page 71.)

[175] Ernesto Carafoli. Calcium signaling: A tale for all seasons. *Proceedings of the National Academy of Sciences*, 99(3):1115–1122, February 2002. (Cited on page 72.)

[176] Michael J. Berridge, Martin D. Bootman, and H. Llewelyn Roderick. Calcium: Calcium signalling: dynamics, homeostasis and remodelling. *Nature Reviews Molecular Cell Biology*, 4(7):517–529, July 2003. (Cited on page 72.)

[177] Mordecai P. Blaustein and W. Jonathan Lederer. Sodium/Calcium Exchange: Its Physiological Implications. *Physiological Reviews*, 79(3):763–854, July 1999. (Cited on pages 72 and 81.)

[178] Kenneth D. Philipson and Debora A. Nicoll. Sodium-Calcium Exchange: A Molecular Perspective. *Annual Review of Physiology*, 62(1):111–133, 2000. (Cited on page 72.)

[179] Donald M. Bers. Cardiac excitation–contraction coupling, January 2002. (Cited on page 72.)

[180] L. Annunziato, G. Pignataro, and G. F. Di Renzo. Pharmacology of Brain Na+/Ca2+ Exchanger: From Molecular Biology to Therapeutic Perspectives. *Pharmacological Reviews*, 56(4):633–654, December 2004. (Cited on page 72.)

[181] Jonathan Lytton. Na+/Ca2+ exchangers: three mammalian gene families control Ca2+ transport. *Biochemical Journal*, 406(3):365–382, September 2007. (Cited on page 72.)

[182] Lynn M. Crespo, Christopher J. Grantham, and Mark B. Cannell. Kinetics, stoichiometry and role of the Na–Ca exchange mechanism in isolated cardiac myocytes. *Nature*, 345(6276):618–621, June 1990. (Cited on page 72.)

[183] Donald W. Hilgemann, Debora A. Nicoll, and Kenneth D. Philipson. Charge movement during Na+ translocation by native and cloned cardiac Na+/Ca2+ exchanger. *Nature*, 352(6337):715–718, August 1991. (Cited on page 72.)

[184] D. O. Levitsky, D. A. Nicoll, and K. D. Philipson. Identification of the high affinity Ca(2+)-binding domain of the cardiac Na(+)-Ca2+ exchanger. *The Journal of Biological Chemistry*, 269(36):22847–22852, September 1994. (Cited on page 72.)

[185] Mark Hilge, Jan Aelen, and Geerten W. Vuister. Ca2+ Regulation in the Na+/Ca2+ Exchanger Involves Two Markedly Different Ca2+ Sensors. *Molecular Cell*, 22(1):15–25, April 2006. (Cited on page 72.)

[186] Mark Hilge, Jan Aelen, Alice Foarce, Anastassis Perrakis, and Geerten W. Vuister. Ca2+ regulation in the Na+/Ca2+ exchanger features a dual electrostatic switch mechanism. *Proceedings of the National Academy of Sciences*, 106(34):14333–14338, August 2009. (Cited on page 72.)

[187] Donald W. Hilgemann and Rebecca Ball. Regulation of Cardiac Na+,Ca2+ Exchange and KATP Potassium Channels by PIP2. *Science*, 273(5277):956–959, August 1996. (Cited on page 72.)

[188] Urbanczyk Jason, Chernysh Olga, Condrescu Madalina, and Reeves John P. Sodium–calcium exchange does not require allosteric calcium activation at high cytosolic sodium concentrations. *The Journal of Physiology*, 575(3):693–705, September 2006. (Cited on page 72.)

[189] Xinjiang Cai and Jonathan Lytton. The Cation/Ca2+ Exchanger Superfamily: Phylogenetic Analysis and Structural Implications. *Molecular Biology and Evolution*, 21(9):1692–1703, September 2004. (Cited on page 72.)

[190] Debora A. Nicoll, Larry V. Hryshko, Satoshi Matsuoka, Joy S. Frank, and Kenneth D. Philipson. Mutation of Amino Acid Residues in the Putative Transmembrane Segments of the Cardiac Sarcolemmal Na+-Ca2+ Exchanger. *Journal of Biological Chemistry*, 271(23):13385–13391, June 1996. (Cited on pages 72 and 78.)

[191] Erich M. Schwarz and Seymour Benzer. Calx, a Na-Ca exchanger gene of Drosophila melanogaster. *Proceedings of the National Academy of Sciences*, 94(19):10249–10254, September 1997. (Cited on page 72.)

[192] Robert J. Winkfein, Robert T. Szerencsei, Tashi G. Kinjo, Kang, Marco Perizzolo, Lynn Eisner, and Paul P. M. Schnetkamp. Scanning Mutagenesis of the Alpha Repeats and of the Transmembrane Acidic Residues of the Human Retinal Cone Na/Ca-K Exchanger. *Biochemistry*, 42(2):543–552, January 2003. (Cited on pages 72 and 78.)

[193] Jun Liao, Hua Li, Weizhong Zeng, David B. Sauer, Ricardo Belmares, and Youxing Jiang. Structural Insight into the Ion-Exchange Mechanism of the Sodium/Calcium Exchanger. *Science*, 335(6069):686–690, February 2012. (Cited on pages 72, 74, 75, 78 and 83.)

[194] J. P. Reeves and J. L. Sutko. Competitive interactions of sodium and calcium with the sodium-calcium exchange system of cardiac sarcolemmal vesicles. *The Journal of Biological Chemistry*, 258(5):3178–3182, March 1983. (Cited on page 72.)

[195] Fabrizio Marinelli, Lior Almagor, Reuben Hiller, Moshe Giladi, Daniel Khananshvili, and José D. Faraldo-Gómez. Sodium recognition by the Na+/Ca2+ exchanger in the outward-facing conformation. *Proceedings of the National Academy of Sciences*, 111(50):E5354–E5362, December 2014. (Cited on page 72.)

[196] Andrew B. Waight, Bjørn Panyella Pedersen, Avner Schlessinger, Massimiliano Bonomi, Bryant H. Chau, Zygy Roe-Zurz, Aaron J. Risenmay, Andrej Sali, and Robert M. Stroud. Structural basis for alternating access of a eukaryotic calcium/proton exchanger. *Nature*, 499(7456):107–110, July 2013. (Cited on pages 72 and 75.)

[197] Tomohiro Nishizawa, Satomi Kita, Andrés D. Maturana, Noritaka Furuya, Kunio Hirata, Go Kasuya, Satoshi Ogasawara, Naoshi Dohmae, Takahiro Iwamoto, Ryuichiro Ishitani, and Osamu Nureki. Structural Basis for the Counter-Transport Mechanism of a H+/Ca2+ Exchanger. *Science*, 341(6142):168–172, July 2013. (Cited on pages 72 and 75.)

[198] Mousheng Wu, Shuilong Tong, Sandro Waltersperger, Kay Diederichs, Meitian Wang, and Lei Zheng. Crystal structure of Ca2+/H+ antiporter protein YfkE reveals the mechanisms of Ca2+ efflux and its pH regulation. *Proceedings of the National Academy of Sciences*, 110(28):11367–11372, July 2013. (Cited on page 72.)

[199] Simon Newstead, Hyun Kim, Gunnar von Heijne, So Iwata, and David Drew. High-throughput fluorescent-based optimization of eukaryotic membrane protein overexpression and purification in Saccharomyces cerevisiae. *Proceedings of the National Academy of Sciences*, 104(35):13936–13941, August 2007. (Cited on pages 73 and 82.)

[200] David Sehnal, Radka Svobodová Vařeková, Karel Berka, Lukáš Pravda, Veronika Navrátilová, Pavel Banáš, Crina-Maria Ionescu, Michal Otyepka, and Jaroslav Koča. MOLE 2.0: advanced approach for analysis of biomacromolecular channels. *Journal of Cheminformatics*, 5:39, August 2013. (Cited on pages 76 and 77.)

[201] Peter Dimroth. Na+-coupled alternative to H+-coupled primary transport systems in bacteria. *BioEssays*, 13(9):463–468, September 1991. (Cited on page 79.)

[202] M. Egger and E. Niggli. Regulatory Function of Na-Ca Exchange in the Heart: Milestones and Outlook. *Journal of Membrane Biology*, 168(2):107–130, March 1999. (Cited on page 81.)

[203] Toshimitsu Kawate and Eric Gouaux. Fluorescence-Detection Size-Exclusion Chromatography for Precrystallization Screening of Integral Membrane Proteins. *Structure*, 14(4):673–681, April 2006. (Cited on page 82.)

[204] W. Kabsch. XDS. *Acta Crystallographica Section D: Biological Crystallography*, 66(2):125–132, February 2010. (Cited on page 83.)

[205] P. R. Evans. An introduction to data reduction: space-group determination, scaling and intensity statistics. *Acta Crystallographica Section D: Biological Crystallography*, 67(4):282–292, April 2011. (Cited on page 83.)

[206] M. D. Winn, C. C. Ballard, K. D. Cowtan, E. J. Dodson, P. Emsley, P. R. Evans, R. M. Keegan, E. B. Krissinel, A. G. W. Leslie, A. McCoy, S. J. McNicholas, G. N. Murshudov, N. S. Pannu, E. A. Potterton, H. R. Powell, R. J. Read, A. Vagin, and K. S. Wilson. Overview of the CCP4 suite and current developments. *Acta Crystallographica Section D: Biological Crystallography*, 67(4):235–242, April 2011. (Cited on page 83.)

[207] Michael Strong, Michael R. Sawaya, Shuishu Wang, Martin Phillips, Duilio Cascio, and David Eisenberg. Toward the structural genomics of complexes: Crystal structure of a PE/PPE protein complex from Mycobacterium tuberculosis. *Proceedings of the National Academy of Sciences*, 103(21):8060–8065, May 2006. (Cited on page 83.)

[208] Airlie J. McCoy, Ralf W. Grosse-Kunstleve, Paul D. Adams, Martyn D. Winn, Laurent C. Storoni, and Randy J. Read. Phaser crystallographic software. *Journal of Applied Crystallography*, 40(Pt 4):658–674, August 2007. (Cited on page 83.)

[209] Frank DiMaio, Thomas C. Terwilliger, Randy J. Read, Alexander Wlodawer, Gustav Oberdorfer, Ulrike Wagner, Eugene Valkov, Assaf Alon, Deborah Fass, Herbert L. Axelrod, Debanu Das, Sergey M. Vorobiev, Hideo Iwai, P. Raj Pokkuluri, and David Baker. Increasing the Radius of Convergence of Molecular Replacement by Density and Energy Guided Protein Structure Optimization. *Nature*, 473(7348):540–543, May 2011. (Cited on page 84.)

[210] E. Blanc, P. Roversi, C. Vonrhein, C. Flensburg, S. M. Lea, and G. Bricogne. Refinement of severely incomplete structures with maximum likelihood in BUSTER–TNT. *Acta Crystallographica Section D: Biological Crystallography*, 60(12):2210–2221, December 2004. (Cited on page 84.)

[211] Eric R. Geertsma, N. A. B. Nik Mahmood, Gea K. Schuurman-Wolters, and Bert Poolman. Membrane reconstitution of ABC transporters and assays of translocator function. *Nature Protocols*, 3(2):256–266, February 2008. (Cited on page 84.)

[212] Dirk Jan Slotboom, Ria H. Duurkens, Kees Olieman, and Guus B. Erkens. Static light scattering to characterize membrane proteins in detergent solution. *Methods*, 46(2):73–82, October 2008. (Cited on page 85.)